

Dynamic Aeroelastic Performance Optimization of Adaptive
Aerospace Structures Employing Structural Geometric
Nonlinearities

by

William P. Parsons

BEng in Mechanical Engineering

A thesis submitted to the Faculty of Graduate and Postdoctoral Affairs in
partial fulfillment of the requirements for the degree of

Master of Applied Science

in

Aerospace Engineering

Carleton University

Ottawa, Ontario

© 2021, William P. Parsons

Abstract

This thesis proposes a framework for the design optimization of geometric nonlinearities developed by active elements embedded in truss-like aerospace structures for the purpose of attenuating their dynamic aeroelastic response under turbulent aerodynamic gust conditions. Dynamic aeroelastic responses are analyzed considering random Power Spectral Density (PSD) and Tuned Discrete Gust (TDG) excitation profiles. MSC NASTRAN® is employed for the development of the dynamic aeroelastic models where the random PSD with a continuous Davenport spectrum (DS) and the TDG with a One-minus cosine (OMC) wind gust excitation profiles are developed. This work presents a multi-objective genetic optimization algorithm (MOGA) utilized to determine optimal prestress values through active element actuations for the purpose of tuning the geometric stiffness and therefore modal response of the structure when exposed to gust excitations. Additionally, this work contributes a new simplified control metric for comparing active member locations. Two case studies are presented to minimize the pointing error of both a simplified and high-fidelity (HF) Earth-based very-long baseline interferometry (VLBI) antenna structure. The pointing error is calculated as the spatial displacement of the secondary reflector using time-consistent displacements (TCD) imparted by time consistent loads (TCL).

To increase the computational efficiency of the design optimization process of the HF model, model order reduction is conducted using the Craig-Bampton method which resulted in the computation time decreasing from 39.21 minutes to only 50 seconds while maintaining a 99.9% Modal Assurance Criterion (MAC) correlation in the first 20 mode shapes of interest of the structure. With the reduced model, the framework used multi-objective genetic optimization with

the dual objectives of decreasing total pointing error while minimizing the total strain energy in the system as a result of both the applied aerodynamic and inertia loads as well as the applied actuations. The yield strength of the elements and their maximum displacements were used as design constraints to ensure integrity of the structure. Pareto fronts are presented containing optimal responses for 16, 32, and 44 active members of the structure. The utopian point method was employed to calculate the best configuration of active members to be considered. A reduction of 82.6% with a total strain energy increase of 292.5% was obtained for the primary operating case under PSD gust excitation. On the other hand, at the increased mean wind speeds of the secondary operating case, the developed design algorithm was able to reduce the total pointing error by 80.9% but with a total strain energy increase of 825.3%. Similarly, for TDG analysis with the OMC excitation profile the optimization algorithm reduced the total pointing error by 51.6% with a TSE increase of 2098.1% and 80.5% with a TSE increase of 48.7% for the primary and secondary operating conditions, respectively, when compared to the uncontrolled response. The adaptive nature of the presented methodology allows a single actuator layout to mitigate structural response for a variety of load cases, which is a large benefit over many traditionally passive techniques. This thesis expands the existing usage of geometric nonlinearities to determine optimal active element location and actuations for given optimization objectives under realistic environmental loading conditions.

Keywords: geometric stiffness, geometric nonlinearities, prestress, states of self-stress, dynamic aeroelastic response analysis, time consistent displacements, time consistent loads, multi-objective genetic algorithm

PREFACE

This research project is an original work developed by William Parsons, under the supervision of Professor Mostafa El Sayed, conforming to all mandatory requirements as stated by Carleton University.

The project is part of the InterTronic Solutions and NASA initiative to develop high-fidelity VLBI ground stations. In close collaboration, InterTronic Solutions provided data relevant to the aeroelastic numerical model, which is used as part of the case study in chapter 8.

One conference paper: Parsons, W.P., ElSayed, M.S.A., Saad, M., Shield, S. (2021), “Geometric Nonlinearities for Tuning and Control of the Dynamic Response of Flexible Structures” presented during the AIAA 2021 online conference and two journal papers: Parsons, W.P., Gasparetto, V.E.L., ElSayed, M.S.A. (2021), “Optimization of Geometric Nonlinearities using a Genetic Algorithm for Attenuation of Dynamic Aeroelastic Response in Adaptive Aerospace Structures” and Parsons, W.P., Gasparetto, V.E.L., ElSayed, M.S.A. (2021), “Multi-Objective Design Optimization of Structural Geometric Nonlinearities within VLBI Antennae for High-fidelity Performance” were partially reproduced here under Chapter 6.3, Chapter 7, and Chapter 8, respectively.

Acknowledgements

As I write this, I am just beginning to construct this thesis that defines the past two years of my life. Two years filled with personal struggles and victories, and endless uncertainty in the face of a global pandemic. I have learned so much both theoretically from this degree as well as internally and I would like to thank the people who made that possible. Firstly, I would like to thank my supervisor Mostafa El Sayed who always brought not only the technical expertise to our conversations but also the perfect amount of pressure paired with constant compassion and belief in me to march on. Next, I would like to thank my colleague and friend Victor Gasparetto for helping to breathe life into a project that at times felt very lonely and overwhelming. Finally, I would like to thank my friends and family for their unconditional support and kindness through these difficult times for which without I would not have succeeded. A special thanks to my fiancée Carley for going on this adventure with me and continuing to support both our dreams. One of my favorite sayings has always been the Latin phrase *Per Aspera Ad Astra* which translates to “through hardships to the stars”, which I believe perfectly summarizes this experience.

Table of Contents

Abstract.....	ii
Acknowledgements	v
Table of Contents	vi
List of Tables	ix
List of Figures.....	x
List of Appendices.....	xiv
Nomenclature	xv
Acronyms	xviii
Chapter 1: Introduction	1
1.1 Background and Motivation	1
1.2 Thesis Overview	5
Chapter 2: Literature Review.....	7
2.1 Definition and Classification of Tensegrity Structures	7
2.2 Analysis of Tensegrity Structures.....	9
2.2.1 Static Response Applications.....	10
2.2.2 Dynamic Response Applications	11
Chapter 3: Theoretical Framework Part I: Stiffening Effects of Geometric Nonlinearities	16

3.1	Determinacy Analysis and Geometric Stiffness Finite Element Formulation.....	16
3.2	Optimal Location of Active Members.....	22
Chapter 4: Theoretical Framework Part II: Dynamic Aeroelastic Response Analysis of Complex Structures		26
4.1	Reduced Order Models.....	26
4.2	Aerodynamic Disturbance Models	29
4.3	Dynamic Aeroelastic Equations of Motion with Geometric Nonlinearities.....	31
4.4	Time Consistent Outputs	35
Chapter 5: Theoretical Framework Part III: Genetic Algorithm Optimization		39
5.1	Genetic Algorithm Parameters	40
5.2	Multi-Objective Genetic Algorithms.....	43
Chapter 6: Software Implementation of Proposed Framework.....		45
6.1	Implementation in MATLAB and NASTRAN	45
6.2	Overall Design Procedure for the Optimization of Geometric Nonlinearities	46
6.3	Framework Validation.....	51
Chapter 7: Case Study I: Attenuation of the dynamic aeroelastic response of a Simplified VLBI antenna model using a single-objective genetic optimization algorithm		54
7.1	Simplified Antenna Model and Optimization Parameters.....	57
7.2	Results for Simplified Antenna Model.....	62

Chapter 8: Case Study II: Attenuation of the dynamic aeroelastic response of a 12-m VLBI antenna model using a multi-objective genetic optimization algorithm	70
8.1 VLBI Antenna Model.....	71
8.2 Parameters for Analysis of VLBI Antenna Model	76
8.3 Results for VLBI Antenna Model	82
Chapter 9: Conclusion and Further Work.....	96
9.1 Recommendations for Future Work	98
Appendices.....	99
Appendix A	99
References	103

List of Tables

Table 7.1 - Primary and Secondary Operating Cases	56
Table 7.2 - Active Element Locations	62
Table 7.3 - Summary of Attenuation	69
Table 8.1 - Objective function values for the best individuals within each subcase of the DS frequency response analysis.....	88
Table 8.2 – Objective function values for the best individuals within each subcase of the OMC time response analysis.....	94

List of Figures

Figure 1.1 – Class-1 T3 Prism Tensegrity Structure.....	2
Figure 1.2 - Determinacy states of structures a) with one IMM and no SSS b) with no IMM or SSS c) with no IMM and one SSS.....	3
Figure 1.3 - Simple process diagram for the framework of optimizing geometric nonlinearities using a genetic algorithm for attenuation of the dynamic aeroelastic responses in adaptive aerospace structures	5
Figure 2.1 – Classification of tensegrity structures [27].....	8
Figure 2.2 – Relationship between the static and dynamic analysis of tensegrities [55].....	12
Figure 2.3 – Effect of actuation on prestressable structures under loading [63]	14
Figure 4.1 – Example DLM panel for a cantilever beam wing	32
Figure 4.2 – Map of models used in dynamic aeroelastic analysis [90].....	38
Figure 5.1 – Flowchart process of a general genetic algorithm	40
Figure 5.2 - k-point crossover visualization of parent and offspring chromosomes [92].....	42
Figure 5.3 - Pareto front and Utopian point method for maximum and minimizations of MOGA	44
Figure 6.1 – Detailed process diagram for the framework of optimizing geometric nonlinearities using a genetic algorithm for attenuation of the dynamic aeroelastic responses of structures	47

Figure 6.2 - Global state of self-stress for simple triplex tensegrity.....	51
Figure 6.3 - Internal mechanism mode for simple triplex tensegrity.....	52
Figure 6.4 - Effect of prestress on the first six natural frequencies of a simple triplex tensegrity	53
Figure 7.1 - Operating case excitation profiles for a) DS and b) OMC gust models.....	56
Figure 7.2 – Simplified VLBI antenna geometry with boundary conditions and important nodes	57
Figure 7.3 – a) InterTronic Solutions 12 m VLBI antenna [102] and b) Added diagonals required for geometric stiffness tuning	58
Figure 7.4 - Initial Response to DS Primary operating case.....	59
Figure 7.5 – Initial Response to DS Secondary operating case	59
Figure 7.6 - Initial Response to OMC Primary operating case.....	60
Figure 7.7 - Initial Response to OMC Secondary operating case.....	60
Figure 7.8 - Active element configurations for each analysis subcase	62
Figure 7.9 - Example of convergence of design vector through generations	63
Figure 7.10 - Frequency response functions for the target node per DOF (Primary Case)	64
Figure 7.11 - Frequency response functions for the target node per DOF (Secondary Case)	65

Figure 7.12 - Optimal element actuations for each actuator configuration when exposed to the secondary operating condition of the Davenport spectrum	67
Figure 7.13 – a) Total and b) per DOF response for each subcase (OMC - Primary Case)	68
Figure 7.14 – a) Total and b) per DOF response for each subcase (OMC - Secondary Case)	68
Figure 8.1 – MAC a) DFEM vs Nieto-ROM [90] b) GP-ROM vs Nieto-ROM	73
Figure 8.2 – a) DFEM b) Nieto-ROM [90] c) GP-ROM.....	74
Figure 8.3 – VLBI Antenna boom arm subsystem vs remaining structure	75
Figure 8.4 – Boom arm subsystem of GP-ROM for VLBI antenna	76
Figure 8.5 – Target and reference node definitions for VLBI antenna.....	77
Figure 8.6 – Location of best active elements and remaining element IDs in the boom arm subsystem.....	79
Figure 8.7 – Uncontrolled response to DS a) Primary operating case and b) Secondary operating case.....	81
Figure 8.8 - Uncontrolled response to OMC a) Primary operating case and b) Secondary operating case.....	81
Figure 8.9 - Pointing path deviation angle frequency response of the target node in the Θ , Φ , and Ψ directions for the Davenport spectrum primary operating case with 16 active elements	83

Figure 8.10 – Utopian point plot and determination of best individual for the Davenport spectrum primary operating case with 16 active elements	85
Figure 8.11 – Uncontrolled vs. best individual response for the Davenport spectrum primary operating case with 16 active elements.....	86
Figure 8.12 – Pointing path deviation angle frequency response of the target node in the Θ , Φ , and Ψ directions for the Davenport spectrum secondary operating case with 16 active elements.....	87
Figure 8.13 – Pointing path deviation angle frequency response of the target node in the Θ , Φ , and Ψ directions for the OMC primary operating case with 44 active elements.....	90
Figure 8.14 – Total pointing path deviation angle frequency response of the target node for the OMC primary operating case with 44 active elements.....	90
Figure 8.15 – Utopian point plot and determination of best individual for the OMC primary operating case with 44 active elements.....	91
Figure 8.16 – Uncontrolled vs. best individual response for the Davenport spectrum primary operating case with 44 active elements.....	92
Figure 8.17 - Pointing path deviation angle frequency response of the target node in the Θ , Φ , and Ψ directions for the OMC secondary operating case with 44 active elements	93
Figure 8.18 - Total pointing path deviation angle frequency response of the target node for the OMC secondary operating case with 44 active elements	93

List of Appendices

Appendix A.....	99
-----------------	----

Nomenclature

Latin Characters

Symbol	Definition
$\bar{\mathbf{M}}$	Mass matrix
$\bar{\mathbf{K}}_{\text{TOT}}$	Total stiffness matrix
$\mathbf{K}_{\mathbf{M}}$	Material stiffness matrix
$\mathbf{K}_{\mathbf{G}}$	Geometric stiffness matrix
\mathbf{C}	Element connectivity matrix
$\bar{\mathbf{C}}$	Damping matrix
\mathbf{u}_k	Aerodynamic displacements
\mathbf{w}_j	Downwash vector
f_j	Normalized lifting pressure at the j -th point
\mathbf{D}_{jk}^1	Substantial differentiation matrix 1
\mathbf{D}_{jk}^2	Substantial differentiation matrix 2
\mathbf{S}_{kj}	Integration matrix
c_{ref}	Reference airfoil chord length
V_{∞}	Free stream velocity
\mathbf{Q}_{kk}	Force Aerodynamic Influence Coefficients matrix
\mathbf{G}_{kd}	Structural splining matrix
\mathbf{Q}_{dd}	Matrix of Force Aerodynamic Influence coefficients
\mathbf{Q}_{hh}	Modal Matrix of Force Aerodynamic Influence coefficients
$\mathbf{q}(\omega)$	Harmonic modal response in the frequency domain
$\mathbf{P}(\omega)$	Modal forces vector in the frequency domain

$\mathbf{F}(t)$	Column vector of non-aerodynamic forces
Δv	Wind gust velocity
v_{g0}	Peak gust disturbance or design gust velocity
L_g	Gust length
$S_D(\omega)$	Davenport Spectrum PSD function
z	Mean height of structure
z_0	Height of the surface roughness
t	Time
t_{crit}	Time at critical frequency
N	Number of active elements
ΔL	Length change in active elements
S_F	Force influence matrix
S_d	Displacement influence matrix
$P_{k_{eff}}$	Effective prestress in element k
$P_{k_{MAX}}$	Max allowable prestress in element k
A_{cs}	Cross-sectional area
l_k	Length of element k
Δd	Nodal displacements vector
Δp	Applied force change in element
G	Flexibility matrix
W_s	Self-stress modes matrix
A	Equilibrium matrix
C	Connectivity matrix
Q	Force density matrix

Greek Characters

Symbol	Definition
φ_i	i -th mode shape
ω	Circular frequency
ω_{crit}	Critical circular frequency
ρ	Density
φ_{crit}	Critical phase angle
σ_{MAX}	Tensile yield strength
α	Linear combination vector of states of self-stress
Ω_{crit}	Critical excitation frequency in degrees
Γ	Hierarchy metric vector
ε_0	Initial strain vector
θ	Deviation angle associated with the x -direction
Φ	Deviation angle associated with the y -direction
Ψ	Deviation angle associated with the z -direction

Acronyms

Acronym	Definition
AIC	Aerodynamic Influence Coefficients
CBMOR	Craig-Bampton Model Order Reduction
DFEM	Detailed Finite Element Model
DLM	Doublet-Lattice Method
DMIG	Direct Matrix Input Grid
DOF	Degree of Freedom
DS	Davenport Spectrum
EOM	Equation of Motion
FRF	Frequency Response Function
GA	Genetic Algorithm
HF	High-Fidelity
ID	Identification
IMM	Internal Mechanism Modes
MAC	Modal Assurance Criteria
MOGA	Multi-objective Genetic Algorithm
NASA	National Aeronautics and Space Administration
OMC	One-Minus Cosine
PCH	Punch file
PSD	Power Spectrum Density
ROM	Reduced Order Model
RSSQ	Root Sum of Squares
SF	Safety Factor

SOL	Solution
SSS	States of Self-Stress
SVD	Singular Value Decomposition
TCX	Time Consistent Outputs
TDG	Tuned Discrete Gust
TRF	Time Response Function
TSE	Total Strain Energy
VLBI	Very Long Baseline Interferometry

Chapter 1: Introduction

In the case of aerospace structures, the performance, weight, service life expectancy, and maintenance cost are key factors that drive design. Optimizing these parameters during design is of utmost importance to the success of the implementation of the structure. To achieve proper safety metrics, these structures are often designed to handle worst-case dynamic loading scenarios and are thus over-designed for more common load cases. The dynamic response is directly correlated to the dynamic loading experienced by the structure where excitation frequencies near resonance can compromise the structural integrity and performance [1,2], thus, it is beneficial to tune the structure based on expected excitation frequencies to avoid such resonances.

The following sections present the relevant background information and motivation for this thesis. As well, an overview of the thesis is given to introduce the reader to the structure of the document and assist in understanding the presented work.

1.1 Background and Motivation

Reducing the dynamic response of a structure can lead to improved performance, reduced maintenance cost, and increased service life [3–7]. Aerospace structures achieve this through various methods of either passive [8–11] or active/adaptive control [12–17]. Adaptive structures offer the added benefit of actively shifting their properties to handle different operating conditions, thus reducing the need for overdesign as previously mentioned. One method of implementing active control is through the integration of actively-prestressable members to increase the stiffness of the structure in response to expected loading.

Tensegrity structures, derived from the words tension and integrity, are defined as prestressable structures comprised of cables and struts which carry solely axial loads, tension for cables or compression for struts [18]. Because each member is strictly axial load carrying the lack of bending moments results in high rigidity structures and allows simple joints to be used [19]. For aerospace structures with lattice or truss-like geometries the resonance peaks can be tuned by leveraging tensegrity structuring techniques. Tensegrity analysis such as form-finding, force-finding, and spectral analysis can be done on pin or ball-jointed truss-structures idealized as tensegrities, while not having all tensegrity features [20–22]. A visual example of the simplest tensegrity structure, denoted a Class-1 T3-prism, is given below in Figure 1.1 where the thicker bars are struts, and the remaining cables provide structural integrity.

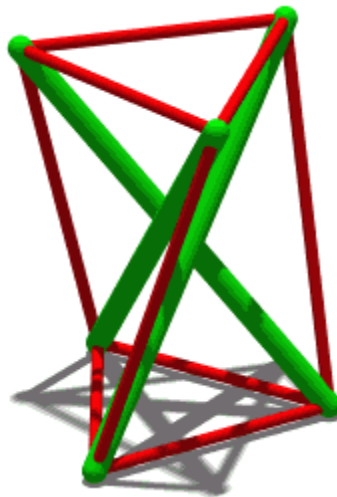


Figure 1.1 – Class-1 T3 Prism Tensegrity Structure

According to Pellegrino and Calladine [23,24], structures can be classified based on their kinematic and static determinacy. Statically determinate structures are stable structures with all unknown reactive forces solvable from the equilibrium equations while statically indeterminate structures are stable yet contain more unknowns than available equilibrium equations. Analyzing

the equilibrium, and by duality, kinematic matrices of a structure finds that a statically indeterminate structure contains states of self-stress (SSS), defined as sets of elemental stresses in static equilibrium with zero applied load while a kinematically indeterminate structure has degrees of freedom allowing the members to move without elemental length changes, deemed inextensional mechanism modes (IMM). The states of self-stress are intrinsic properties of the structures geometry and are only changed with a change in geometry, thus, the actual experienced stress state of the entire structure can be tuned by introducing geometric nonlinearities through active element length changes, regardless of the existence of IMM's.

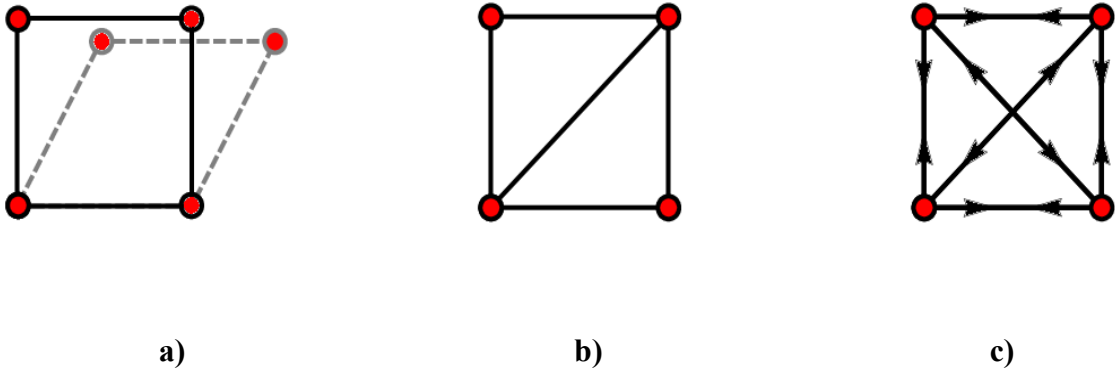


Figure 1.2 - Determinacy states of structures a) with one IMM and no SSS b) with no IMM or SSS c) with no IMM and one SSS

As shown in Figure 1.2a, this simple structure contains an internal mechanism mode as it can move without the need for element length changes. From Figure 1.2b the structure cannot move without length changes, however, with one element changing length the others would simply move to accommodate the change. In contrast, from Figure 1.2c it is evident that making any member active and extending its length would induce stresses in the other members, termed prestress, the magnitude of which can be determined by the state of self-stress modes. The collection of these prestresses defines what is known as the structure's geometric stiffness, an additional stiffness to

the material stiffness matrix on a per element basis. While this method of structural tuning has many potential applications, currently no framework exists for geometric stiffness optimization to tailor the dynamic aeroelastic response of structures, which will be the focus of this thesis. The states of self-stress will be analyzed for their tuning capabilities and optimal actuator locations and corresponding prestress levels will be calculated accordingly. This will be done considering the effects of environmental gust disturbances on the dynamic aeroelastic response and element internal loads.

Dynamic aeroelastic response analysis considers elastic and inertial forces of the structure as well as the effect on the structure from external aerodynamic forces. These aerodynamic forces must be transferred from the load excitation profile to the structure and will be done using the doublet-lattice method (DLM) in this thesis. Two different excitation profiles will be used in this work, namely the random Power Spectral Density with Davenport spectrum for frequency domain analysis and Tuned Discrete Gust for time domain analysis. The dynamic response of the structure to these excitation profiles hinders on the aerodynamic equations of motion which are altered, and therefore can be tuned, by the geometric stiffness as mentioned above.

Finally, to achieve the optimal tuning of the dynamic response using geometric stiffness as the design input, an optimization algorithm is required to determine the optimal design values within the specified constraints. This thesis leverages both single and multi-objective genetic optimization algorithms to tune the dynamic response for various objectives. Figure 1.3 depicts a simplified process diagram of the proposed framework to give initial context to the reader for the following chapters.

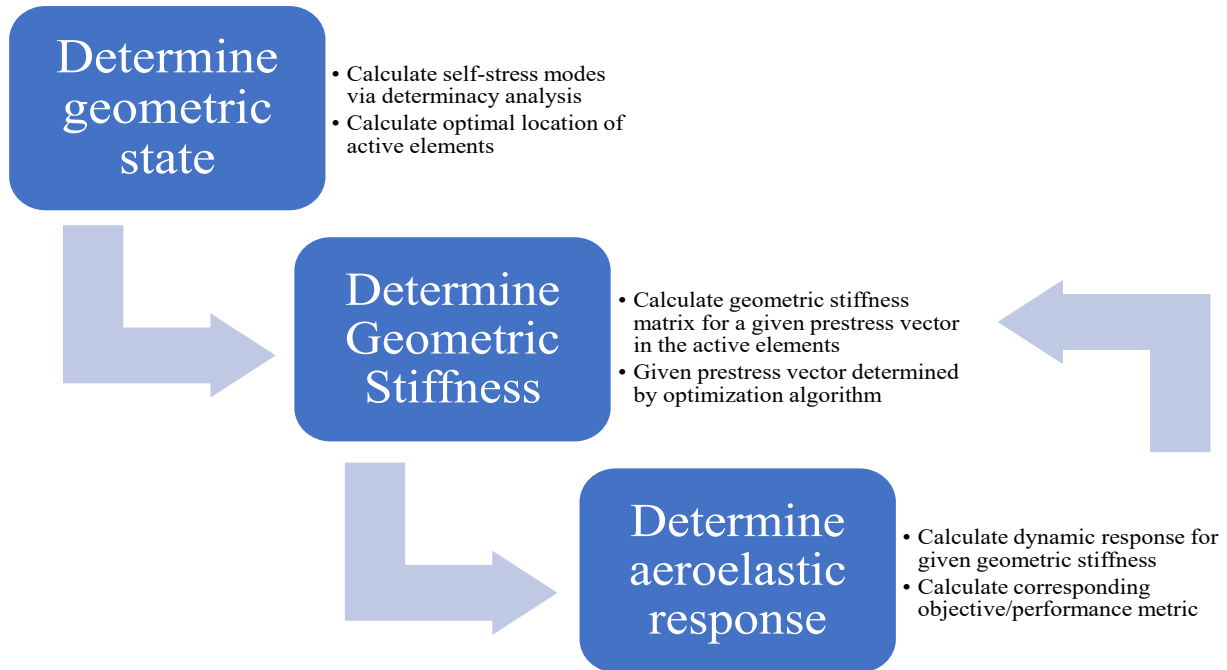


Figure 1.3 - Simple process diagram for the framework of optimizing geometric nonlinearities using a genetic algorithm for attenuation of the dynamic aeroelastic responses in adaptive aerospace structures

The second and third steps are completed within the design space of a single or multi-objective genetic algorithm to find the optimal design vector to minimize or maximize the objective/performance metrics.

1.2 Thesis Overview

This thesis is structured as follows: First, a literature review is presented to outline the existing work in utilizing geometric nonlinearities, establishing a basis of current research and highlighting the need for this thesis' contribution to the area. Next, the relevant theory of geometric nonlinearities is discussed including determinacy analysis, geometric stiffness formulation, force and shape influence matrices, as well as the newly proposed optimal location metric. Following

afterwards, the theory of reducing a high-fidelity model for performing dynamic aeroelastic analysis and the excitation models needed to do so is given. As well, the expected outputs and post-processing of such analysis will be discussed. Next, single and multi-objective genetic algorithm optimization is discussed in the context of geometric stiffness tuning and the implementation of all relevant theory in software will conclude the definition of the proposed framework. Finally, two applications of the framework are presented. The first of which is a simplified VLBI antenna with the singular objective of minimizing pointing error. Second, a full high-fidelity VLBI antenna model from InterTronic Solutions is analyzed with the dual objectives of minimizing pointing error and total strain energy in the system under both continuous and discrete gust disturbances in the frequency and time domains, respectively. The Craig-Bampton model order reduction technique is also discussed which is used to increase the computational efficiency of the VLBI antenna model. The relevant results are discussed and future considerations are offered.

Chapter 2: Literature Review

In this section, past and present research done in the areas of prestressable structures will be defined to illustrate the need for this work. While the intended application of this work is not specifically on tensegrity structures, they form the basis of the simplest type of prestressable structures for which the important principles of form-finding, force-finding, spectral analysis, and optimization/control all apply.

2.1 Definition and Classification of Tensegrity Structures

Although the original inventor of the tensegrity structure is still up to much debate, the general aspects that define them are universally accepted. In one of the most influential books in the field, Fuller gives the following definition: “Tensegrity describes a structural relationship principle in which structural shape is guaranteed by the finitely closed, comprehensively continuous, tensional behaviors of the system and not by the discontinuous and exclusively local compressional behaviors” [25]. This was then updated shortly after by Pugh in 1976, “A Tensegrity system is established when a set of discontinuous compressive components interacts with a set of continuous tensile components to define a stable volume in space” [26]. Since then, important additional aspects such as “self-supporting” and “self-equilibrated” as well as a class system have been added to the definition of a tensegrity. The class designation is based on the maximum number of struts that connect together at a node, where a pure classical tensegrity consisting of only struts connected to cables would be Class-1. This classification is a clear way of understanding the transition from a pure classical tensegrity with only struts and cables (Class-1) to a prestressable truss structure (Class-n).

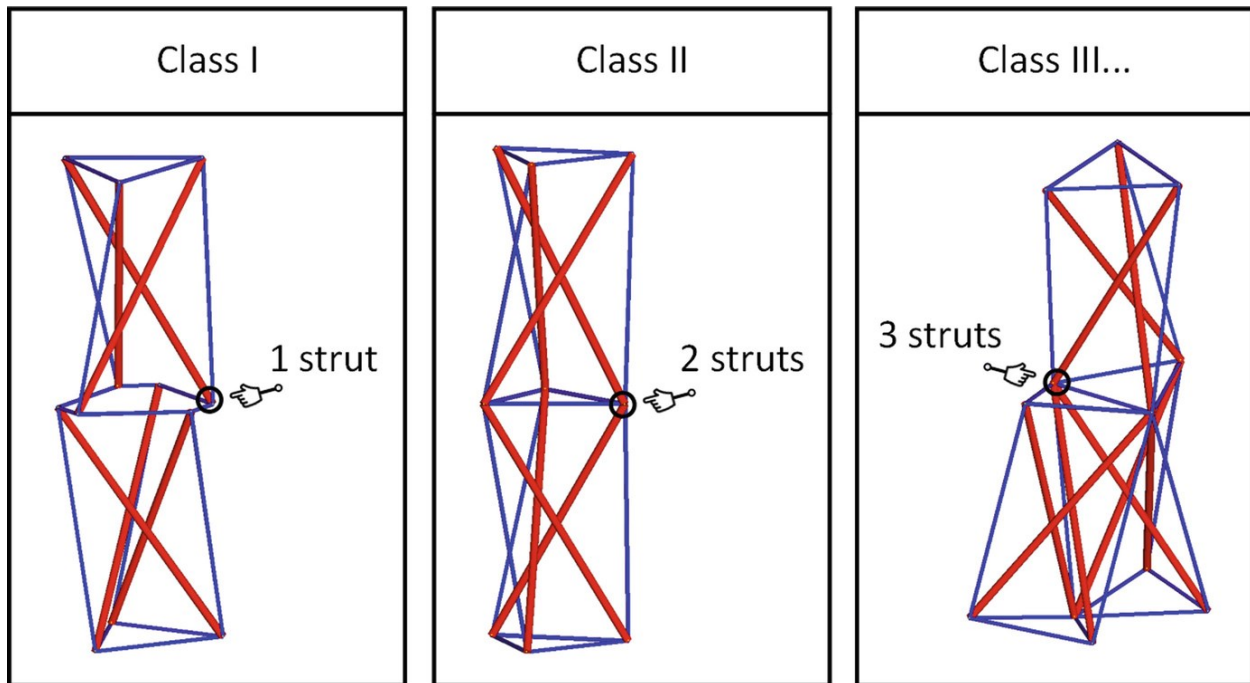


Figure 2.1 – Classification of tensegrity structures [27]

The class of the tensegrity greatly influences the stiffness of the structure and will determine the applications for which it is used. Due to the wide variety of tensegrity classes from 1 to n an equivalent wide range of application is possible. Lower class tensegrities were originally used in architecture for their aesthetics and illusion of floating from their self-supporting nature. They are also easily deployable to create larger structures from simple cables and struts. This becomes very useful in space applications for deployable solar arrays, space antennas, and masts as they can be compactly and lightly brought to space on a launch vehicle before deploying to their intended application [28,29]. This is similar to the process of a camping tent where the cables and poles are easily compacted in a carrying bag before deploying into a large, high-stiffness (relative to mass) structure. More advantages of tensegrity structures are given by Skelton [30] and Juan [31] and are summarized as follows:

- **Efficient:** Tensegrities can exhibit large stiffness to mass ratios, only needing material in the load paths. They also store energy in the form of compression and tension so actuation energy is partially stored in the structure itself, leading to high energy efficiency [32].
- **Scalability:** The tensegrity structure analysis principles are based solely on the geometry and can therefore be scaled to their intended application. One extreme of this is in nanostructures where wireframe and tensegrity DNA are leveraged [33].
- **Redundancy and Tunability:** Elements within a tensegrity structure can be replaced with smart elements such as sensors, linear actuators, and other load carrying elements. Additionally, due to the prestressed nature of tensegrities the stiffness properties of the structure can be tuned to the intended application and when paired with sensors can respond to external excitations. These two principles will serve as the basis for this research.

Now that the basic definition and classification of tensegrities has been given, the existing research done in the field of static analysis, dynamic analysis, and optimization of tensegrities will be reviewed while further discussing potential applications.

2.2 Analysis of Tensegrity Structures

All initial research in the field of tensegrities was done as static analysis. This is because the static analysis of the structure determines its self-equilibration state(s) thus providing stability and ultimately allowing its existence. Although Fuller [25], Emmerich [34], and Pugh [26] were the first few to implement tensegrity techniques into their work they mostly relied on intuitive methods without mathematical criteria. Also, the first tensegrity applications were in architecture simply for their aesthetics or for creating cable-strut domes, it was not until much later that tensegrity properties were utilized in civil or aerospace applications. The first mathematical static analysis

was not performed on tensegrity structures until 1981 by Roth and Whiteley [35] where they applied concepts used on bar frameworks and extended them to the theories of tensegrities. The next important breakthrough in the area was Calladine and Pellegrino as previously mentioned in Chapter 1.1. Calladine proved the concepts of self-stress and how they can stiffen internal mechanisms [36]. Pellegrino and Calladine then developed a framework to determine the number of states of self-stress, internal mechanisms, and equilibrium configurations [37–40]. Important to this work, Pellegrino also defined the effect of external loads on a static tensegrity that is kinematically indeterminate [38]. Their work on extending Maxwell's rule still serves as the basis for determinacy analysis of kinematically and statically indeterminate structures although many new ways have been developed in computing such an analysis. It was not until 1998 with Wang [41] defining the relationship between the prestress distribution and the stiffness of a structure that the field of adaptive prestressable structures really took off and the possible applications expanded greatly. Adaptive prestressable structures have the ability to change their shape by using active members such as actuators controlled by a control system [42]. The following section will review the research done in the field of adaptive prestressable structures.

2.2.1 Static Response Applications

Most of the early static response applications were simple form-finding and force-finding of tensegrities where analysis was done to determine the required configuration of struts and cables to achieve an optimal shape. A lot of research was done into different methods for this analysis, including non-linear programming techniques, the introduction of the singular-value decomposition method, dynamic relaxation method, and most recently the integrated force density method (which will be the technique of choice for this paper due to its simplicity and direct relationship to active member length changes) [24,43,44]. Recently, with the rise of many new

optimization techniques new optimization algorithms are being used for form-finding and stability of tensegrities when multiple states of self-stress are involved as they add exponentially increased complexity [45–49].

With the various form and force-finding methods established came applications of prestressable structures other than tensegrities using the same principles of prestress. One of the most commonly used of these is the invention of prestressed concrete. The deflections and stresses of concrete buildings with varying levels of prestress are analyzed by both Ahmed [50] and Naser [51] using static response analysis while Mercan investigated prestressed concrete beams for their failure properties [52]. More recently, Moored investigates bio-inspired morphing wings using tensegrity principles to achieve desired displacements [53]. Sobek and Teuffel prove force and shape control of pin-jointed structures can reduce the effect of external loading [54]. Although optimizing the shape for static deflection and stress levels is extremely important in many applications it fails to encapsulate the whole problem, especially when dynamic loading is applied or the vibration response of the structure is important. For these reasons, tensegrity analysis is often extended for dynamic analysis.

2.2.2 Dynamic Response Applications

Research in dynamic analysis of prestressable structures is much less common than the static analysis counterpart due to the increased complexity of the problem. Dynamic analysis of tensegrities relies on a static analysis already being completed as the shape and forces are required to understand the dynamics of the structure. The theory of dynamic analysis of tensegrities will be presented further in Chapter 3: but put simply the increased stiffness, as a result of the prestress levels in the structure, will alter the dynamic equations of motion. Specifically, the stiffness matrix

will be altered to include an additional term that considers this added geometric stiffness, thus altering the natural frequencies of the structure and therefore the free and forced vibrational response. Figure 2.2 depicts the relationship between the static and dynamic analysis of prestressable structures.

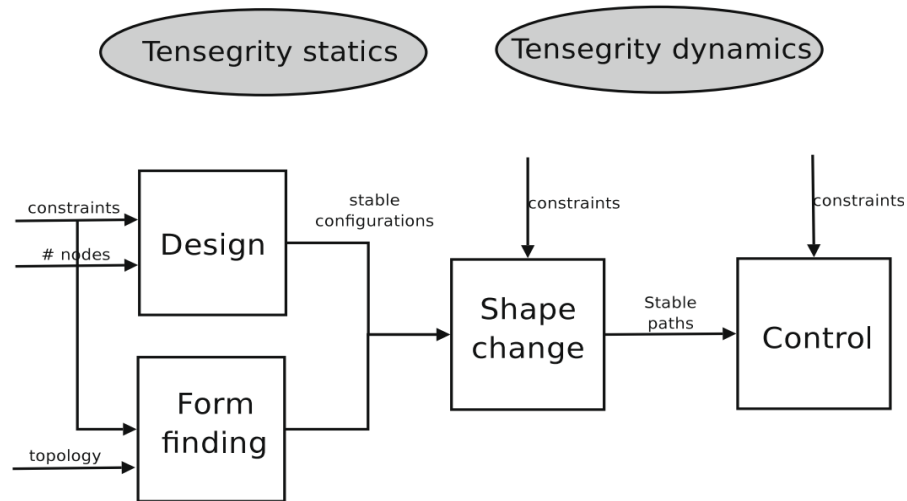


Figure 2.2 – Relationship between the static and dynamic analysis of tensegrities [55]

Using a lumped mass approach, the first dynamic analysis of a tensegrity was performed by Motro [56] and verified by experimental results on a simple tensegrity structure. Motro concluded that the natural frequency of the structure increased with the square of the prestress levels for mode shapes that correspond to infinitesimal mechanisms. For mode shapes corresponding to global bending modes of the structure the natural frequency changes negligibly with the level of prestress as the geometric stiffness is not capable of increasing the total stiffness a meaningful amount. Additional studies done by Mousa [57], Khala [58], and Murakami [59] confirmed Motro’s result. However, Ashweari later conducted experiments in 2014 on many tensegrity structures and determined Motro’s theory was not fully developed [60]. Ashweari added that whether the

tensegrity was cable or strut dominant also determined the relationship between the natural frequencies and level of prestress in the active members.

Another extremely important step forward in the field was the formulation of the force and shape influence matrices by Yuan [61]. Yuan uses the integrated nonlinear force method to develop a direct relationship between the prestressed state of a structure and the changes in elemental forces and nodal displacements with external loading. Yuan also develops a formulation to determine the minimum number of required actuators for desired force and/or displacement control. However, this requires the desired response to be known in terms of force and/or displacement output and mathematically tests the feasibility of an actuator layout configuration. Senatore, Reksowardojo, and Wang extend this theory to design adaptive structures with minimum whole-life energy as well as structures that can adapt to loads through large shape changes [62–66]. Senatore et al. investigate the effects of both permanent loads and live loads using these force and shape control methods with actuators, a summary of the process is shown in Figure 2.3.

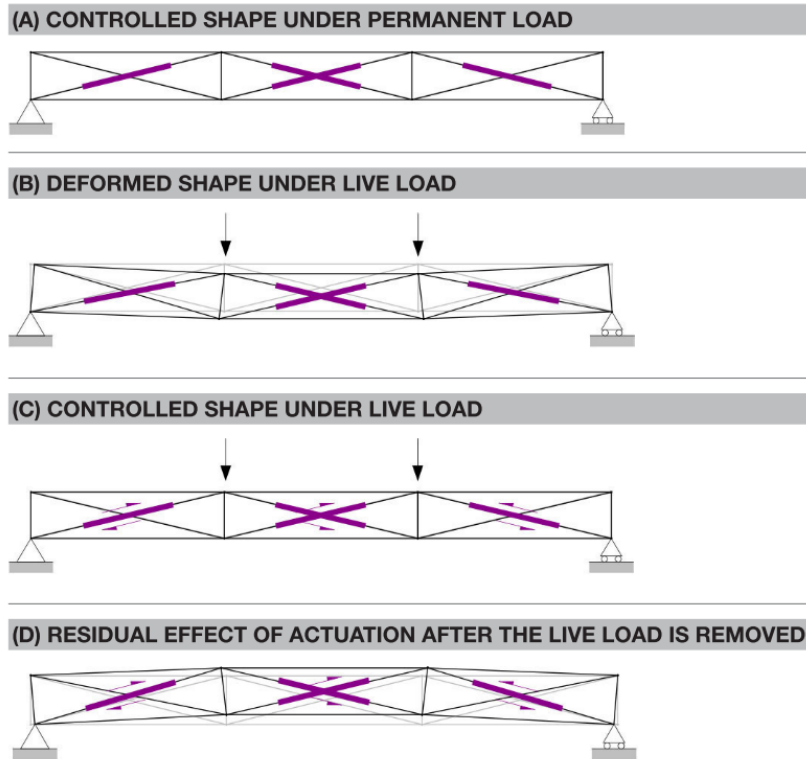


Figure 2.3 – Effect of actuation on prestressable structures under loading [63]

However, both Yuan and Senatore apply these control strategies for desired shape change or for minimum energy structures, not for vibration attenuation, which will be the focus of this thesis. Vibrational attenuation is the natural evolution when considering applications of the dynamic analysis of tensegrities and has been extensively researched. Xiadong analyzes a 2D tensegrity beam for vibration control under seismic excitation [67]. Rasool creates a variable stiffness composite panel using varying levels of mechanical prestress and analyzes the aeroelastic response [68]. Hadj et al optimizes a tensegrity-based footbridge under dynamic loading [47]. Taylor uses a genetic algorithm to optimize the shape of a tensegrity beam for vibration suppression [69]. Other prestressable structure applications include Ashwear [70], Giurgiuttu [71], and Hu [72] using various methods of prestress for structural health monitoring and Suwala et al. using prestressed

strips in the floor of a rotorcraft to reduce local vibrations [73]. Similar to the use of optimization techniques for form-finding and stability analysis tensegrity structures can be tuned for vibration suppression. Amendola et al. [74] tune frequency band gaps of tensegrities using global prestress while Pal [75] tunes the wave propagation in a periodic tensegrity structure using prestress. However, no framework currently exists that performs dynamic aeroelastic analysis on a tensegrity structure using control actuations for vibration attenuation. Furthermore, no framework exists that uses this concept in the context of an optimization (single or multi-objective) problem to achieve the optimal response according to the application and designer's objectives. Therefore, the need for such a framework has been established as many aerospace and civil adaptive structures experience aerodynamic gust disturbances in the form of wind excitation profiles and could greatly benefit from optimized control actuators attenuating their response according to the desired performance objectives. The following chapters will present the necessary theory required to establish this proposed framework before explaining the implementation in software and presented case studies.

Chapter 3: Theoretical Framework Part I: Stiffening Effects of Geometric Nonlinearities

In structural analysis both material and geometric nonlinearities can occur. Material nonlinearities are present when the material exhibits nonlinear elastic, plastic, and/or viscoelastic behavior and alter the material stiffness matrix of the structure. Similarly, geometric nonlinearities can occur when structural deformations are sufficiently large enough (exceed the infinitesimal limit) to represent a force or shape change from the initial geometry or stress state and impose an additional stiffness termed the geometric stiffness. The geometric stiffness formulation based on standard finite element approaches is reproduced by multiple authors [76–79]. In practice, these geometric nonlinearities can be imposed through piezoelectric smart materials, hydraulic or pneumatic linear actuators, and various cable-tensioning techniques. This chapter will present the necessary theory for determining self-stress states and calculating the corresponding geometric stiffness matrix for a given geometry and active member length changes.

3.1 Determinacy Analysis and Geometric Stiffness Finite Element Formulation

The equilibrium matrix of a structural geometry with nel number of elements can be analyzed using singular value decomposition (SVD) to identify static and kinematic properties of the geometry. These properties can then be used with standard determinacy analysis computations to determine the effect of geometric nonlinearities in the structure through the introduction of active members length changes on the systems dynamic response [24].

The equilibrium method of determinacy analysis requires a few key assumptions: the geometry of the structure in terms of nodal coordinates is known, elements are connected by pin joints, external

loads and the self-weight of the structure are neglected, there are no dissipative forces acting on the system, and both local and global buckling are neglected. These assumptions then allow an expression for nodal equilibrium equations to be found for each bar element k containing a node i and node j [80]:

$$(\mathbf{C}^T \mathbf{Q} \mathbf{C}) \mathbf{x}_i = \mathbf{f}_i \quad (3.1)$$

where \mathbf{C} defines the connectivity of the structure's geometry based on the \mathbf{x}_i vector of x , y , and z nodal coordinates. \mathbf{Q} is a square diagonal matrix containing force to length ratios, denoted force density, for each bar element on the main diagonal and zero elsewhere which are respectively in equilibrium with the applied external load vector \mathbf{f}_i .

$$\mathbf{C}_{k,p} = \begin{cases} 1 & \text{if } p = i \\ -1 & \text{if } p = j \\ 0 & \text{otherwise} \end{cases} \quad (3.2)$$

Utilizing the above assumption of negligible external load allows the right-hand side of Equation 1 to be idealized as zero, resulting in the formulation of the equilibrium matrix, \mathbf{A} , that defines all bar element force density sets that are in static equilibrium as:

$$\mathbf{A} = \mathbf{C}^T \begin{bmatrix} \mathbf{c}_x \\ \mathbf{c}_y \\ \mathbf{c}_z \end{bmatrix} \quad (3.3)$$

where \mathbf{c}_x , \mathbf{c}_y , \mathbf{c}_z are the main diagonal elements of \mathbf{C} that correspond to the x , y , and z nodal coordinate locations, respectively. Once the equilibrium matrix of the structure is established the degree of static indeterminacy, s , and corresponding states of self-stress can be found by taking the SVD of \mathbf{A} [24]. SVD is an extremely useful technique for determinacy analysis as spectral

decomposition is only possible for $[n \times n]$ square matrices and indeterminate structures inherently have a non-square equilibrium matrix. SVD factorizes a matrix into three separate constituent matrices that generalize the spectral decomposition to work for any $m \times n$ matrix and provides information on important characteristics of the equilibrium matrix. The three constituent matrices of SVD are the left singular vectors matrix $[\mathbf{U}_r \quad \mathbf{U}_q]$, singular matrix $\begin{bmatrix} \mathbf{V}_r & \mathbf{0} \\ \mathbf{0} & \mathbf{0} \end{bmatrix}$, and right singular vectors matrix $[\mathbf{W}_r \quad \mathbf{W}_s]$ which are expressed together as:

$$\mathbf{A} = [\mathbf{U}_r \quad \mathbf{U}_q] \begin{bmatrix} \mathbf{V}_r & \mathbf{0} \\ \mathbf{0} & \mathbf{0} \end{bmatrix} [\mathbf{W}_r \quad \mathbf{W}_s]^T \quad (3.4)$$

For an equilibrium matrix, \mathbf{A} , \mathbf{U}_r is the basis of the column space and defines the range of all loads in equilibrium with the \mathbf{W}_r row space of \mathbf{A} . Crucially, \mathbf{U}_q is the left null space (null space of \mathbf{A}^T) while \mathbf{W}_s is a matrix whose s columns pertain to the individual self-stress modes, equivalently found from the null space of the equilibrium matrix.

The self-stress modes are a non-dimensional set of $[nel \times 1]$ per-element factors that represent all possible combinations of internal forces in equilibrium with an $[nel \times 1]$ vector of zero applied load, hence the term self-stress. Finally, \mathbf{V}_r represents the square roots of the non-negative eigenvalues. Using these decomposed vectors, a system of compatibility equations equivalent to Equation (3.3) can be formed as per [24]:

$$(\mathbf{W}_s^T \mathbf{G} \mathbf{W}_s) \alpha = -\mathbf{W}_s^T \left(\mathbf{G} \sum_{i=1}^s \frac{\mathbf{U}_{r_i}^T \Delta \mathbf{p}}{\mathbf{V}_{r_i}} \mathbf{W}_i + \boldsymbol{\varepsilon}_0 \right) \quad (3.5)$$

where \mathbf{G} is the flexibility matrix, $\boldsymbol{\alpha}$ is a vector of s free parameters that represent a weighted factor linear combination of the s states of self-stress, and \mathbf{W}_s is indexed from 1 to s by the variable i . Additionally, $\Delta\mathbf{p}$ is a vector of applied element forces, and $\boldsymbol{\epsilon}_0$ is a vector of per-element initial strains. The summation term presented in Equation (3.5) represents a stress-system in equilibrium with the applied load vector and can be simplified using matrix notation to the following Moore-Penrose pseudo-inverse of the equilibrium matrix [64]:

$$\mathbf{A}^+ = \mathbf{W}_r \mathbf{V}_r^{-1} \mathbf{U}_r^T \quad (3.6)$$

Rearranging Equation (3.5) for $\boldsymbol{\alpha}$ and post-multiplying by \mathbf{W}_s gives the global state of self-stress, which defines the internal force change of each member in response to both initial strain (induced via active member length changes) and external applied load. Adding an additional term to include the change in element force directly from external applied load gives the total element force change, deemed the effective prestress as:

$$\mathbf{P}_{k_{eff}} = (\mathbf{W}_r \mathbf{V}_r^{-1} \mathbf{U}_r^T) \Delta\mathbf{p} - \mathbf{W}_s \left[(\mathbf{W}_s^T \mathbf{G} \mathbf{W}_s)^{-1} \mathbf{W}_s^T (\Delta\mathbf{L} + \mathbf{G} (\mathbf{W}_r \mathbf{V}_r^{-1} \mathbf{U}_r^T) \Delta\mathbf{p}) \right] \quad (3.7)$$

where $\Delta\mathbf{L}$ is a design vector representing the length change induced in the active members, zero for non-active members, stemming from the initial strain $\boldsymbol{\epsilon}_0$. The first term represents the internal force change directly from the applied load on that element while the second term represents the summation of all other elements affecting this specific element, defined by the global state of self-stress. Interestingly, all variables other than $\Delta\mathbf{L}$ are intrinsic to the structural geometry or load scenario, thus rearranging Equation (3.7) for $\Delta\mathbf{L}$ and replacing $\mathbf{P}_{k_{eff}}$ with $\mathbf{P}_{k_{MAX}}$ which is easily

found from maximum allowable tensile stresses in the member gives an interesting result: the maximum allowable length change in each element to maintain structural integrity, which is calculated as:

$$\Delta \mathbf{L}_{MAX} = \left[\frac{\mathbf{P}_{k_{MAX}} - (\mathbf{W}_r \mathbf{V}_r^{-1} \mathbf{U}_r^T) \Delta \mathbf{p} + \mathbf{W}_s (\mathbf{W}_s^T \mathbf{G} \mathbf{W}_s)^{-1} \mathbf{W}_s^T \mathbf{G} (\mathbf{W}_r \mathbf{V}_r^{-1} \mathbf{U}_r^T) \Delta \mathbf{p}}{-\mathbf{W}_s (\mathbf{W}_s^T \mathbf{G} \mathbf{W}_s)^{-1} \mathbf{W}_s^T} \right] \quad (3.8)$$

where

$$\mathbf{P}_{k_{MAX}} = \frac{\sigma_{MAX} * \mathbf{A}_{CS}}{SF} \quad (3.9)$$

where σ_{MAX} is the tensile yield strength, \mathbf{A}_{CS} is the cross-sectional area, and SF is a safety factor, all on an elemental basis. It is important to note that in practice the denominator of Equation (3.8), termed the force influence matrix \mathbf{S}_F , often does not have a unique solution and must be inverted either with the Moore-Penrose pseudo inverse or with a least squares minimization method [64], and can be easily done in MATLAB®. The next important formulation is the development of the geometric stiffness matrix using the elemental prestress. Defined per bar element k for a Euler-Bernoulli beam the geometric stiffness, \mathbf{K}_G , is as follows:

$$\mathbf{K}_G(k) = \frac{\mathbf{P}_{keff}(k)}{l_k(k)} \begin{bmatrix} 1 & 0 & 0 & 0 & 0 & 0 \\ 0 & 1 & 0 & 0 & -1 & 0 \\ 0 & 0 & 1 & 0 & 0 & -1 \\ 0 & 0 & 0 & 1 & 0 & 0 \\ 0 & -1 & 0 & 0 & 1 & 0 \\ 0 & 0 & -1 & 0 & 0 & 1 \end{bmatrix} \quad (3.10)$$

The geometric stiffness accounts for the added stiffness induced by the prestress and supplements the material stiffness matrix, \mathbf{K}_M , to give the total stiffness matrix, $\bar{\mathbf{K}}_{TOT}$, which is then assembled globally to represent the entire structure:

$$\bar{\mathbf{K}}_{TOT}(k) = \mathbf{K}_M(k) + \mathbf{K}_G(k) \quad (3.11)$$

Already briefly introduced, the force influence matrix, \mathbf{S}_F , defines the link between the active element length changes and the effective prestress in each member in the standard linear system form of $\dot{A}\dot{x} = \dot{b}$ and is defined as:

$$\mathbf{S}_F = -\mathbf{W}_s(\mathbf{W}_s^T \mathbf{G} \mathbf{W}_s)^{-1} \mathbf{W}_s^T \quad (3.12)$$

$$\mathbf{S}_F \Delta \mathbf{L} = \mathbf{P}_{keff} \quad (3.13)$$

which allows a simple input output relationship between the design variable, $\Delta \mathbf{L}$, and an output variable \mathbf{P}_{keff} to achieve a desired geometric stiffness. It is important to note that $\Delta \mathbf{L}$ defines only the applied length changes in the respective active element, not the resultant length change in the elements when multiple active elements are used. The relationship that defines the actual resulting changes in nodal positions, and subsequently length changes, is the shape influence matrix, \mathbf{S}_d . Similar to the linear form of the force influence matrix relationship, \mathbf{S}_d relates the active element length changes to the actual nodal position changes, $\Delta \mathbf{d}$, as:

$$\mathbf{S}_d = \mathbf{U}_r \mathbf{V}_r^{-1} \mathbf{W}_r^T \left[\mathbf{G} \left(-\mathbf{W}_s (\mathbf{W}_s^T \mathbf{G} \mathbf{W}_s)^{-1} \mathbf{W}_s^T \right) + \mathbf{I}_{nel \times nel} \right] \quad (3.14)$$

$$\mathbf{S}_d \Delta \mathbf{L} = \Delta \mathbf{d} \quad (3.15)$$

where $\mathbf{I}_{nel \times nel}$ is a $nel \times nel$ identity matrix. Remembering that the equilibrium matrix and therefore the states of self-stress are dependent on the nodal positions, if the resulting $\Delta \mathbf{d}$ from a set of $\Delta \mathbf{L}$ inputs is too large then the determinacy analysis must be redone in the new configuration, or a small amount of error must be accepted. This adds a second constraint to $\Delta \mathbf{L}$ on top of Equation (3.8). Now containing a constraint due to maximum allowed load for safety of the structure, and a constraint for assuring accurate analysis.

The above equations assume $\Delta \mathbf{L}$ is a $nel \times l$ vector, meaning that every element is active, which is often not the case due to material availability, configuration complexity, among other potential factors. The following section will introduce a new simplified method for determining optimal locations for active elements to be introduced into the structure and the effects that has on the force and shape influence matrices.

3.2 Optimal Location of Active Members

Determining the location of active elements is a necessary step in finding the optimal performance of an adaptive structure. However, optimal location analysis is usually done as a separate and prior process to the optimal actuation values for the objective of the problem, thus disjointing the location analysis from the ultimate goal of the adaptive structure [45,81,82]. Computational cost limits the problem from being an optimization problem within an optimization problem, but most

methods nevertheless run two separate optimization procedures, still greatly increasing the overall computational cost. Additionally, the dependence of the second design variable (optimal actuation length changes) on the first design variable (optimal actuator locations) prevents the formulation of a multi-objective optimization procedure. To avoid additional and especially compounding optimization problems within this framework a simpler determination of active member optimal locations is required. According to matrix multiplication rules, for an $m \times nel$ matrix, each column in $\mathbf{S}_F^{m \times nel}$ respectively multiplies an element in $\Delta \mathbf{L}^{nel \times 1}$ by a factor and the results are summed to produce the effective prestress, $P_{keff}^{nel \times 1}$. By evaluating the L1 norm of the factors in each column of $\mathbf{S}_F^{m \times nel}$ (which correspond to a single element in $\Delta \mathbf{L}^{nel \times 1}$) a comparison can be found that represents that respective element's overall effect on the effective prestress in the system. This is an important result as the level of prestress directly affects the geometric stiffness matrix and therefore the system response. Creating a vector $\mathbf{\Gamma}$ of this comparison metric in ascending order will then give a ranking of element effectiveness within a geometry for altering the geometric stiffness magnitude and correspondingly the system response.

$$\mathbf{\Gamma}_j = \sum_{i=1}^m |\mathbf{S}_F(i, j)| \quad (3.16)$$

$$\mathbf{\Gamma} = \max_N(\mathbf{\Gamma}_j) \quad (3.17)$$

where i and j represent the current row and column of an $m \times nel$ matrix, respectively. The designer can then choose the N best elements from $\mathbf{\Gamma}$, which is in ascending order, as the optimal active element locations where N is a user-defined value of number of actuators based on need of control

or actuator availability. As well, Γ can be truncated to only include elements within a certain area of the structure if desired, limiting the potential candidates to certain areas based on implementation difficulty, available materials, target areas, etc. Once the active element locations have been determined it is then necessary to compute their respective constraints by modifying Equation (3.8). Both \mathbf{S}_F and $\Delta\mathbf{L}$ (and \mathbf{S}_d if desired) are truncated to \mathbf{S}_F^* and $\Delta\mathbf{L}^*$, respectively, by nulling the non-active elements in $\Delta\mathbf{L}$ and corresponding columns of \mathbf{S}_F .

$$\mathbf{S}_F^*(i, j \neq \Gamma) = [] \quad (3.18)$$

$$\Delta\mathbf{L}^*(i \neq \Gamma) = [] \quad (3.19)$$

$$\mathbf{S}_F^* \Delta\mathbf{L}^* = \mathbf{P}_{k_{eff}} \quad (3.20)$$

This is done to ensure the solution set of $\Delta\mathbf{L}^*$ being tested during an iteration will correspondingly give the $\mathbf{P}_{k_{eff}}$ assuming only the correct active members are active, for use in constraints and in simplifying the computation of Equation (3.7). An example of Equations (3.18) to (3.20) is given as Algorithm 2.2 for clarity.

Algorithm 2.2: Optimal Location of Active Members

Input: Shape Influence Matrix, S_F and Number of active elements, N

Output: Hierarchy Matrix, Γ

start

for $i = 1$ to nel (or subset of elements to choose from)

$$SSS_{sum}(i) = \text{sum}(\text{row } i \text{ of } S_F)$$

end

$\Gamma = SSS_{sum}$ **sorted** largest to smallest magnitude

select first N values of Γ

end

Now a subset of elements to become active can be chosen based on the number of desired active elements and the truncated analysis can be performed. In terms of complexity, each additional active element becomes an additional design variable in an optimization/tuning application which must also be considered.

Chapter 4: Theoretical Framework Part II: Dynamic Aeroelastic Response

Analysis of Complex Structures

As previously mentioned, dynamic aeroelastic analysis considers elastic, inertial, and aerodynamic forces when determining the structural response to a given excitation. The response of each degree of freedom is analyzed for every excitation frequency specified in the analysis, which for complex structures and/or wide excitation ranges results in long computation time and large output datasets. One common approach to combat this issue is reducing the order of the numerical model while maintaining a good correlation to the original high-fidelity model in terms of dynamic characteristics within a frequency range of interest. This chapter will cover the process of reducing a high-fidelity model to improve computation time while ensuring proper modal characteristics are maintained. Additionally, multiple aerodynamic disturbance models will be presented and discussed for use in dynamic aeroelastic analysis as excitation profiles. Finally, the theory involved in combining dynamic aeroelastic analysis with geometric stiffness tuning will be presented as well as the common outputs and post-processing approaches for use in applications.

4.1 Reduced Order Models

One of the most common methods of model order reduction for finite element models, and the one used in this work, is Craig-Bampton model order reduction (CBMOR) based on the Rayleigh-Ritz approach in modal analysis. CBMOR uses Ritz vectors to improve the accuracy-cost and accuracy-time ratios for structural dynamics [83]. CBMOR produces simplified matrices of the high-fidelity model's modal characteristics based on its mass, stiffness, and damping matrices for the nodes of interest. The nodes of interest are the degrees of freedom to be kept in the CBMOR matrices which are altered from the high-fidelity matrices to capture the effect of the non-kept degrees of freedoms

on the mass, stiffness, and damping, respectively. In its most simplified form, a finite element model with mass $\bar{\mathbf{M}}$, damping $\bar{\mathbf{C}}$, and stiffness \mathbf{K}_{TOT} has a second order response in the Laplace domain using the Laplace operator, \hat{s} , as:

$$\left[[\bar{\mathbf{M}}]\hat{s}^2 + [\bar{\mathbf{C}}]\hat{s} + [\bar{\mathbf{K}}_{\text{TOT}}] \right] \{q(\hat{s})\} = [b]\{u(\hat{s})\} \quad (4.1)$$

$$\{y(\hat{s})\} = [c]\{q(\hat{s})\} \quad (4.2)$$

where the actual outputs, y , are a linear combination, c , of the generalized degrees of freedom, q , and the input matrix b scales the time/frequency dependent input force, u . For model order reduction the generalized degrees of freedom within the finite element model can be approximated by a subset of degrees of freedom of interest, q_r , according to the Ritz/Galerkin displacement method through a transformation matrix \mathbf{T} [83]:

$$\{q\} \approx [\mathbf{T}]\{q_r\} \quad (4.3)$$

This approximation assumes zero virtual work in the dual subspace generated by $[\mathbf{T}]^T$ therefore the reduced models second order response in terms of the subset of degrees of freedom of interest is:

$$\left[[\mathbf{T}]^T[\bar{\mathbf{M}}][\mathbf{T}]s^2 + [\mathbf{T}]^T[\bar{\mathbf{C}}][\mathbf{T}]s + [\mathbf{T}]^T[\bar{\mathbf{K}}_{\text{TOT}}][\mathbf{T}] \right] \{q_r(s)\} = [\mathbf{T}]^T[b]\{u(s)\} \quad (4.4)$$

$$\{y(s)\} = [c][\mathbf{T}]\{q_r(s)\} \quad (4.5)$$

This is an important result as the relationship between q and q_r is constant according to \mathbf{T} regardless of the excitation of the structure/loading scenario. This means the calculation converting the full DOF set to the DOF subset must be performed only once, while the dynamic aeroelastic response of the structure can be calculated for varying excitations (and/or geometric stiffness configurations) according to Equation (4.4) using only the subset of degrees of freedom to characterize the system response. This will improve computation cost and time for each response analysis, which will become essential in Chapter 5: in the context of an optimization algorithm with a large amount of iterations and potential design variables.

To achieve this improved process, one must first determine the conversion matrix, \mathbf{T} , to get the reduced model. The two main assumptions to do so are: the model must be valid over a restricted frequency band, and the number of inputs must be limited. This is because the accuracy between q and q_r is dependent on the frequency range for which the reduced order model must be similar to the original. In simpler terms, a ROM that is only required to be analyzed for one natural frequency and subsequent mode shape can be significantly more accurate to the original high-fidelity model than a ROM that must characterize the original model's response for a large number of natural frequencies/mode shapes. The derivation for \mathbf{T} can be found in [83] and will not be reproduced herein.

Once the ROM has been established it is crucial to validate the new model within the framework of the intended analysis. One of the most common methods to do so is by calculating the modal assurance criterion (*MAC*). The *MAC* defines a correlation coefficient between two sets of mode shapes, one set produced by the original high-fidelity model and one set produced by the new ROM. The *MAC* is a statistical indicator based on a least squares form of linear regression analysis

and outputs a value between 0 and 1, with 0 representing no correlation and 1 representing full correlation. The *MAC* is the normalized scalar product of the two sets of mode shapes and can be calculated according to [84] as:

$$MAC(HF, ROM) = \frac{|\{\boldsymbol{\varphi}_A\}_{HF}^T \{\boldsymbol{\varphi}_X\}_{ROM}|^2}{(\{\boldsymbol{\varphi}_A\}_{HF}^T \{\boldsymbol{\varphi}_A\}_{HF})(\{\boldsymbol{\varphi}_X\}_{ROM}^T \{\boldsymbol{\varphi}_X\}_{ROM})} \quad (4.6)$$

where $\{\boldsymbol{\varphi}_A\}_{HF}$ are the mode shapes of the high-fidelity model and $\{\boldsymbol{\varphi}_X\}_{ROM}$ are the mode shapes of the ROM. Again, the mode shapes in Equation (4.6) are a subset of the total mode shapes for each model corresponding to the desired frequency range of interest. The designer can decide how close the *MAC* must be to 1 to constitute an acceptable ROM, with again the difficulty of accuracy being dependent on the frequency range of interest and the amount of reduction of the degrees of freedom in the system.

4.2 Aerodynamic Disturbance Models

Testing adaptive aerospace structures under realistic excitations is pertinent to understanding the behavior and level of effectiveness from the adaptations made. For many aerospace structures these realistic excitations come in the form of turbulence and wind gust disturbances that can have a large effect on the structure's dynamic response. Atmospheric disturbances near the ground (under ~1600 ft elevation) arise as the result of either turbulence due to friction, wind shear, or by solar heating from the ground and can be understood by various wind gust models [85]. For structures within the atmospheric boundary layer the Davenport Spectrum is the most widely accepted model for continuous turbulence in power spectral density analysis as it considers ground

effects and is captured via Equations (4.7) through (4.9). A uniformly distributed load acts on the lifting surfaces of the structure for a specified mean wind gust, v_m .

$$S_D(\omega) = 4800v_m\kappa \frac{\beta\omega}{(1 + (\beta\omega)^2)^{\frac{4}{3}}} \quad (4.7)$$

$$\beta = \frac{600}{\pi v_m} \quad (4.8)$$

$$\kappa = \frac{1}{\left(2.5 \ln\left(\frac{z}{z_0}\right)\right)^2} \quad (4.9)$$

where $S_D(\omega)$ is the velocity spectral density as a function of frequency and κ is the surface drag coefficient with mean height of structure z and height of surface roughness z_0 . The total wind velocity is the combination of both the mean wind velocity, v_m , and the gust velocity, Δv :

$$\mathbf{v} = \mathbf{v}_m + \Delta \mathbf{v} \quad (4.10)$$

To compute the total wind gust velocity with a davenport spectrum disturbance, Δv is found using a fourth order filter to approximate S_D and applying a white noise input.

Similarly, the most common discrete wind gust disturbance model used in TDG analysis is the one-minus-cosine (OMC) model and is expressed according [86] as:

$$\Delta v(t) = \frac{v_{g0}}{2} \left(1 - \cos \left(\frac{2\pi v_m t}{L_g} \right) \right) \quad (4.11)$$

where $\Delta v(t)$ is the wind incremental velocity as a function of time, t ; v_{g0} is the peak gust disturbance, and L_g is the gust scale length. Compared to the DS model requiring white noise input, the gust velocity can be directly computed as a function of time and the total wind velocity can then be found once again via Equation (4.10). In the next section these two models will be used in conjunction with the modal equations of motion to determine a structure's dynamic aeroelastic response.

4.3 Dynamic Aeroelastic Equations of Motion with Geometric Nonlinearities

Utilizing the formulation for aerospace structural control in a realistic environment demands software that can perform dynamic aeroelastic analysis and the necessary atmospheric disturbance model to test within. MSC NASTRAN® contains a dynamic aeroelasticity solution sequence (SOL 146) with the capability to perform such analysis. For a specified finite element model of an aerospace structure and aerodynamic load profile the aerodynamic matrices, including aerodynamic loads, are computed at each user-defined Mach number and dimensionless reduced frequency pair, (\hat{m}, \hat{k}) [87,88]. To perform these calculations SOL 146 takes advantage of the double lattice method (DLM) which is based on linearized aerodynamic potential theory. This greatly simplifies the analysis compared to high-fidelity computational fluid dynamics based on Navier-Stokes's equations.

The goal of the DLM is to create a set of aerodynamic influence coefficients (AIC) and spline them to the structural geometry through interpolation, thus capturing the effects of aerodynamic

loading on the structural response. The DLM creates aerodynamic elements which are regions of lifting surfaces or bodies that occur in streamwise arrays. Each aerodynamic element is divided into small trapezoidal lifting surfaces (boxes) such that the boxes are arranged in strips parallel to the free stream. Each box is comprised of a uniform acceleration potential doublet at the $\frac{1}{4}$ box chord length and an aerodynamic grid point at the $\frac{1}{2}$ box chord length. In MSC NASTRAN® the $\frac{1}{4}$, $\frac{1}{2}$, and $\frac{3}{4}$ chord lengths are indexed as ‘ i ’, ‘ j ’, and ‘ k ’, respectively.

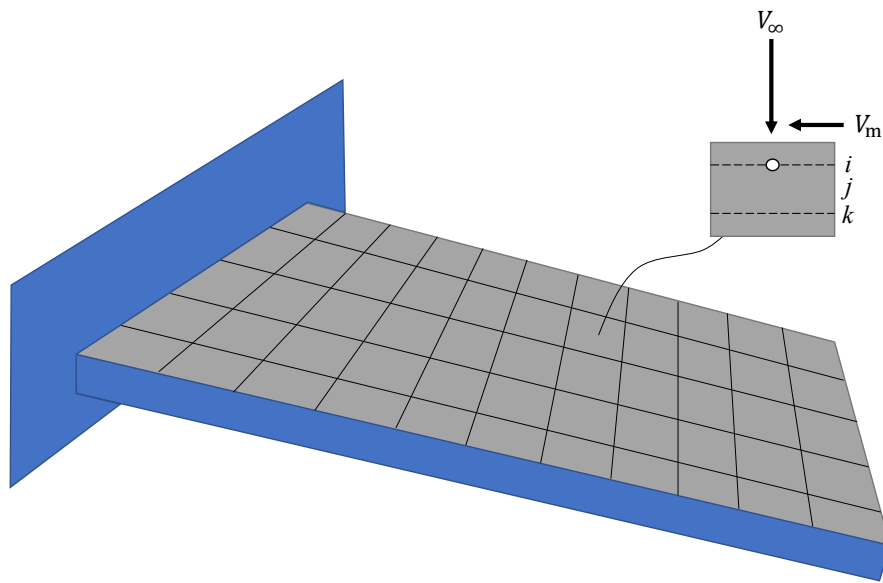


Figure 4.1 – Example DLM panel for a cantilever beam wing

From Figure 4.1, the individual trapezoidal boxes shape is dependent on the overall shape of the DLM panel and the box distribution, appearing square for a square wing. The induced downwash forcing function, w_j at j of each lifting surface (box) is then related to a complex pressure coefficient, Δc_p , derived from circulation strength by the AIC [89]. The downwash forcing function will be modeled by the DS in the frequency domain and TDG in the time domain for the purposes of this work.

$$\Delta c_p = \left(\text{AIC}(\hat{m}, \hat{k}) \right) (w_j) \quad (4.12)$$

$$\hat{k} = \frac{c_{ref} \omega}{2V_\infty} \quad (4.13)$$

where (\hat{m}, \hat{k}) are again the Mach number and dimensionless reduced frequency pair, c_{ref} is the reference airfoil chord length, ω is the circular frequency, and V_∞ is the free-stream velocity. Additionally, downwash can be computed via the substantial differentiation matrices, \mathbf{D}^1_{jk} and \mathbf{D}^2_{jk} , of the deflections, u_k . \mathbf{D}^1_{jk} and \mathbf{D}^2_{jk} represent the dimensionless real and imaginary parts, respectively.

$$w_j = [\mathbf{D}^1_{jk} + ik\mathbf{D}^2_{jk}]u_k + w_j^g \quad (4.14)$$

where w_j^g is the static aerodynamic downwash consisting of the static incidence distribution that may arise from an initial angle of attack, camber, or twist [87]. Next, the lifting pressure f_j is integrated using the \mathbf{S}_{kj} integration matrix to obtain subsequent aerodynamic forces, F_k , and moments as presented in Equation (4.15). This result is then combined with Equations (4.12) and (4.14) to obtain the aerodynamic force influence coefficient matrix, \mathbf{Q}_{kk} , at the aerodynamic grid points according to:

$$F_k = \mathbf{S}_{kj}\{f_j\} \quad (4.15)$$

$$\mathbf{Q}_{kk} = \mathbf{S}_{kj}[\mathbf{AIC}]^{-1}[\mathbf{D}_{jk}^1 + ik\mathbf{D}_{jk}^2] \quad (4.16)$$

To develop the relationship between \mathbf{Q}_{kk} and the structural grid points either a surface (curved or planar) or linear beam spline matrix, \mathbf{G}_{kd} , must be employed to interpolate between the two grid point sets per Equation (4.17). This is because the aerodynamic grid set and the structural grid set are created independently and generally do not coincide. Once this relationship between structural deformation and aerodynamic forces is established it can be converted to modal coordinates according to Equation (4.18) for use in the global aeroelastic equation of motion.

$$\mathbf{Q}_{dd} = \mathbf{G}_{kd}^T \mathbf{Q}_{kk} \mathbf{G}_{kd} \quad (4.17)$$

$$\mathbf{Q}_{hh} = \boldsymbol{\varphi}_i^T \mathbf{Q}_{dd} \boldsymbol{\varphi}_j \quad (4.18)$$

Both flutter and dynamic aeroelastic analysis are possible in MSC NASTRAN® and utilize the following equation of motion for a harmonic modal response $\mathbf{q}(\omega)$:

$$\left[\mathbf{M}_{hh} \omega^2 + i\mathbf{B}_{hh} \omega + (1 + ig)\bar{\mathbf{K}}_{hh} - \frac{1}{2} \rho V_\infty^2 \mathbf{Q}_{hh}(m, k) \right] \mathbf{q}(\omega) = \mathbf{P}(\omega) \quad (4.19)$$

$$\mathbf{P}(\omega) = \boldsymbol{\varphi}_i^T \mathbf{F}(t) + \frac{1}{2} \rho V_\infty^2 [\boldsymbol{\varphi}_i^T \mathbf{G}_{kd}^T \mathbf{S}_{kj} \mathbf{AIC}] \mathbf{w}_j \quad (4.20)$$

where the load vector $\mathbf{P}(\omega) = 0$ for flutter analysis and can be supplied in either the frequency or time domain. The first term of which corresponds to non-aerodynamic forces such as structural loading in modal coordinates, while the second term covers all aerodynamic forces. \mathbf{M}_{hh} , \mathbf{B}_{hh} ,

$\bar{\mathbf{K}}_{hh}$, $\mathbf{Q}_{hh}(\hat{m}, \hat{k})$ are the modal mass matrix, modal damping matrix, modified modal stiffness matrix, and aerodynamic force matrices, respectively. The modal stiffness matrix \mathbf{K}_{hh} is modified to $\bar{\mathbf{K}}_{hh}$ to include the geometric stiffness formulated above, which is directly added into SOL 146's total stiffness via direct matrix input (DMIG). While all MSC NASTRAN® aeroelastic analysis is done in the frequency domain for simplicity based on the dependence of ω , when $\mathbf{P}(\omega)$ is supplied in the time domain a Fourier Transform is performed to convert to the frequency domain for analysis before Inverse Fourier Transforming to return to the time domain for outputting results. However, if additional calculations are required of the frequency domain outputs then they must first be shifted to a time consistent set, **TCX**.

4.4 Time Consistent Outputs

Dynamic aeroelastic analysis is by default performed in the frequency domain for MSC NASTRAN® and only converted to time domain analysis using Fourier Transforms if outputs are requested as such. For frequency-dependent outputs a necessary conversion must be performed to shift the outputs (forces, displacements, accelerations, etc.) to time consistent values while still in the frequency domain. This is done to allow for meaningful manipulation of the outputs ensuring the correct magnitudes of respective components are used for subsequent calculations. The first step is done by identifying a key output of interest (for example the maximum degree-of-freedom-displacement) and designating its respective circular frequency as the critical frequency, ω_{crit} [cycles/sec], and critical phase, φ_{crit} [degrees] as the instance of interest. From there, all other respective outputs can be converted to a time consistent set at that instance through a phase shift per Equations (4.21) through (4.23).

$$\Omega_{crit} = 360 * \omega_{crit} \quad (4.21)$$

$$t_{crit} = \frac{\varphi_{crit}}{\Omega_{crit}} \quad (4.22)$$

$$\mathbf{TCX} = \mathbf{X}_{\omega=crit} * \cos((\Omega_{crit}t_{crit} - \varphi_{\omega=crit})) \quad (4.23)$$

where Ω_{crit} and t_{crit} are the frequency in degrees per second and the time corresponding to the critical (of interest) frequency and phase, respectively. **TCX** represents a generic output where X can be load, displacement, etc., and $\mathbf{X}_{\omega=crit}$ and $\varphi_{\omega=crit}$ are the magnitude and phase at Ω_{crit} of the output being shifted, done for each degree of freedom. Algorithm 3.4 is given to illustrate the overall process.

Algorithm 3.4: Time Consistent Outputs from Dynamic Aeroelastic Analysis

Inputs: Nodal output magnitudes per excitation frequency, ω and the corresponding phase, φ

Output: Time consistent outputs, **TCX**

start

Define ω_{crit} , φ_{crit} as excitation frequency [cycles/sec] and phase [deg] corresponding to maximum output magnitude

$t_{crit} \rightarrow$ Equation (4.22)

for $i_{node} = 1$ to # of nodes

for $i_{DOF} = 1$ to # of degrees of freedom

TCX{ i_{node}, i_{DOF} } \rightarrow Equation (4.23);

end

end

end

Once the time consistent outputs have been established their use in post-processing analyses is imperative to understanding the system response. They will be used to determine the objective functions for the given design variable set and any performance metrics for defining suitability.

After the dynamic aeroelastic response analysis has been performed and the time consistent outputs have been calculated it is important to post-process the results to find meaningful relationships and characteristics of the structure. Nodal displacements can be used to create a frequency response function (FRF) for PSD analysis and time response function (TRF) for TDG analysis. The displacement amplitude is plotted for a given range of excitation frequencies to depict that respective nodes dynamic response, for which these functions can be plotted with varying design variable sets and compared. It is important to note that for the nodal FRF's the use of time

consistent displacements is not necessary as the dependence is simply on the excitation frequency, and for TRF's the displacements are already a time consistent set. However, for any performance metrics that make use of multiple nodal displacement sets the time consistent displacements must be used after frequency analysis to ensure the proper displacements are being compared. A summary of the model's use in the dynamic aeroelastic analysis is given below in Figure 4.2.

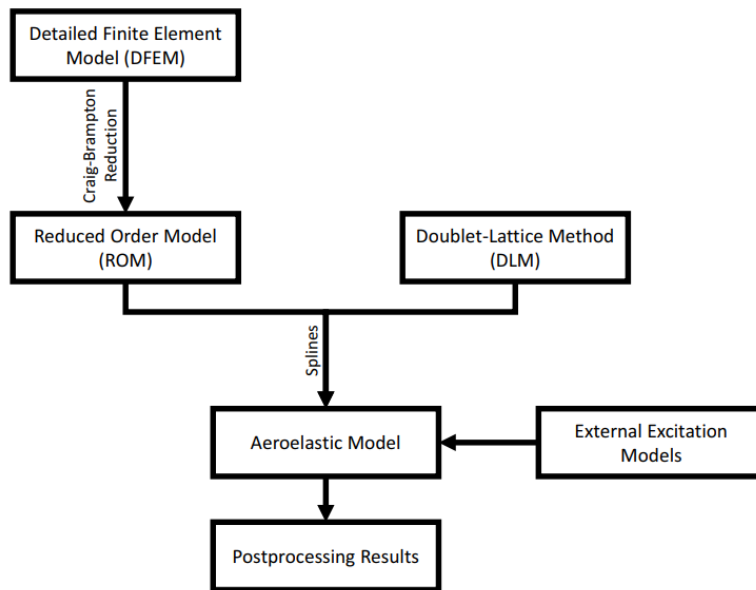


Figure 4.2 – Map of models used in dynamic aeroelastic analysis [90]

As previously mentioned, the FRF's, TRF's, and any post-processing calculations are all dependent on the dynamic response displacements. Subsequently, these displacements are dependent on the total geometric stiffness defined by the design vector set of element length changes in the active elements as derived in Chapter 3.1. Therefore, finding the optimal dynamic response requires the power of an optimization algorithm to determine the optimal design vector within user-defined constraints. The following chapter will discuss the process of both single and multi-objective optimization via genetic algorithms.

Chapter 5: Theoretical Framework Part III: Genetic Algorithm Optimization

The proposed methodology uses a genetic algorithm to converge to the optimal solution. Genetic algorithms are a type of popular stochastic search algorithm based on the mechanisms of natural genetics, selection, and evolution [91]. GA's start with a randomly populated solution set where each individual solution in the set is made up of chromosomes, which will evolve through successive iterations, known as generations. The initial population can either be randomly defined between a set of given bounds or manually defined by the user if certain areas of the total solution space are to be avoided or are known. Offspring are created from the chromosomes to form the population of the next generation and are determined by evaluating each chromosome on some measure of fitness. The best chromosomes from the previous generation, called parents, are either modified using a mutation operator or merged to create the offspring of the next generation, where the population size will stay consistent. After successive generations, the algorithm will converge to the best possible chromosome within the solution set based on the fitness criterion, representing the optimal solution to the problem. Figure 5.1 illustrates the general process of a genetic optimization algorithm. Determining if the objective function is satisfactory is based on the user-defined stopping criteria, usually defined as either a specific value of the objective function or a convergence metric found from the best individual of each generation not changing within a certain tolerance.

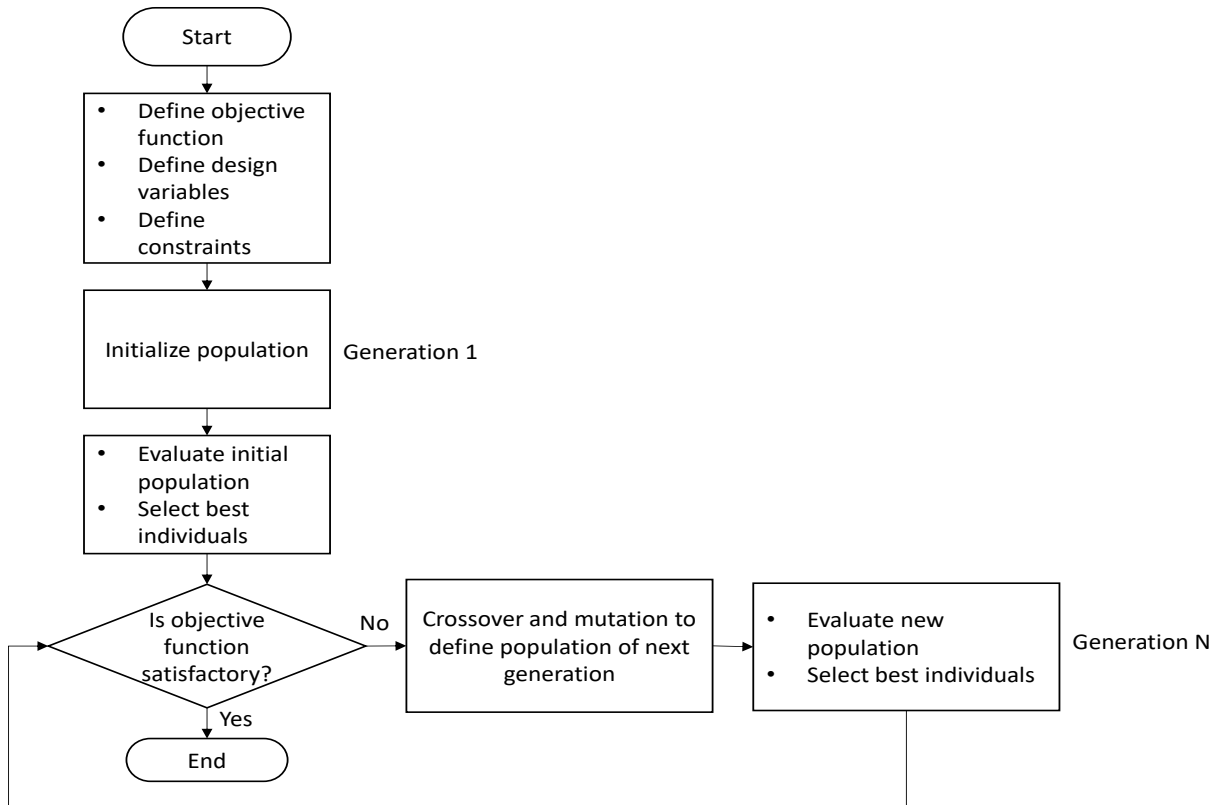


Figure 5.1 – Flowchart process of a general genetic algorithm

5.1 Genetic Algorithm Parameters

The five main phases in a genetic algorithm are the initial population, function evaluation, selection, crossover, and mutation, with the final three constituting the evolution of the optimal solution. After each individual (usually stored in binary as a string of 1's and 0's) is evaluated based on the fitness function, a subset is selected to breed the new generation. Most selection criteria heavily weigh the fitness of the individuals with fitter solutions being more likely to be selected, however, less-computationally expensive methods employ a simple random selection process. The fitness function is always problem-dependent and can be a combination of one or more objective functions dependent on the design variables. Usually, the fitness values for each

individual are normalized with respect to the total sum of fitness values of that generation. This is done as a check once all fitness values in a generation are evaluated to ensure the accumulated normalized fitness value is unity. Many selection methods are available, the most popular of which are summarized as follows [92]:

- Roulette Wheel Selection – the probability of an individual being selected is directly proportional to its fitness value as a random selection is made with weights proportional to the fitness value. This can be thought of as spinning a roulette wheel with one slice per individual, the size of which is defined by its fitness value, hence the name. The wheel is spun a user-defined amount of times, N_s , equal to the number of individuals desired for selection.
- Tournament Selection – a randomly chosen subset of the population is defined (constituting the tournament) and the best individual within that subset is deemed the winner and is selected. This is repeated N_s times.
- Truncation Selection – a proportion equal to $\frac{N_s}{\text{population size}}$ is defined and the individuals in that top percentage are chosen for selection.

Once the selected individuals have been chosen, they must crossover (sometimes referred to as recombination) to the next generation to establish the new population to be evaluated. However, simply reusing those selected individuals in the next generation provides no new information and can lead to failed optimization. The selected individuals are instead defined as parents of the new population to increase diversity by combining, hence recombination, the parents in different ways to create the new population. The genetic information of the chromosomes in the parents is stored in bit arrays and used in the various crossover methods:

- One-point crossover – two parents are randomly picked then a point is randomly chosen in both as the crossover point. Points to the right of that crossover point within the bit array are swapped between parents to produce two new offspring.
- k-point crossover – two parents are randomly picked then two or more points are randomly chosen in both as the crossover points. Points between the k crossover points are swapped.
- Uniform crossover - two parents are randomly picked then each bit within the parents has an equal probability of swapping. Other weighted probabilities of swapping, termed mixing ratios, may also be used.

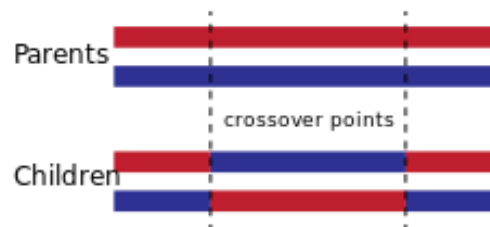


Figure 5.2 - k-point crossover visualization of parent and offspring chromosomes [92]

Finally, mutation may also occur after selection of the parent individuals to increase genetic diversity throughout the optimization. Genetic diversity helps mitigate the chance of the algorithm getting stuck in local minima. A mutation probability is defined by the user and represents the chance mutation will occur during crossover. This is usually a small probability to not hinder the effectiveness of the selection process in converging to the optimal values. If mutation occurs, one or more chromosomes within a parent is mutated to a random value and the rest of the algorithm continues. The next section will discuss how evaluation of the fitness for each individual differs when more than one objective is introduced into the genetic algorithm.

5.2 Multi-Objective Genetic Algorithms

For problems with multiple objectives involved, a multi-objective genetic algorithm (MOGA) can be used in place of the original GA. An example of this is MATLAB®'s *gamultiobj* function which uses a controlled elitist genetic algorithm. An elitist GA always favors individuals with the best fitness values while a controlled elitist GA favors individuals with good fitness values but that also increase the diversity of the population. Now that more than one objective function is involved in determining the fitness of an individual a few new terms must be introduced to assist the higher order situation. The rank of an individual determines the chance of selection of an individual and is based on the principle of dominance. A point x dominates a point y (y inferior to x), for a vector-valued objective function f , when $f_i(x) \leq f_i(y)$ for all i and $f_j(x) < f_j(y)$ for some j , where i and j are separate objectives. Individuals with rank 1, meaning they are not dominated by any other individuals, make up what is known as the Pareto front. The Pareto front represents a set of individuals that are all considered optimal solutions to the MOGA but with varying levels of optimality between the multiple objectives. No individual is best in all objectives, each has a trade-off between the conflicting objectives. It is then the designer's decision based on problem-specific factors to choose the specific individual within the Pareto front as the best individual.

Alternative to designer choice, many selection criteria exist for determining the best individual among the Pareto front. The most commonly used method is based on L_p norms and calculates the distance from the Pareto front to an ideal "utopian" point, the individual with the shortest distance corresponding to the best individual [93,94]. Among these the most common is the L_2 norm which is equivalent to the Euclidean distance. When calculating the distance different weights may be applied to the objective functions depending on the designer's choice.

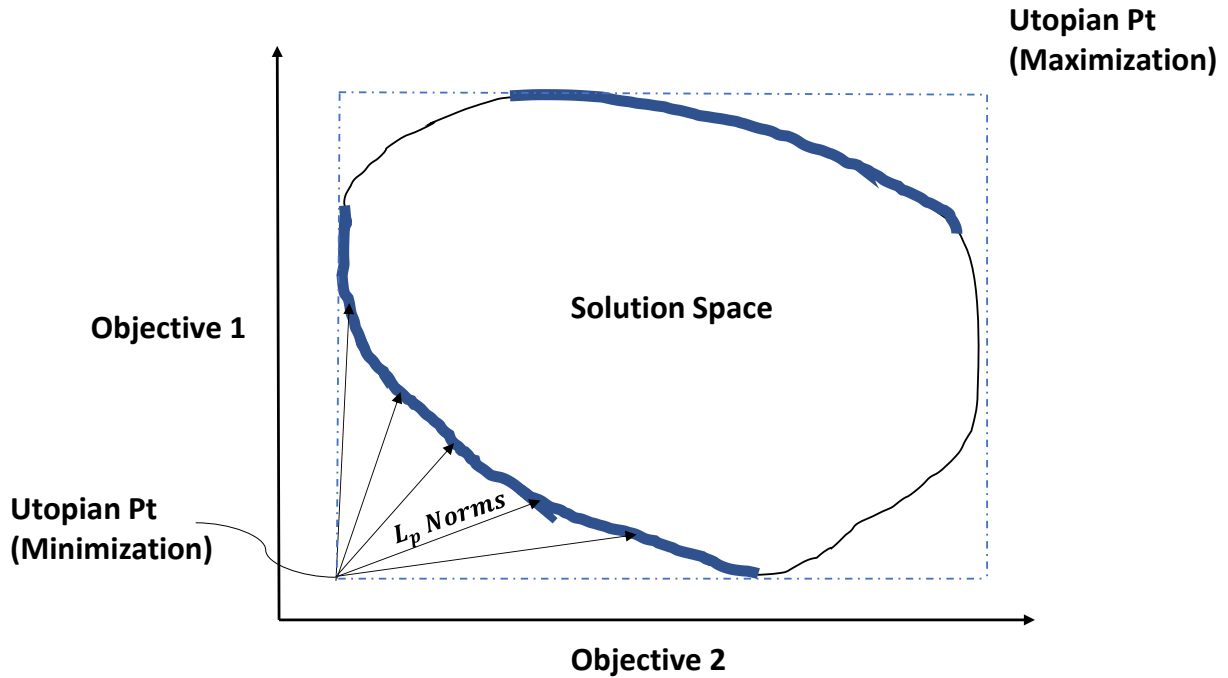


Figure 5.3 - Pareto front and Utopian point method for maximum and minimizations of MOGA

The utopian point method is useful for both maximization and minimization objective functions and defines a quantitative selection method opposed to designer-choice. This method is effective for any number of objectives in the MOGA but as the number of objectives increases the weights applied to each becomes increasingly important to achieve a meaningful utopian point.

Chapter 6: Software Implementation of Proposed Framework

Now that the relevant theory has been established for the proposed framework it is crucial to explore how the theory will be combined to achieve the desired outcome of optimizing the dynamic aeroelastic response of structures using geometric nonlinearities and how it will be implemented in software.

6.1 Implementation in MATLAB and NASTRAN

As previously mentioned, the proposed framework leverages the capabilities of both MATLAB® and NASTRAN® to iteratively perform the required complex calculations. Before optimization an initial determinacy analysis and active member location analysis per Chapter 3, as well as MOGA initialization must be performed. For the determinacy analysis MATLAB®'s built in SVD function allows quick determination of the states of self-stress and subsequently the force influence matrix according to Chapter 3.1. Using this force influence matrix, the optimal location of active members can then be determined according to Chapter 3.2. Once the active member locations are determined an initial determinacy analysis is performed for a design vector of zero length changes in the active elements and the problem specific MOGA optimization is initialized by defining all MOGA parameters. This initialization includes the definition of the fitness function (objective functions), calculation of all constraint equations (whether bounds, linear inequalities, and/or nonlinear inequalities), and initial values of the fitness function via calculation of the fitness function with an empty design vector.

For optimization, as mentioned in Chapter 5, MATLAB®'s built-in *ga* or *gamultiobj* are used for single or multi-objective genetic algorithm optimizations, respectively. The fitness function to

be minimized carries out all necessary steps to take a design vector of active element actuations and output the aerodynamic response of the degrees of freedom of interest.

6.2 Overall Design Procedure for the Optimization of Geometric Nonlinearities

For a structure with active elements Γ , the fitness function, design variables, and constraints are as follows:

$$\begin{aligned}
 \text{Fitness function:} & \quad \text{Minimize } \eta \\
 \text{Design variables:} & \quad \Delta \mathbf{L} \\
 \text{Constraints:} & \quad \mathbf{S}_F^* \Delta \mathbf{L}^* \leq \mathbf{P}_{k_{MAX}} \\
 & \quad -\Delta \mathbf{L}_i \leq \%length(i) \leq \Delta \mathbf{L}_i
 \end{aligned} \tag{6.1}$$

where η is any function of the dynamic aeroelastic response defining performance and $\mathbf{P}_{k_{MAX}}$ is the maximum allowable prestress in either tension or compression defined by Equation (3.7) and (3.9). The objective functions used in the case studies are the minimization of overall pointing error and the minimization of total strain energy in the system and will be discussed further in chapter 7.1 and 8.1. The first inequality constraints, plural due to each element being compared against its respective $\mathbf{P}_{k_{MAX}}$, are implemented to satisfy the force influence matrix and yield strengths as discussed in Chapter 3.1. Similarly, the bound constraints are implemented to satisfy the shape influence matrix as discussed in 3.1, limiting the actuations by some factor of their length to ensure the structure is not displaced too far from its original geometry to introduce errors large

errors in the determinacy analysis. The overall process for the proposed optimization procedure is presented in Figure 6.1 showing important steps and necessary inputs.

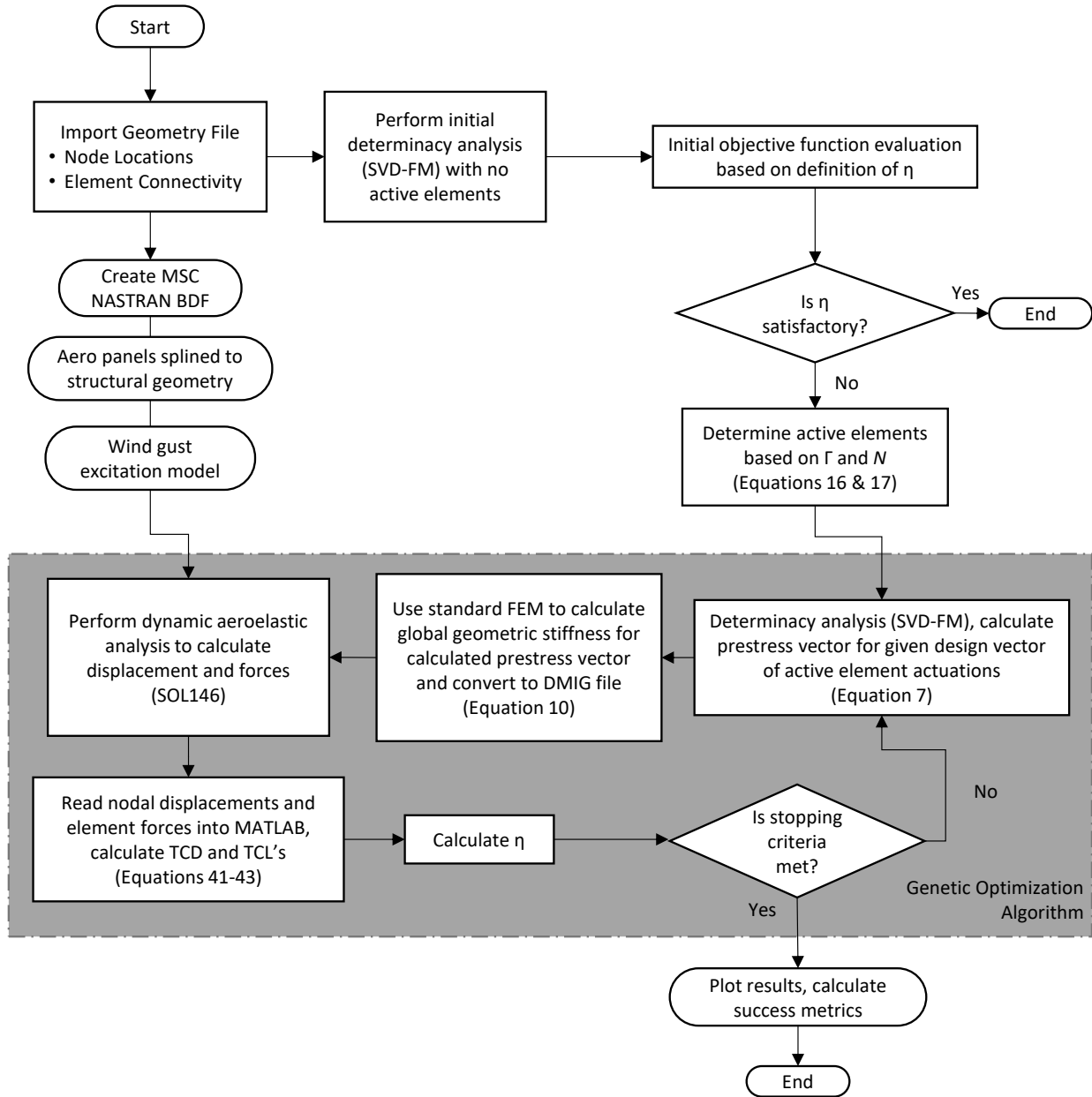


Figure 6.1 – Detailed process diagram for the framework of optimizing geometric nonlinearities using a genetic algorithm for attenuation of the dynamic aeroelastic responses of structures

With all necessary inputs in place the algorithm performs an initial objective function calculation using a design vector of zeroes to determine required action and establish a performance baseline. The active element actuations are then optimized based on a comparison of the objective function η to the user-defined stopping criteria, which is usually based on ensuring convergence to the global minimum of the fitness function. Finally, plots and performance metrics are calculated to establish the level of success of the framework. The necessary inputs for the geometry of the structure include the node locations and element connectivity, as well as all cross-sectional areas and material properties. These inputs are used to create the NASTRAN® bulk data file (BDF) which specifies the structure, the type of dynamic analysis whether PSD or TDG, the desired outputs, and any other data files to include. Two other input data files required to include are: the DLM aero panel distribution with associated splines between the structural and aerodynamic geometry, and the atmospheric disturbance excitation model being considered. The objective (or fitness) function $\eta = f(\Delta L^*)$ is created such that the objective function can be minimized according to a single design vector of ΔL^* , where the user-defined stopping criteria is compared after each generation. To further explain the steps involved in the framework Figure 6.2 is presented.

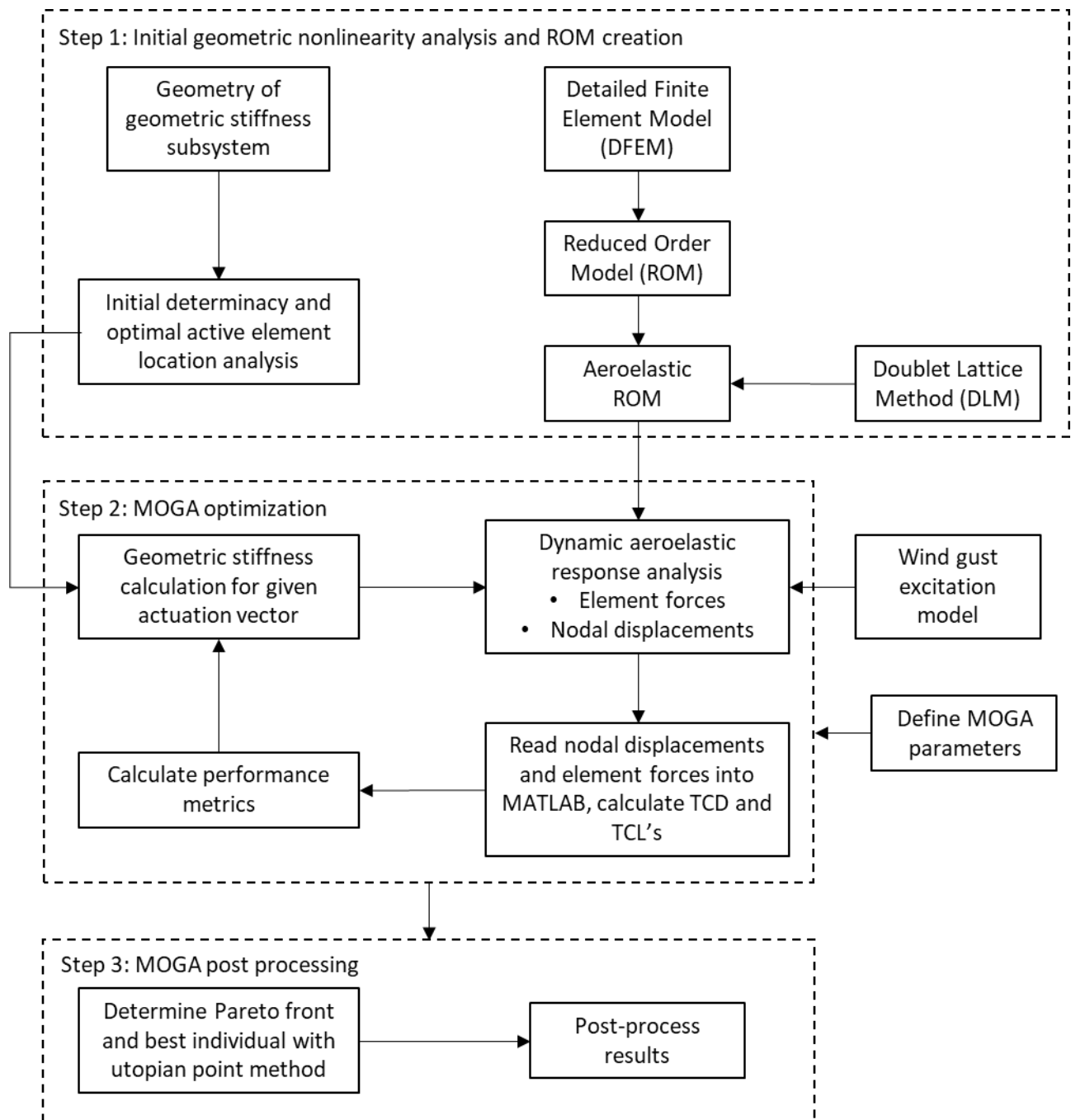


Figure 6.2 – Step breakdown of proposed performance optimization framework

In step 1, the geometry of the system for which geometric stiffness calculations are to be performed on is inputted into MATLAB®. Equivalently, the reduced order finite element model of the system is inputted into NASTRAN® and used to create the reduced aeroelastic model using the CB-MOR

and DLM process. An initial determinacy analysis with zero actuations is calculated and an optimal active element location analysis is performed. In step 2, in the confines of a single or multi-objective genetic optimization algorithm the geometric stiffness is iteratively tested via active element actuations to determine the actuations that give the best dynamic aeroelastic response. In step 3 the results from the optimization are post-processed. For a MOGA the utopian point method is used to determine the best individual.

One of the most important aspects of the framework is the link between the MATLAB® analysis in the context of the genetic algorithm, and the dynamic aeroelastic analysis in MSC NASTRAN®. During each function evaluation of the GA or MOGA where an individual is being tested the MATLAB® script must create a Direct-Matrix-Input (DMIG) file that can be read by NASTRAN®'s SOL146 to add the calculated geometric stiffness into the system, as the BDF only contains the material stiffness matrix and the request for a DMIG file. MATLAB® must then call the NASTRAN® BDF to perform SOL146 and output the results into MATLAB®-readable files. NASTRAN® outputs the results into a .pch (punch) file with displacements and/or forces for each degree of freedom at each excitation frequency (or time) interval. Once the .pch file has been fully populated MATLAB will then use built-in text file reading and regular expression matching functions to bring the data into strings and matrices within the workspace, for manipulation in post-processing as discussed in Chapter 4.4. From there, the objective functions of that individual are evaluated, requested figures are plotted, and the produced files from the current run are deleted in preparation for the next iteration.

6.3 Framework Validation

To ensure the proposed framework is properly operating it must first be validated. To do so the reference model of a simple triplex tensegrity unit consisting of 3 struts and 9 cable members with geometry from Yildiz [19] was analyzed with varying prestress in the struts between 0.4 MPa and 2 MPa to prove the algorithm correctly identifies the effect of prestress on the natural frequencies and mode shapes. With the top three members fully fixed as boundary conditions a single state of self-stress was identified, thus being the only factor towards the global state of self-stress and can be visualized in Figure 6.3 with the respective magnitudes of axial force densities in each member labelled. A single internal mechanism was identified and can be seen in Figure 6.4 with both the original and displaced configurations.

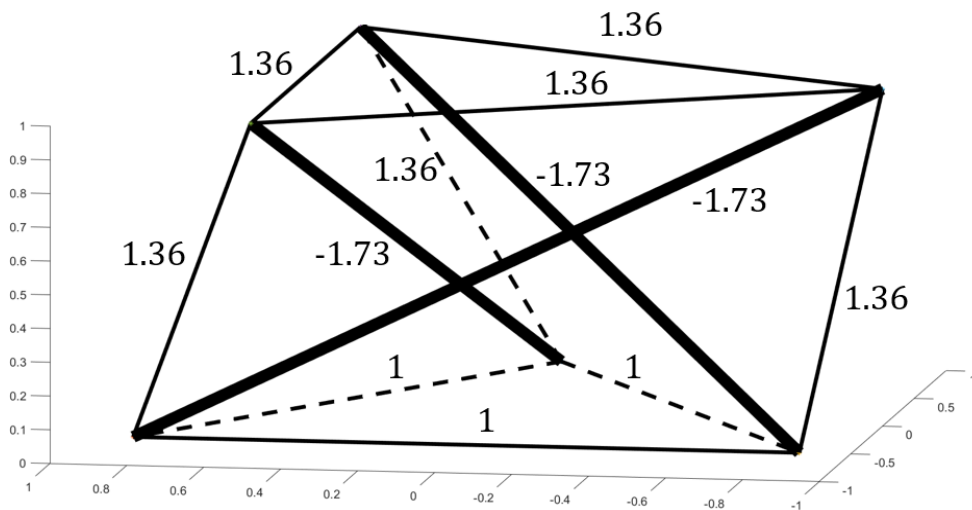


Figure 6.3 - Global state of self-stress for simple triplex tensegrity

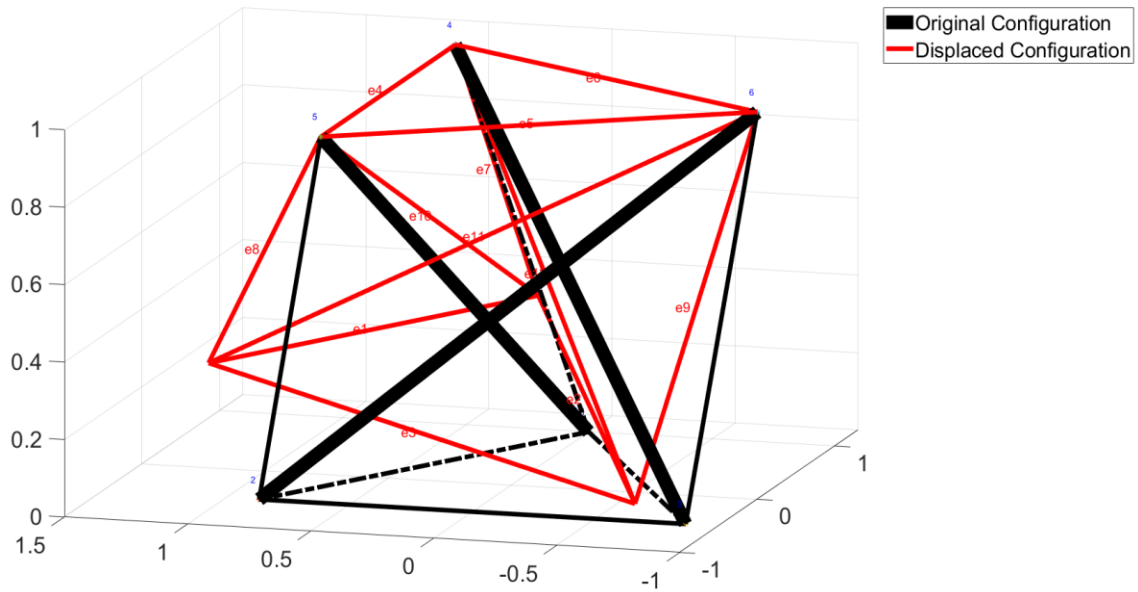


Figure 6.4 - Internal mechanism mode for simple triplex tensegrity

The trends of the first six natural frequencies of the tensegrity vs the corresponding prestress magnitude are displayed in Figure 6.5 and agrees with the results from [19]. It can be seen that only the first natural frequency is heavily shifted by an increase in prestress while the higher vibrational modes are governed by the axial stiffness of the individual members and are therefore less responsive to changes in prestress, only negligibly increasing for the triplex unit. This is expected as the lower frequencies always correspond to the infinitesimal mechanisms which are heavily influenced (stiffened) by the level of prestress proportional to the square root of the stiffness and subsequently, prestress.

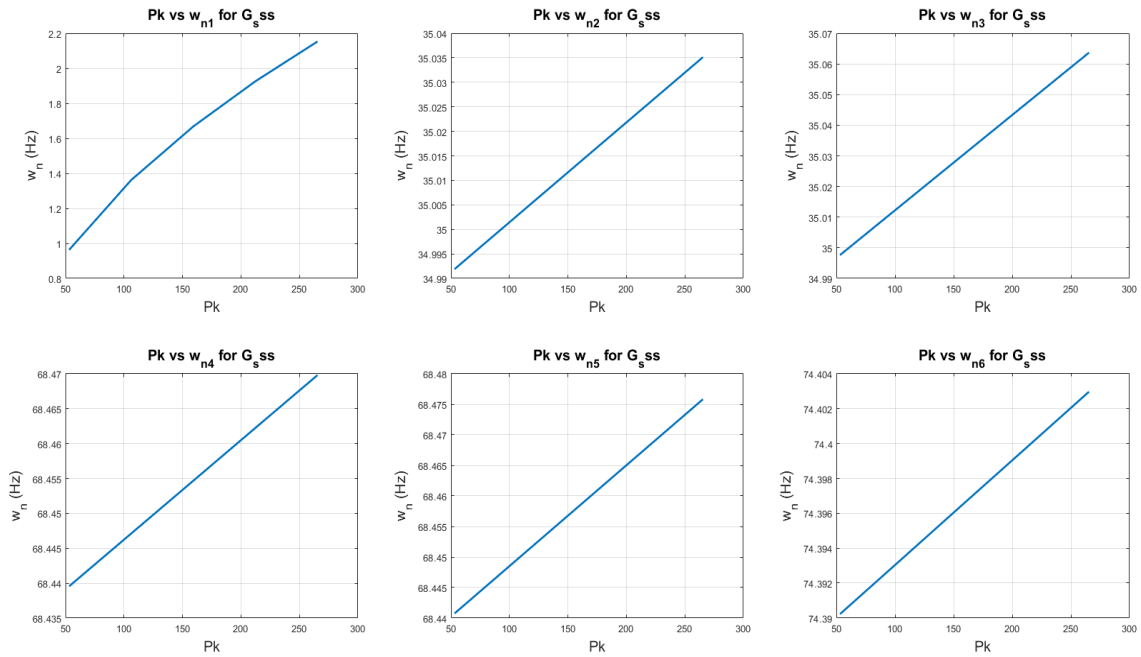


Figure 6.5 - Effect of prestress on the first six natural frequencies of a simple triplex tensegrity

It is also worth noting the pairs of natural frequencies after the first; this is due to the high levels of symmetry within the tensegrity structure. The natural frequencies of a tensegrity structure can be thought of as a nearness to buckling in one or more of its compressed components [70,95].

Chapter 7: Case Study I: Attenuation of the dynamic aeroelastic response of a Simplified VLBI antenna model using a single-objective genetic optimization algorithm

A case study was performed using the proposed optimization algorithm on a simplified Very-Long Baseline Interferometry (VLBI) antenna structure with the objective of decreasing the overall pointing path deviation angle when subjected to atmospheric disturbances. VLBI is a geometrical technique based on the synthetic aperture radio observation method used in radio astronomy in which an array of earth antenna ground stations simultaneously target a space radiation signal source to obtain high fidelity imaging [96–99]. The difference in time delay of the wavefronts reaching the individual antennae is used to calculate their baseline length and stitch together a more accurate radio image with the effective aperture of the distance between ground stations. VLBI also has many geodesic applications and for either radio source the pointing accuracy is pivotal to the signal clarity [100]. Ground station antennas are comprised of complex support truss structures as well as boom-arm truss structures to connect primary and secondary reflectors offset from one another thus making them ideal candidates for the proposed optimization framework.

Using time consistent loads the effect of the applied load was considered in the calculation of the structure's geometric stiffness while time consistent displacements were used to calculate the antenna's pointing path deviation angle, which is to be minimized. Pointing error is calculated according to Equations (7.1) through (7.4) and serves as the single objective function, η , for this case study [6].

$$\theta = \tan^{-1} \left(\frac{\text{TCD}_{x,\text{target node}}}{|\Delta L_{\text{target node-reference node}}|} \right) \quad (7.1)$$

$$\phi = \tan^{-1} \left(\frac{\text{TCD}_{y,\text{target node}}}{|\Delta L_{\text{target node-reference node}}|} \right) \quad (7.2)$$

$$\psi = \tan^{-1} \left(\frac{\text{TCD}_{z,\text{target node}}}{|\Delta L_{\text{target node-reference node}}|} \right) \quad (7.3)$$

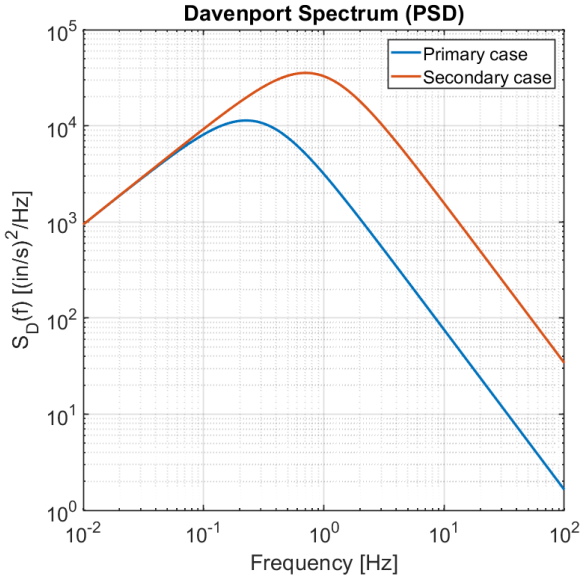
$$\eta_{\text{pointing error}} = \sqrt{\theta^2 + \phi^2 + \psi^2} \quad (7.4)$$

θ , ϕ , and ψ are the deviation angles in the X, Y, and Z directions, respectively. The target node and reference node will be discussed further in Chapter 7.1. This case study will introduce the subject antenna model, the optimization parameters used, and discuss the results for both frequency domain response with DS and time domain response with OMC.

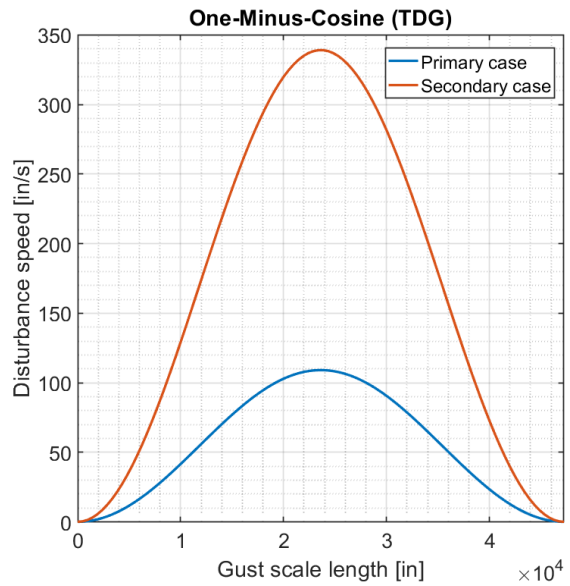
Two subcases of atmospheric disturbance will be analyzed and are termed the primary and secondary operational cases, respectively. The operational cases were defined by The National Aeronautics and Space Administration (NASA) and the industrial partner based on potential installation locations and are summarized in Table 7.1 and Figure 7.1 [101].

Table 7.1 - Primary and Secondary Operating Cases

<i>Operating Case</i>	<i>Mean Wind Speed</i>	<i>Disturbance Speed</i>	<i>Dynamic Pressure</i>	<i>Mach Number</i>
	[in/s]	[in/s]	[lb_f/in^2]	
Primary	349.95	109.10	0.005686	0.02615
Secondary	1093.61	339.20	0.055524	0.08173



a)



b)

Figure 7.1 - Operating case excitation profiles for a) DS and b) OMC gust models

7.1 Simplified Antenna Model and Optimization Parameters

The geometry used for this case study is comprised of 501 rod elements of 7075-T6 aluminum making up two main substructures: the supporting truss structure representing the primary reflector and subsequent supporting trusses, and the boom-arm system connecting the primary reflector to the secondary reflector. The total system geometry can be seen in Figure 7.2. The supporting truss structure consists of 25-inch-long elements in a triangular pattern forming a hexagonal array. Aerodynamic panels were placed on both the upper and lower halves of the hexagonal array on the supporting structures face. Each aero panel was then uniformly sectioned into 10 x 10 boxes for DLM analysis, totaling 200 aerodynamic lifting surfaces.

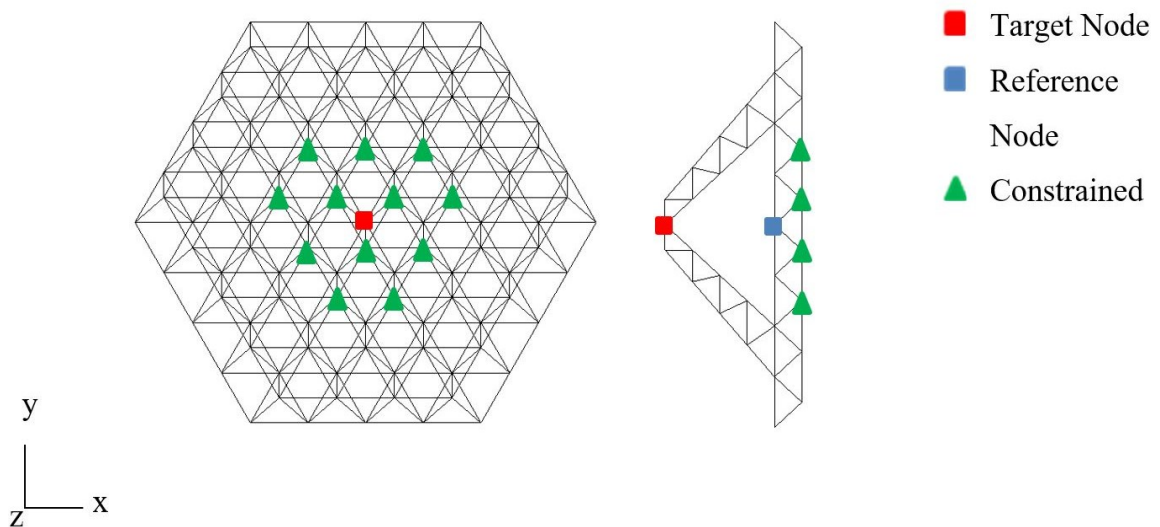
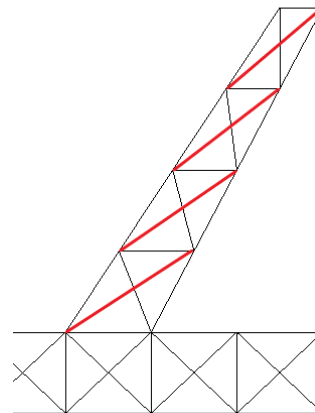


Figure 7.2 – Simplified VLBI antenna geometry with boundary conditions and important nodes

The boom-arms were designed to connect a secondary reflector placed 47.24 inches away from the surface of the primary reflector between the target node and the reference node and follow the pattern of the reference antenna shown in Figure 7.3. The target node and reference node are used for the pointing accuracy calculations as the signal clarity depends on their proper alignment. The constrained nodes are constrained in all three directions to eliminate all possible rigid body motion. A determinacy analysis was performed on the boom-arm subsystem and found no states of self-stress, leading to a lack of control through geometric stiffness tuning in the area. To overcome this, off-diagonal elements were added to induce a single state of self-stress in each boom-arm, allowing for the secondary reflector motion to be better controlled by the proposed method.



a)



b)

Figure 7.3 – a) InterTronic Solutions 12 m VLBI antenna [102] and b) Added diagonals required for geometric stiffness tuning

Modal analysis was performed on the modified geometry and found the systems first 5 natural frequencies with no prestress (a ΔL^* vector of zero actuations) to be 2.86 Hz, 2.97 Hz, 3.50 Hz, 4.08 Hz, and 4.57 Hz. Additionally, the initial response of the target node to both the DS and OMC primary and secondary cases are shown in Figure 7.5 through Figure 7.7 and will be discussed further in Chapter 7.2.

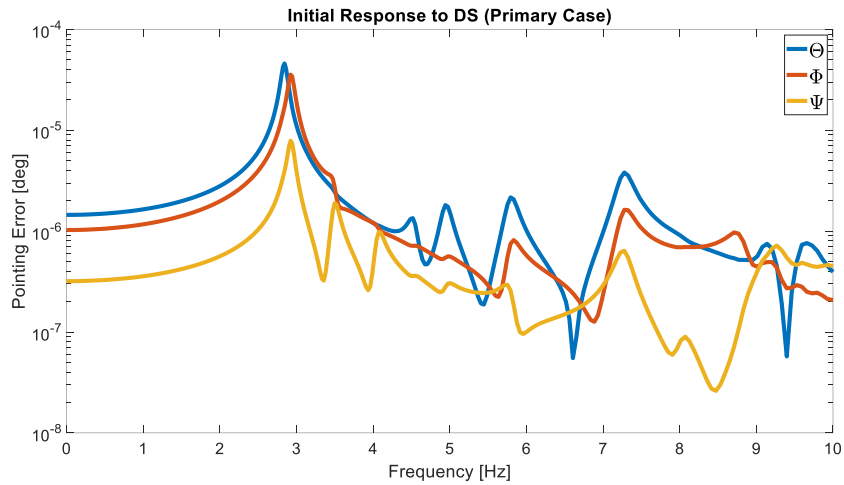


Figure 7.4 - Initial Response to DS Primary operating case

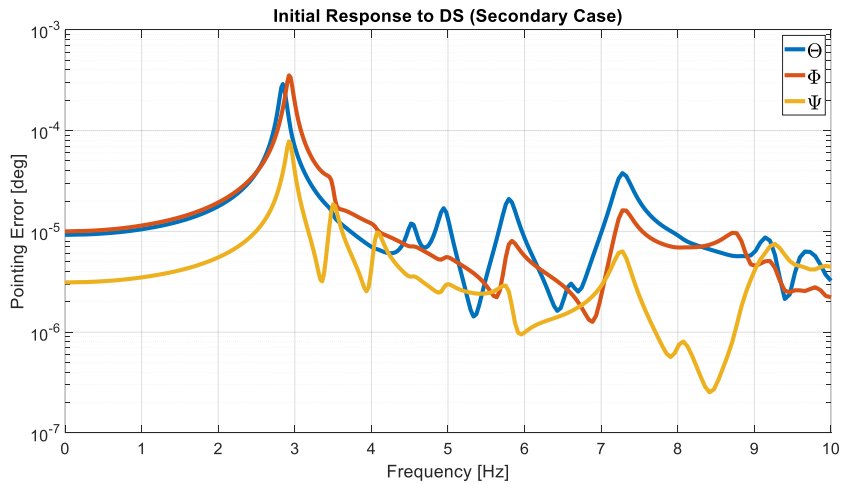


Figure 7.5 – Initial Response to DS Secondary operating case

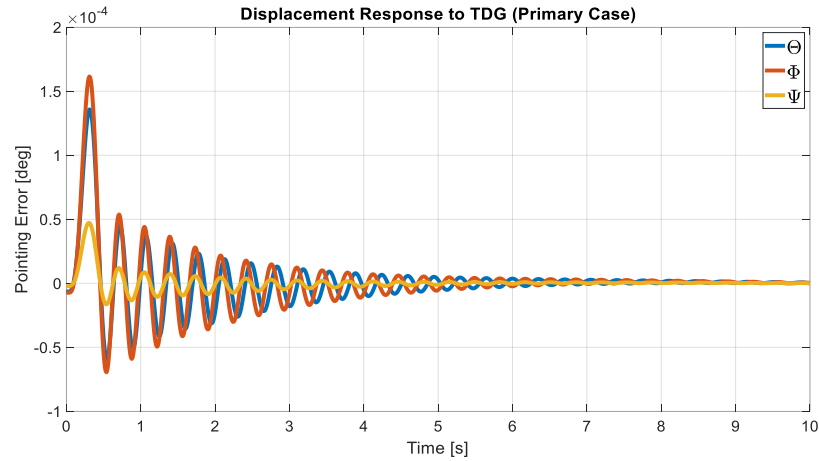


Figure 7.6 - Initial Response to OMC Primary operating case

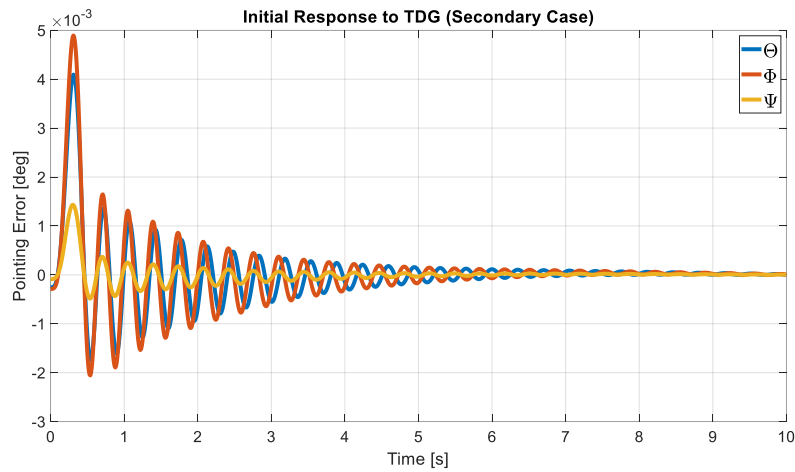


Figure 7.7 - Initial Response to OMC Secondary operating case

The dominant mode for this response can be seen at approximately 2.86 Hz, corresponding to the first natural frequency, while all other resonance peaks have much smaller amplitudes as can be seen by the vertical axes logarithmic scale. This frequency will thus serve as the critical frequency in the optimization algorithm and the amplitude will be minimized by shaping this dominant mode through the introduction of the active member length changes. The time response due to TDG will also be analyzed as the summation of the first 50 modes but will be heavily characterized by the

first dominant mode due to its large participation factor. Only the first 10 seconds are shown in Figure 7.7 as the amplitude response becomes negligible afterwards.

The constraints on this optimization case study are according to Equations (3.9) and (6.1) with $\sigma_{MAX} = 70$ [ksi] for the 7075-T6 aluminum [103] and a safety factor of 1.1. This ensures no element is stressed past its respective tensile limit. A population size of 300 (500 for systems with 64 active elements), 20 maximum generations, and MATLAB®'s default FunctionTolerance of 1E-06 for generational stopping criteria with 5 maximum stall generations were used for the GA optimization parameters. Based on the case studies objective function and due to ease of installation, possible actuator placement was limited to the boom-arm subsystem where three different actuator layouts were analyzed based on the number of active members desired. Systems with the best 16, 32, and 64 active elements according to Γ were analyzed and are summarized in Table 7.2 and Figure 7.8. A full sensitivity analysis can be done on this proposed optimization framework to determine the optimal number of actuators, N , using the proposed location metric Γ in addition to optimal actuator length changes either in the supporting truss structure, the boom arms, or both, but is out of scope of this work. The following sections will present the major results of this case study under each excitation model, operating case, and active member subcase.

Table 7.2 - Active Element Locations

<i># of Active Elements</i>	<i>Active Elements based on Γ</i>
16	<i>Red</i>
32	<i>Red + Green</i>
64	<i>Red + Green + Blue</i>

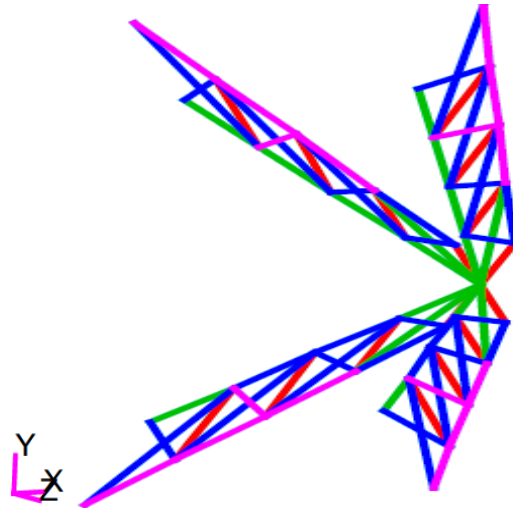


Figure 7.8 - Active element configurations for each analysis subcase

7.2 Results for Simplified Antenna Model

The proposed optimization procedure was performed for each layout subcase within each respective operational excitation case and the results are compared using frequency and time response functions per degree of freedom. It is important to note the total response cannot be calculated in the frequency domain without first shifting to time consistent outputs with equivalent

phases. The optimal actuator length changes were found by the framework through many generations of the GA, for which an example of convergence is presented in Figure 7.9

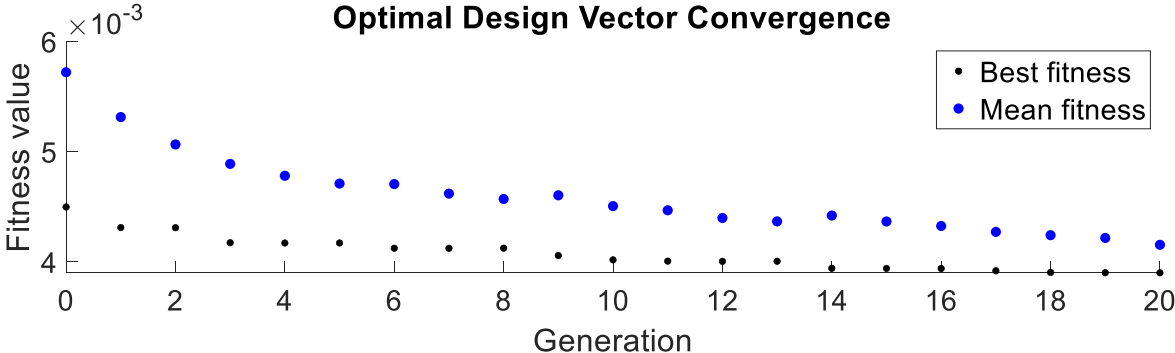


Figure 7.9 - Example of convergence of design vector through generations

These converged solutions then give the responses shown in Figure 7.10 and Figure 7.11 corresponding to the structure with optimal actuator length changes for each respective active element configuration subjected to DS.

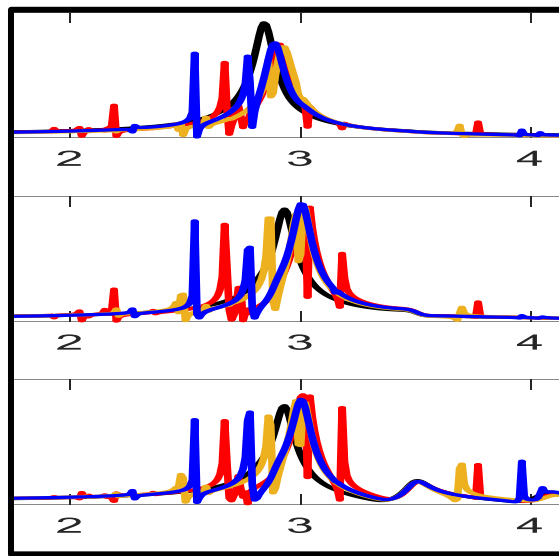
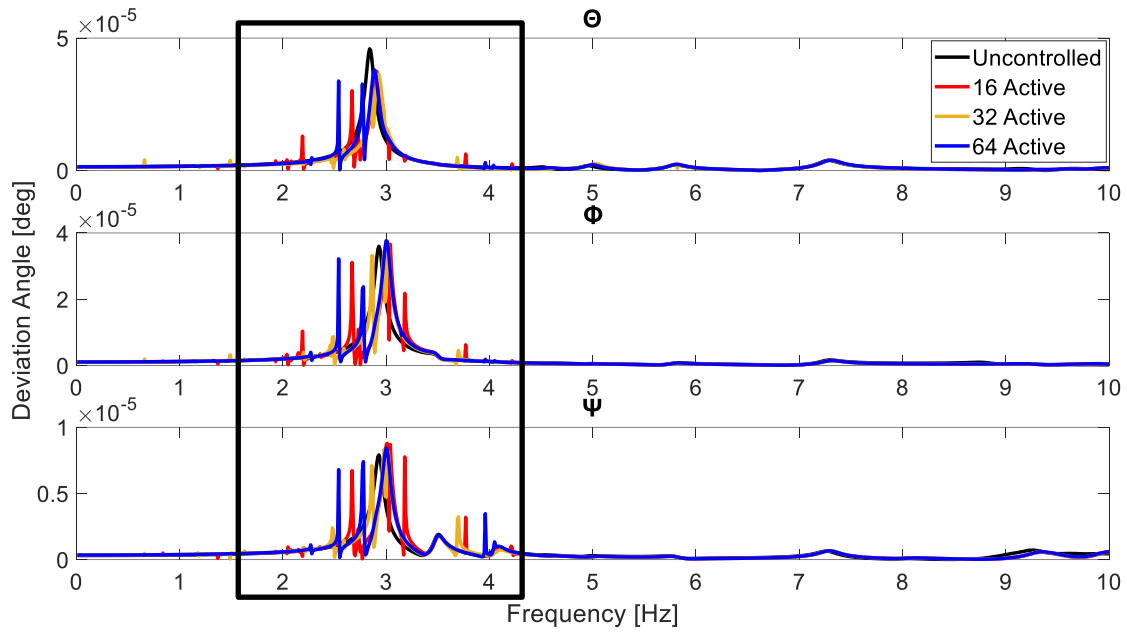


Figure 7.10 - Frequency response functions for the target node per DOF (Primary Case)

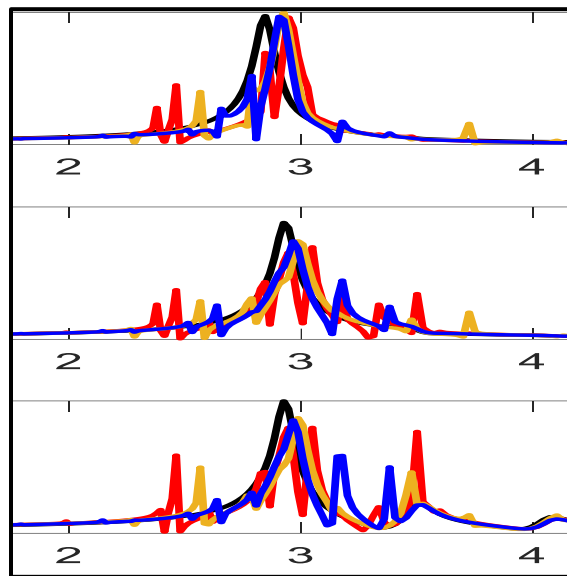
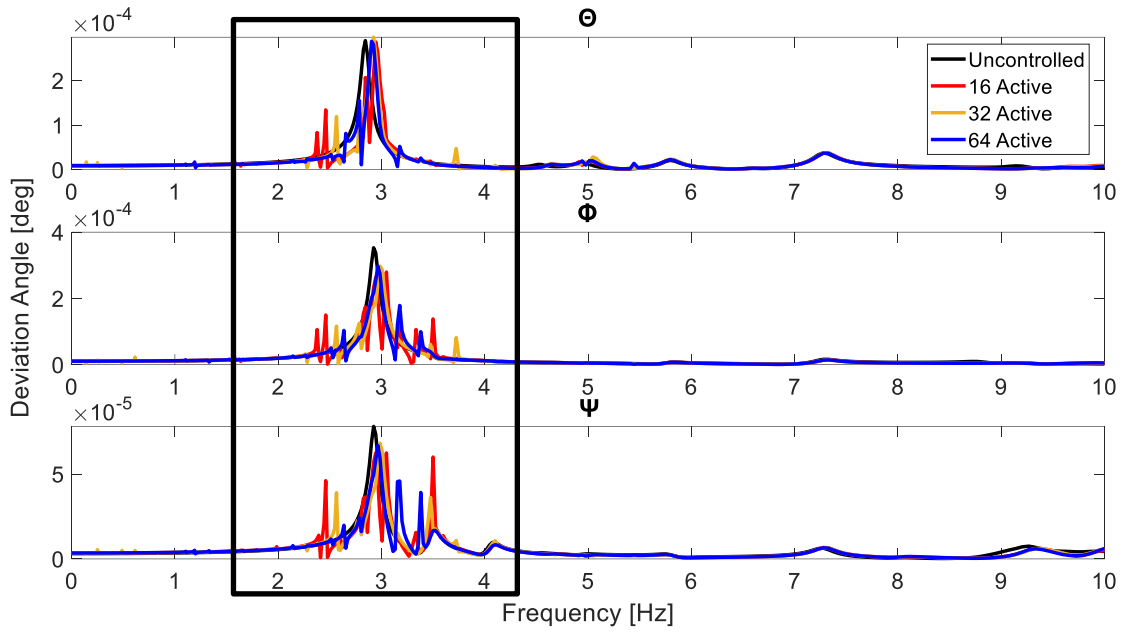


Figure 7.11 - Frequency response functions for the target node per DOF (Secondary Case)

It can be observed that each optimal configuration reduces the maximum deviation angle in all directions by forcing the structure to experience multiple less dominant resonance peaks around the original resonance peak. For the primary operating case, the maximum displacement is reduced by 20.2%, 22.1%, and 19.1% for 16, 32, and 64 active elements, respectively. Similarly, for the

secondary operating case at a higher mean wind speed the maximum displacement is reduced by 17.0%, 15.34%, and 15.0%, respectively. Additionally, calculating the root-mean square (RMS) displacement for the frequency range of 0-10 Hz yields attenuation of 23.0%, 20.7%, and 20.8% for the primary case and 18.7%, 18.7%, and 19.4% for the secondary case.

Although the configurations with more active elements still contain the smaller subset of active elements from the lesser configurations it is found that the systems with 16 active elements perform better than with 32 and subsequently 64 for reducing the maximum displacement. This is an interesting result due to its counterintuitive nature as one would expect more active elements would continually increase vibration attenuation. One possible explanation for this result is due to the nature of the proposed location metric Γ . Each optimal subcase is bound by the same constraints of maximum tensile or compressive stress in any element, which is found from the interconnectedness of the element prestresses according to the states of self-stress. Therefore, front-loading the prestresses to the active members higher up in the proposed location metric Γ , up to a certain extent, offers better attenuation within the constraints. Moreover, adding actuation length changes in elements with a lower Γ value negligibly affects the system response due to their lower influence on other elements prestress while still increasing internal stresses in themselves, possibly breaching the constraints earlier. An example distribution of active element length changes is presented in Figure 7.12 for the secondary operation case.

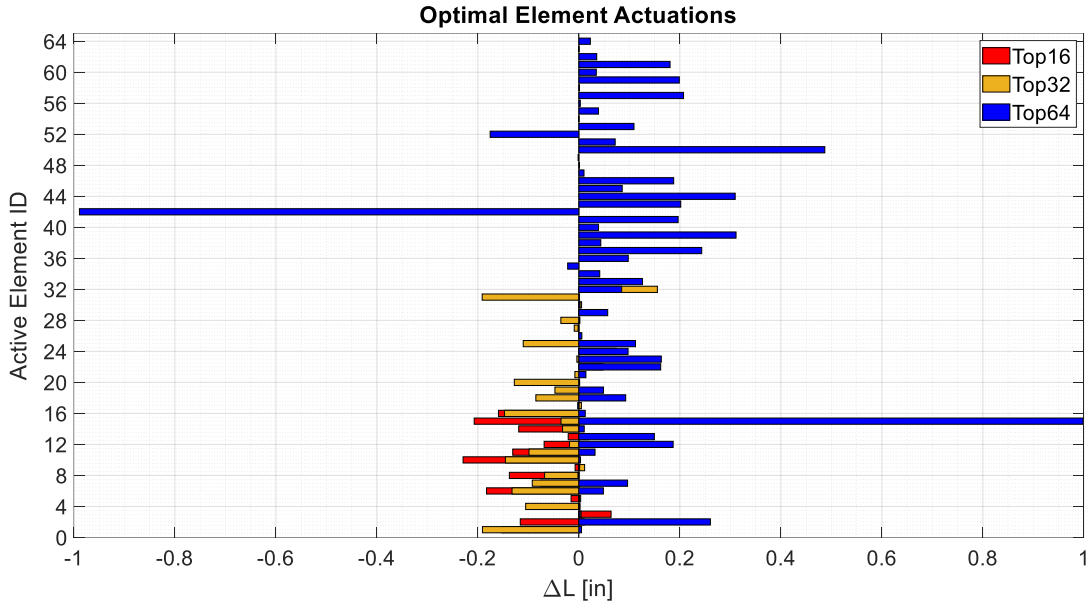


Figure 7.12 - Optimal element actuators for each actuator configuration when exposed to the secondary operating condition of the Davenport spectrum

The elemental prestresses were analyzed for each optimal design vector of actuators to determine the limiting elements in the optimization, and it was found that the active elements consistently contain much higher prestresses compared to non-active counterparts. This is the expected result as prestress produced in the active elements is only transferred to the other elements through multiplication of the shape influence matrix with factors between 0 and 1. As the constraints of this application are defined by Equation (3.9) the designer can improve attenuation by increasing the tensile yield strength, σ_{MAX} , of the active elements specifically. For example, increasing σ_{MAX} of the active elements from 70 ksi (7075-T6 aluminum) to 100 ksi (high-strength steel actuators) [104] for 16 active elements increases the attenuation from 20.2% for the primary operating case to 32.0%.

Next, both primary and secondary cases are analyzed with the OMC atmospheric disturbance model and similarly compared. The time response objective function, η , was altered to the integral of the response function with respect to time, thus ensuring the maximum overall vibration attenuation was achieved throughout the disturbance response. The total and per degree of freedom response for each subcase is presented in Figure 7.13 and Figure 7.14, respectively for the first 6 seconds of the response.

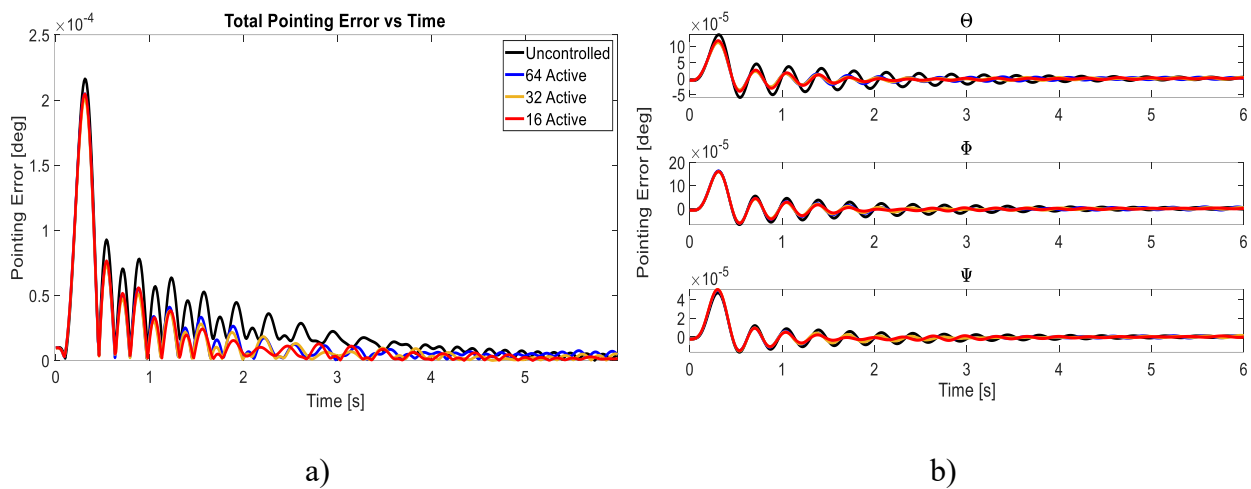


Figure 7.13 – a) Total and b) per DOF response for each subcase (OMC - Primary Case)

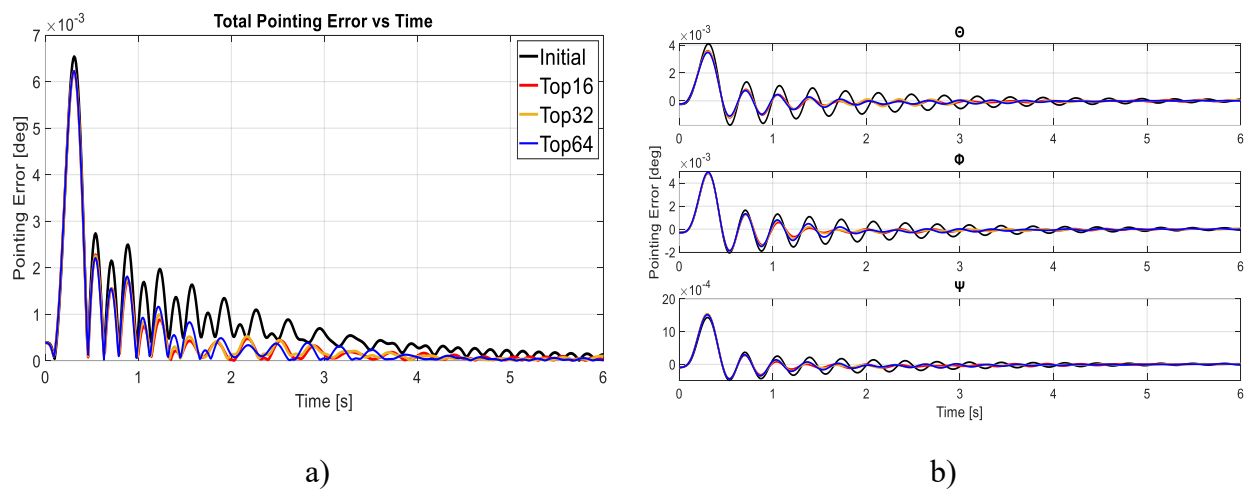


Figure 7.14 – a) Total and b) per DOF response for each subcase (OMC - Secondary Case)

A similar result as DS was found for OMC, larger available values in the fewer and more effective members giving a slightly better result. The time response is attenuated by 36.8%, 36.2%, and 34.6% for 16, 32, and 64 active elements, respectively. For the secondary operating case at a higher mean wind speed the maximum displacement is reduced by 37.0%, 36.4%, and 35.0%, respectively. While the maximum initial peak only reduces by a relatively small amount for each degree of freedom the dynamic response is seen to be heavily attenuated for each actuation subcase as the response signal dies out much quicker than the uncontrolled case. This is as a direct result of the change of objective functions for the time domain response as previously discussed, no longer is the maximum displacement the target of minimization but rather the overall response in the given timeframe. The magnitude of vibration attenuation is summarized for each DS and OMC subcase in Table 7.3.

Table 7.3 - Summary of Attenuation

Aluminum Elements, $\sigma_Y = 70 \text{ ksi}$						
<i>N</i>	Primary Operating Case			Secondary Operating Case		
	DS (Max Peak)	DS (RMS)	OMC	DS (Max Peak)	DS (RMS)	OMC
16	20.2%	23.0%	36.8%	17.0%	18.7%	37.0%
32	22.1%	20.7%	36.2%	15.4%	18.7%	36.4%
64	19.1%	20.8%	34.6%	15.0%	19.4%	35.0%

Chapter 8: Case Study II: Attenuation of the dynamic aeroelastic response of a 12-m VLBI antenna model using a multi-objective genetic optimization algorithm

The general framework was expanded from the simplified VLBI case study for the application of a high-fidelity VLBI model from InterTronic Solutions (See Figure 7.3a) with the dual objectives of minimizing the pointing path deviation angle and the total strain energy within the structure after being subjected to various atmospheric disturbances.

The strain energy, U , of a system is an elastic potential energy stored in the elements due to the external work done to elastically deform the element from its unstressed state. Assuming the force-deflection relationship is linear for axial tension or compression the elemental strain energy is calculated as follows:

$$U_k = \frac{1}{2} P_{k_{eff}} \Delta l_k \quad (8.1)$$

$$\Delta l_k = |\mathbf{TCD}_i - \mathbf{TCD}_j| \quad (8.2)$$

where $P_{k_{eff}}$ and Δl_k are the elemental force in either tension or compression and the corresponding elemental length change, respectively, for an element k with nodes i and j . As Δl_k consists of a calculation using displacements from different nodes, the time consistent displacements (TCD) must be used if in the frequency domain to ensure the proper amplitudes are being compared. The total strain energy of the system can then be calculated from the summation of the elemental strain energies and categorizes the level of strain in the system. The maximum strain energy of a material

is known as the resilience and characterizes the elastic limit of the material. Maximum strain energy theory states that failure will occur when the strain energy per unit volume due to the applied stresses in a part equals the strain energy per unit volume at the yield point in uniaxial testing. Therefore, to avoid failure due to strain energy the material must be sized properly to ensure operation below the yield point with a suitable resilience.

The high-fidelity model will again be analyzed for the primary and secondary atmospheric disturbance subcases presented in Table 7.1 and Figure 7.1 for both PSD analysis with the DS model and TDG analysis with the OMC model.

8.1 VLBI Antenna Model

The original detailed finite element model (DFEM) of the VLBI antenna contains 911,842 grid points which would be extremely computationally expensive to run NASTRAN®'s SOL146. This is compounded by the iterative nature of the MOGA optimization and therefore requires severe reduction to achieve a practical framework. Nieto successfully reduced this DFEM to a ROM with 1328 grid points while maintaining 99.9% accuracy of the total structural mass for the first 165 mode shapes [90]. Nieto chose to retain only the grid points that mimic/define the overall shape of the antenna and grid points with the highest mass participation factors. When performing normal modes analysis this leads to a root mean square error between the ROM and DFEM of only 0.0346% for the first 20 flexible modes, where error is calculated as the percent change between each respective mode. This model order reduction caused a large reduction in computational cost, reducing normal modes analysis (SOL103) from 27.3 minutes to 0.93 minutes and dynamic analysis (SOL146) from 39.21 minutes to 2.05 minutes. Although this reduction is extremely beneficial, for an example MOGA optimization with a population and generation of 100 and 30,

respectively, the total function evaluations/iterations exceed 3000, resulting in a SOL146 runtime of 112.75 hours (or 4.70 days). The Nieto-ROM was therefore desired to be further reduced to decrease total runtime of the optimization. The criteria used for this further reduction was to eliminate all grid points from the Nieto-ROM that do not pertain to the following sets:

1. Grid points used for aerodynamic DLM panel definition
2. Grid points used in splining aerodynamic grid points to structural grid points
3. Boundary condition grid points
4. Grid points that define the truss structure geometry of the boom arms in the DFEM

Doing so will reduce the model as far as possible while still maintaining all important characteristics for dynamic aeroelastic analysis. This resulted in a ROM by the author and their colleague Victor Gasparetto with only 573 grid points. The GP-ROM normal modes analysis (SOL103) then required only 10 seconds to complete while SOL146 only required 50 seconds to complete. For the same population and generations as the Nieto-ROM the total optimization runtime was further reduced from 112.75 hours to only 45.8 hours (1.91 days). This will greatly benefit the overall analysis for each subcase and increase its effectiveness as a tool in industry. Next, the modal assurance criterion was calculated to ensure proper correlation between mode shapes.

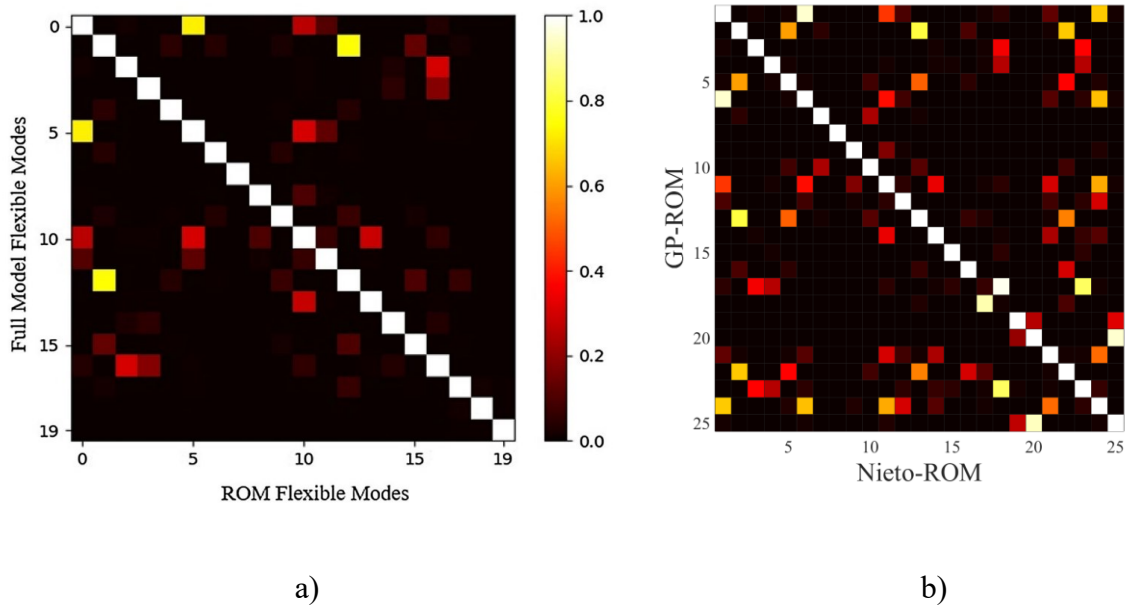


Figure 8.1 – MAC a) DFEM vs Nieto-ROM [90] b) GP-ROM vs Nieto-ROM

Figure 8.1a shows good correlation (MAC close to 1) between the DFEM and Nieto-ROM for the first 20 mode shapes while Figure 8.1b again shows good correlation but between the Nieto-ROM and the GP-ROM for the first 25 mode shapes. Figure 8.2 below illustrates the visual differences between the three models.

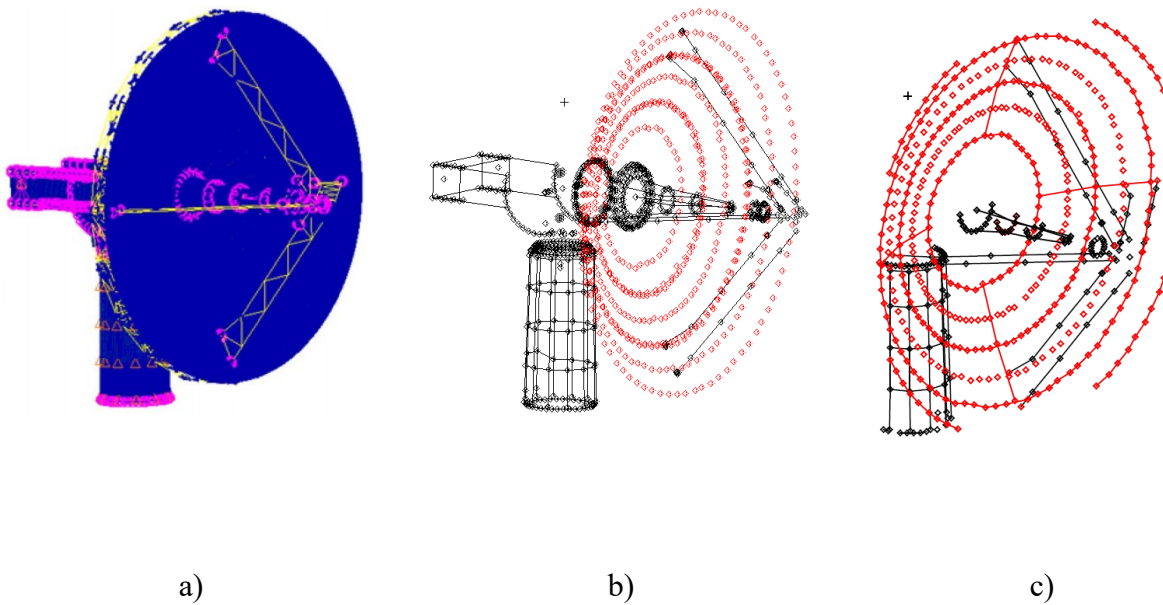


Figure 8.2 – a) DFEM b) Nieto-ROM [90] c) GP-ROM

The most important distinction between the Nieto-ROM and the GP-ROM is the boom arm subsystem of the antenna. Similar to Chapter 7:, the active element locations for this application will again be limited to the boom arm subsystem due to ease of installation and because the first few mode shapes experience large local deformation of the boom arms. As well, because the pointing error of the antenna is as a direct result of the displacements of the boom arm degrees of freedom it is important to ensure the geometric stiffness tuning capabilities are concentrated to that subsystem. A large amount of complexity is introduced in the calculation of the geometric stiffness of the entire antenna due to the interface of the parabolic dish between the boom arm truss subsystem and the supporting truss structure subsystem. This is by consequence of the theory of determinacy analysis and geometric stiffness being derived from tensegrity structures made up of purely axial bar elements. Figure 8.3 shows the clear distinction between the boom arm subsystem

and the parabolic dish. Also, the existence of the secondary reflector and collector create additional complexity for determinacy analysis similar to the primary reflector.

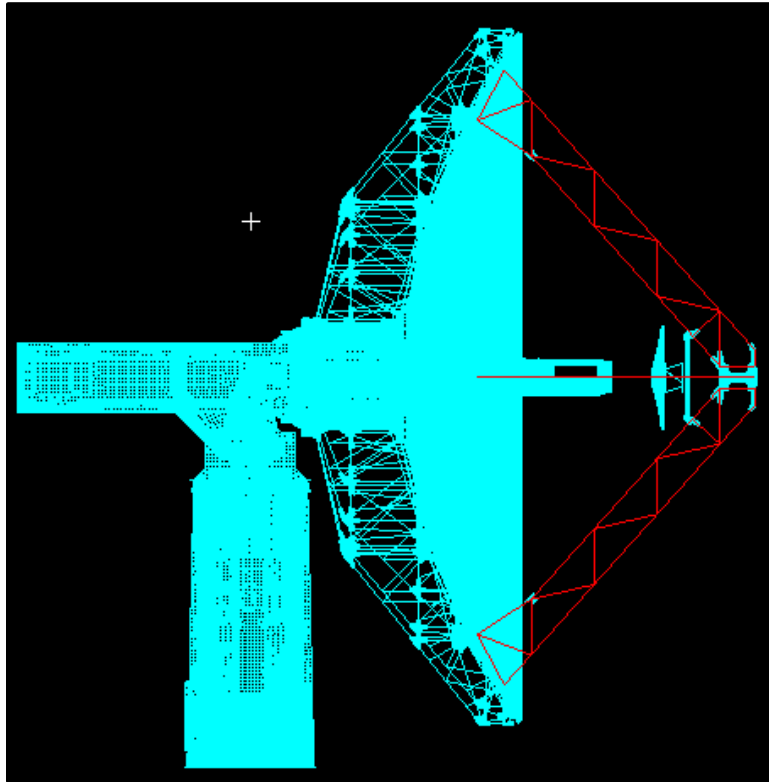


Figure 8.3 – VLBI Antenna boom arm subsystem vs remaining structure

To simplify the calculation of the geometric stiffness of the antenna, a separate geometry made of the boom arm subsystem was created to capture the effect of the active element actuations on the boom arm stiffness. This was done by joining the interface nodes between the boom arm truss structure and the antenna dish together with bar elements of high stiffness. Also, a determinacy analysis was done on the boom arm subsystem similar to the previous case study and found no states of self-stress. Therefore, off-diagonal members were again added to induce states of self-stress to allow for geometric stiffness tuning. The boom arm subsystem used for geometric stiffness calculations is shown isometrically in Figure 8.4.

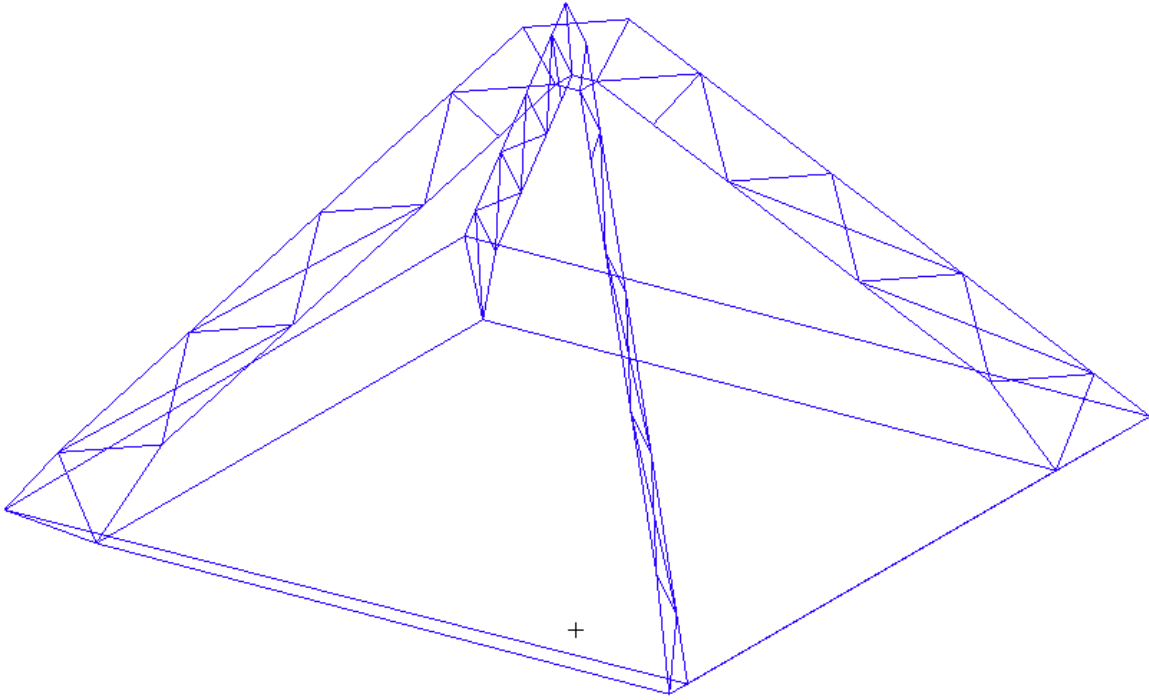


Figure 8.4 – Boom arm subsystem of GP-ROM for VLBI antenna

Next, the parameters used for the optimization of each subcase will be discussed and the corresponding results will be presented.

8.2 Parameters for Analysis of VLBI Antenna Model

The total pointing path deviation angle will again be the main objective of the optimization as the deviation angle defines the pointing accuracy of the antenna. The target node for which the deviation angles are calculated is shown in Figure 8.5 where the tangent between point 1 (target node) and point 0 (reference node) is determined for the X, Y, and Z directions corresponding to the θ , ϕ , and ψ deviation angles. The root sum squared of the three deviation angles is then computed to become the objective function value, η .

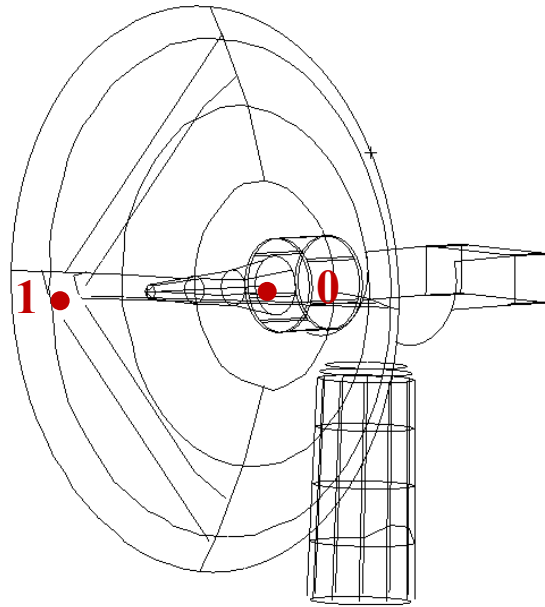


Figure 8.5 – Target and reference node definitions for VLBI antenna

The total strain energy is also computed for each element in the boom arm subsystem and summed to become the second objective function. This will serve as a direct relationship between the required actuations for improved pointing accuracy and the effect those actuations have on the structure.

Next, it is important to define the elements that will be active for each subcase, which will be determined according to Chapter 3.2 using the proposed hierarchy metric, Γ . The only elements considered in the analysis are those that correspond to existing elements in the GP-ROM, meaning all connection elements added to create the boom arm subsystem for geometric stiffness calculations are ignored as they do not pertain to actual elements in the full structure. Similar to the first case study the three actuator layout subcases that will be analyzed correspond to a structure with 16, 32, and 64 active elements. This is done again to better understand the relationship between the number of active elements, N , within Γ and the effectiveness of attenuation for a

realistic VLBI structure. Interestingly, although there are 88 potential candidates for actuators in the boom arm subsystem after analyzing Γ it was found that only 44 elements had nonzero factors towards creating prestress and subsequently affecting the geometric stiffness. Therefore, adding any additional actuators past 44 would have no benefit in geometric stiffness tuning and would only increase the total strain energy in the system. This is due to the 4 individual states of self-stress in the system combining to produce many zero rows in the force influence matrix. Analyzing the distribution of Γ resulted in the best 4 elements (elements 55, 65, 75, and 85) being superior at a value of $2.69E+05$ while all remaining elements have the same magnitude of $1.35E+05$. This is due to the high amount of symmetry in the substructure and means the difference between the active element configurations is simply the number of element candidates within the design space, where the later active elements do not lose effectiveness towards tuning. Figure 8.6 illustrates the location of elements 65 and 75 in the boom arm subsystem which have the most effect on geometric stiffness and therefore control (elements 55 and 85 are in equivalent positions in their respective arms).

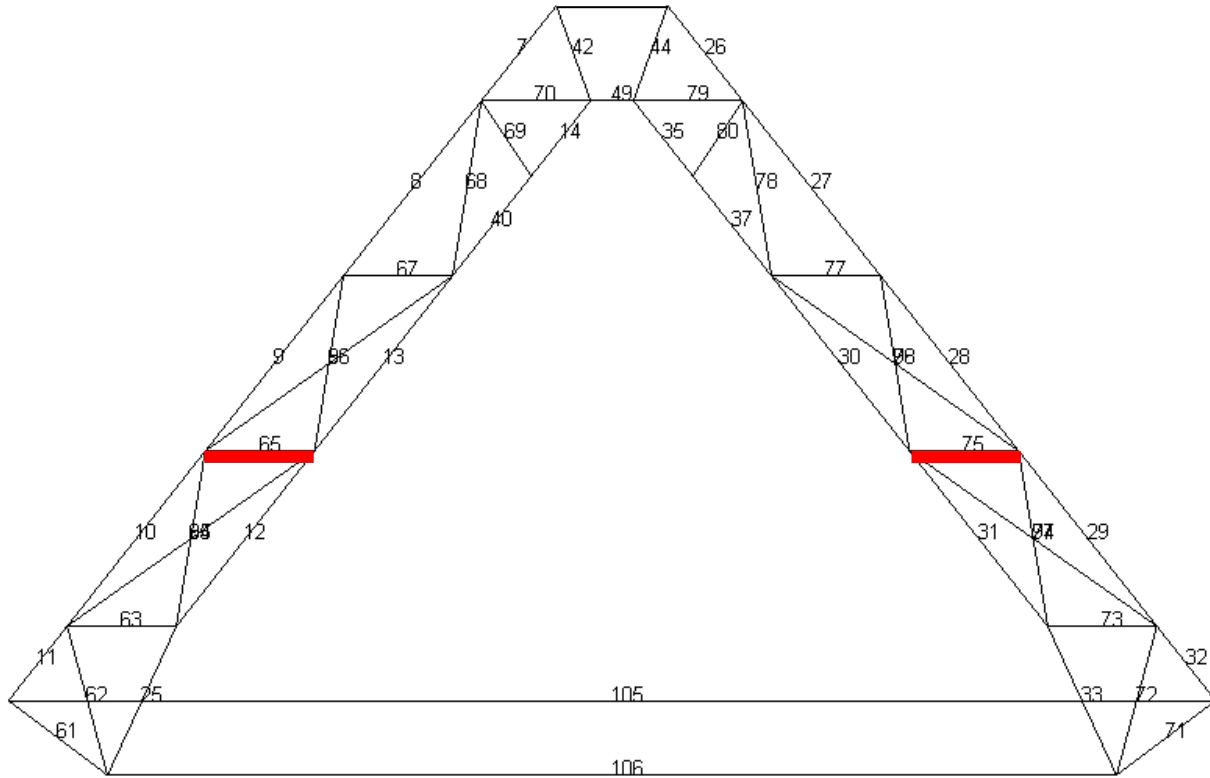


Figure 8.6 – Location of best active elements and element IDs in the boom arm subsystem

Each subcase will use either the top 16, 32, or 44 elements and for each of these subcases the same optimization parameters were used in the MOGA. The following parameters were used in each simulation and were chosen to produce results with the best improvement of the fitness function while also limiting total computation time:

- Population Size: 100
- Maximum number of generations: 15
- Crossover fraction: 80%
- Elitism probability: 2%
- Migration interval: 20%
- Pareto fraction: 35%

Specifics about the MOGA parameter definitions can be found in Deb [105] and are chosen to ensure sufficient convergence of the problem while maintaining a relatively low total function count for minimum computational cost. 1500 total function evaluations occur per actuator layout and excitation model subcase. Additionally, before presenting the results of the subcases it is crucial to establish all initial values and constraints of the problem. The constraints on the design variable (active element actuations) are defined to ensure safety of the structure at all times, accuracy of analysis, and realistic feasibility. Following the format of Equation (6.1) the constraints used for each subcase are as follows:

Fitness function: Minimize [η , TSE]

Design variables: $\Delta \mathbf{L}^*$

$$\mathbf{S}_F \Delta \mathbf{L} \leq \sigma_{MAX}$$

Constraints:

$$-\Delta \mathbf{L}_i \leq 0.05 \times length(i) \leq \Delta \mathbf{L}_i$$

where η is defined as the total point path deviation angle and TSE is the total strain energy in the system. σ_{MAX} is calculated assuming a tensile yield strength of 70 ksi [103] in the non-active members and 101.5 ksi in the active members [104].

Finally, to establish a baseline of the dynamic aeroelastic response of the VLBI antenna the initial uncontrolled response is illustrated in Figure 8.7 and Figure 8.8 for both the DS and OMC models.

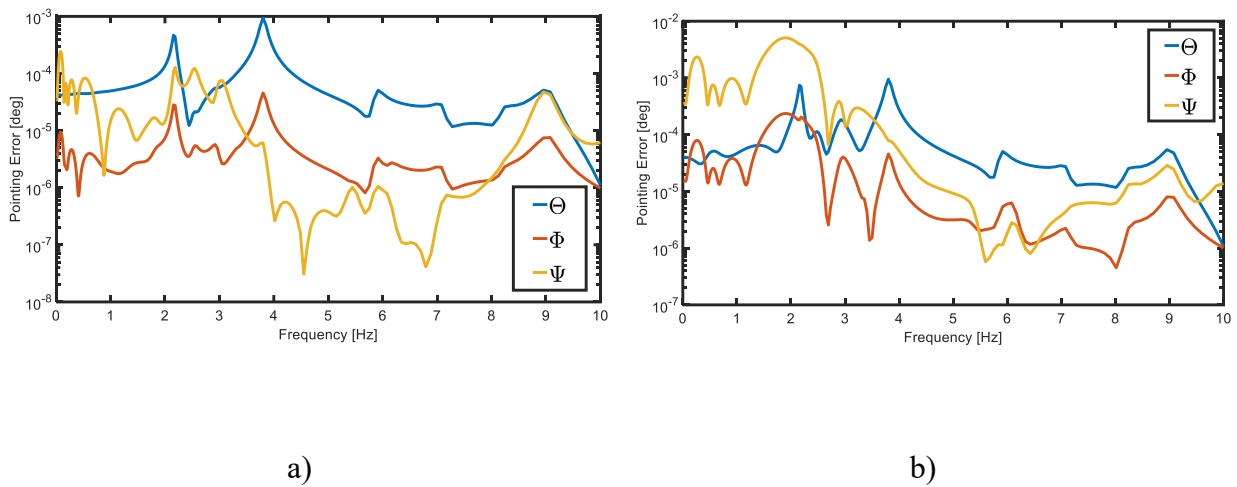


Figure 8.7 – Uncontrolled response to DS a) Primary operating case and b) Secondary operating case

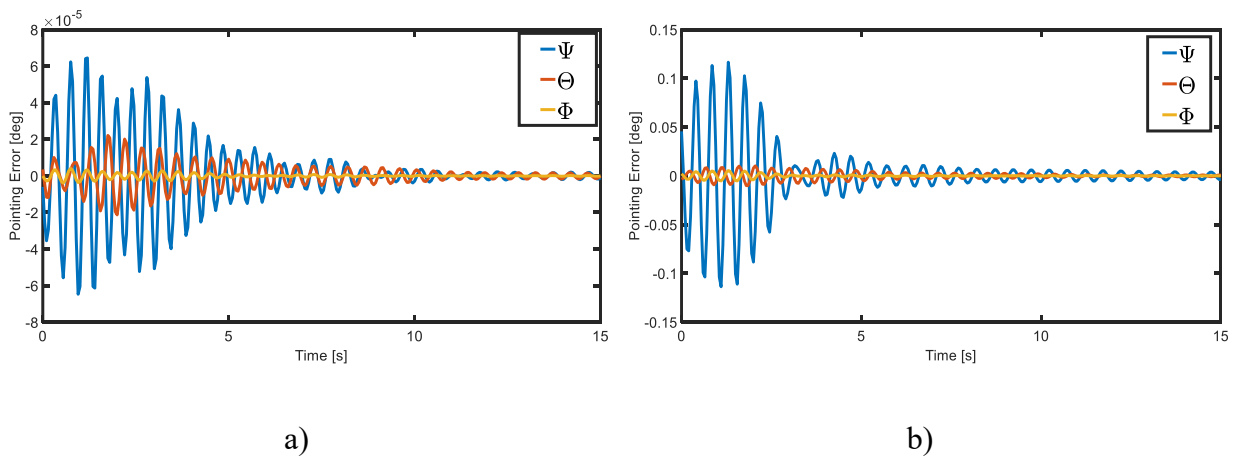


Figure 8.8 - Uncontrolled response to OMC a) Primary operating case and b) Secondary operating case

It is evident that the first two natural frequencies of the structure are at ~ 2.3 Hz and ~ 3.9 Hz which correspond to global bending modes of the structure and will be the focus areas of the optimization

algorithm as they pertain to resonance peaks similar to the findings in Chapter 7.2. An interesting factor for the secondary operating case is the dominance of the Ψ angle at lower frequencies, which may pertain to the dominant pointing error to be minimized for that load case, depending on the attenuation of that curve by means of geometric stiffening. Ψ is also dominant during the entire response in the time domain most likely due to the fact the excitation gust direction is in the z-direction.

8.3 Results for VLBI Antenna Model

First, the optimal dynamic aeroelastic response was computed with PSD analysis using the DS model's primary operating case. The total deviation angle was determined by taking the root-sum of squares of the deviation angles at the critical frequency, which is defined as the frequency pertaining to the largest deviation angle in any direction. The following pareto FRF was determined for the subcase of 16 active elements with each curve representing an optimal design along the pareto front. The original response was plotted alongside the pareto curves to illustrate specifically where the vibration attenuation occurred and can be seen in Figure 8.9 in black.

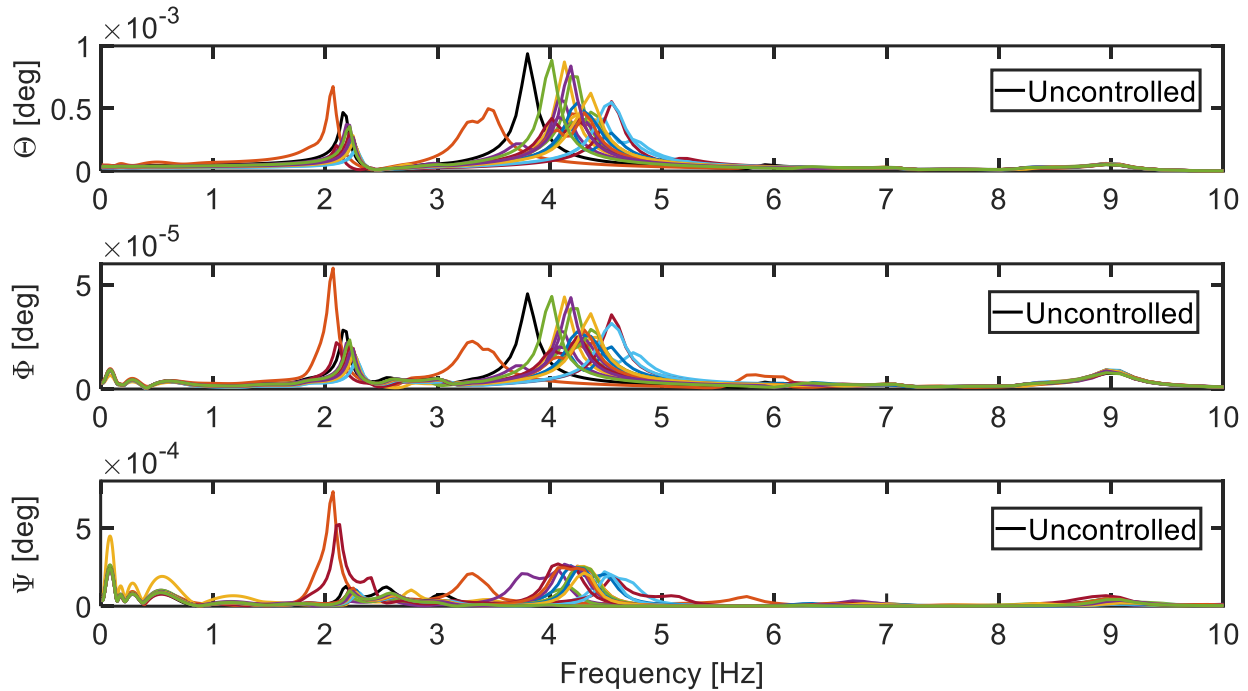


Figure 8.9 - Pointing path deviation angle frequency response of the target node in the Θ , Φ , and Ψ directions for the Davenport spectrum primary operating case with 16 active elements

As would be expected the optimal curves decreased the peak of the dominant mode in all cases for the Θ and Φ directions, however, slightly increasing in the Ψ direction. As the DS excitation direction was in the z-direction (corresponding to a deviation angle Ψ) it is expected that the magnitude of the actuation would be greatest in the Θ -direction due to its higher magnitude, leaving Ψ to slightly increase. So although the deviation angle slightly increases for Ψ it's relative magnitude is 10 times smaller than Θ , resulting in an overall decrease. It can also be seen that in general the pareto responses are shifted slightly to the right in the frequency axis. Again this is expected as the method of vibration attenuation is increasing the total stiffness by introducing a geometric stiffness. The increased stiffness will shift the natural frequencies of the structure to higher values which can be a secondary benefit of the optimization. Often the need for vibration

attenuation comes from the natural frequencies of the structure being close enough to the expected excitation frequency to activate a resonance response resulting in large amplitudes of displacement and deflection. If designed with this in mind the experienced shift from the geometric stiffness may bring the resonance frequencies of the structure far enough away from the expected mean wind speed to decrease the chance of experiencing resonance.

To determine the best individual from this pareto set of optimal values the utopian point method was employed as discussed in Chapter 5:. For the subcase of 16 active elements and using equal weights between pointing error reduction and total strain energy increase in the boom arms the best individual in the pareto front was deemed to be individual 6. Figure 8.10 shows this selection and the two objective functions ranges for the solution space. No convergence plot is shown for this MOGA framework as there is no optimal value to converge to. Instead, each individual in the pareto set corresponds to an optimal design vector with varying levels of the two objective functions.

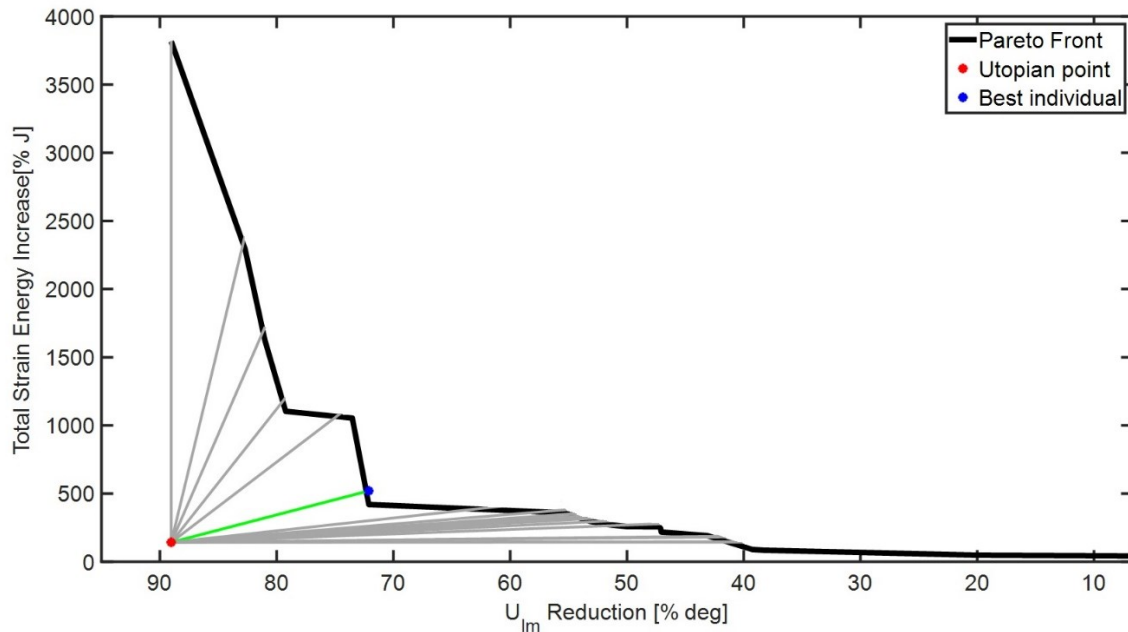
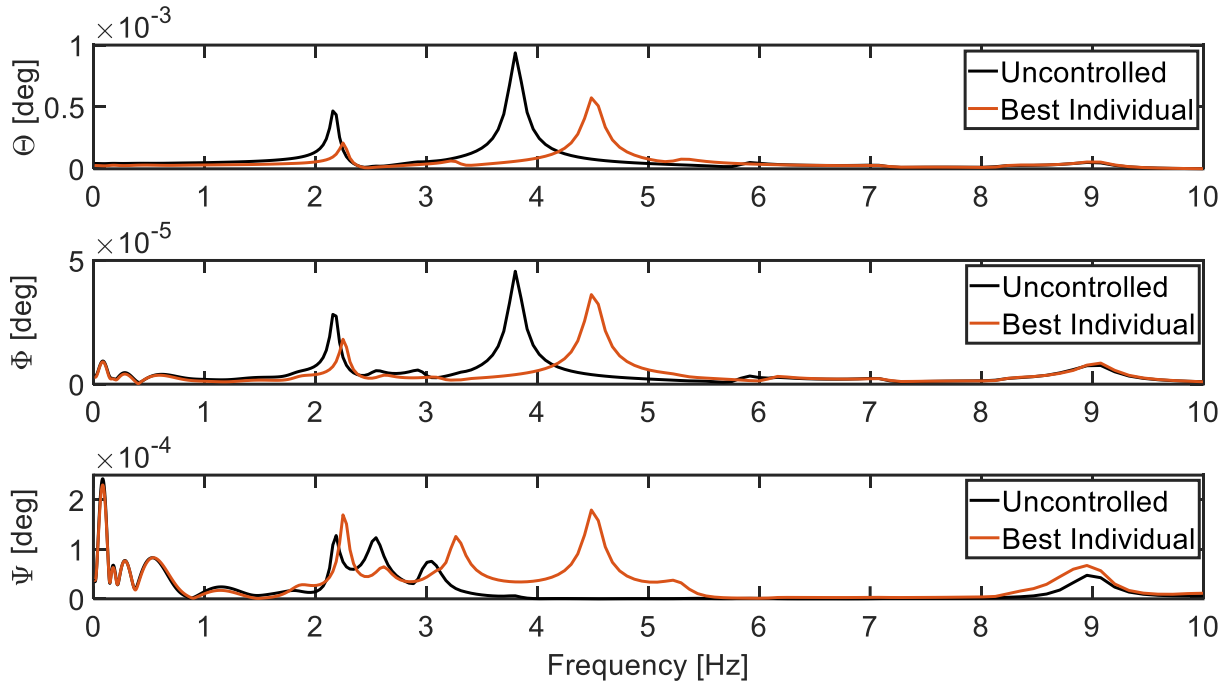


Figure 8.10 – Utopian point plot and determination of best individual for the Davenport spectrum primary operating case with 16 active elements

The level of attenuation ranges between $\sim 0\%$ and 90% for the pointing error corresponding to a strain energy increase of $\sim 0\%$ to 3750% . This exemplifies the frameworks capabilities of vibration attenuation depending on allowable levels of strain energy defined by the designer. Although the percent increase in strain energy seems extremely high the y-axis is calculated as percent change from a value of 6.8 J , meaning even the 3750% increase at 90% attenuation still only corresponds to a total strain energy of 266.4 J in the booms. Next, the best individual (corresponding to a pointing error of $6.2\text{E-}04$ degrees and 72.1% reduction) was plotted against the uncontrolled case and the FRF in Figure 8.11 was produced.



**Figure 8.11 – Uncontrolled vs. best individual response for the Davenport spectrum
primary operating case with 16 active elements**

The optimization algorithm was then run for the subcase of 16 active elements with the secondary operating condition consisting of a much higher mean wind speed. Similar to the primary operating case the Ψ direction slightly increases and is now the dominant component of the total deviation angle, however, the total deviation angle still decreases for each pareto response. The hump previously mentioned at low frequencies is amplified at secondary operating cases mean wind speed. This is believed to correspond to numerical instabilities and when analyzed in MSC Patran® a local bending mode in the boom arms is seen. The increased stiffness from the active members greatly removes this instability as can be seen by the attenuated humps in Figure 8.12.

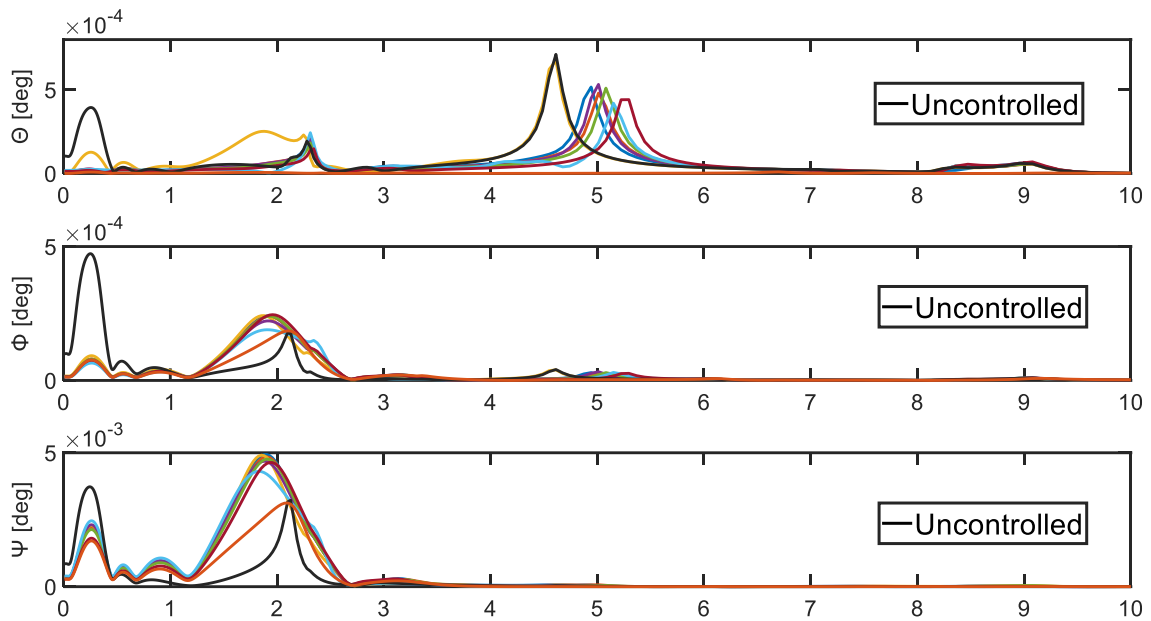


Figure 8.12 – Pointing path deviation angle frequency response of the target node in the Θ , Φ , and Ψ directions for the Davenport spectrum secondary operating case with 16 active elements

It is observed once again that the addition of the geometric stiffness shifts the natural frequencies to the right and reduces the maximum peak. To eliminate repetitive figures the utopian point plots will not be reproduced for the remaining subcases. Instead, Table 8.1 summarizes the best individuals and their corresponding total strain energy increase and pointing error for each subcase of the DS model. For all design vectors corresponding to these best individuals for PSD analysis please refer to Appendix A

Table 8.1 - Objective function values for the best individuals within each subcase of the DS frequency response analysis

PSD	Primary - 16		Primary - 32		Primary - 44	
	η [deg]	TSE [J]	η [deg]	TSE [J]	η [deg]	TSE [J]
Best Individual (Value)	6.2E-05	35.4	4.3E-05	51.7	3.9E-05	26.7
Best Individual (% change)	72.1	420.6	80.7	660.6	82.6	292.5

PSD	Secondary - 16		Secondary - 32		Secondary - 44	
	η [deg]	TSE [J]	η [deg]	TSE [J]	η [deg]	TSE [J]
Best Individual (Value)	2.7E-04	1318.5	5.4E-04	447.1	2.3E-04	2350.5
Best Individual (% change)	77.7	419.1	55.7	76.0	80.9	825.3

For the primary operating case the configuration with 44 active elements achieves the best attenuation and with the lowest total strain energy. This is an interesting result when compared to the results of the simplified antenna model where the lower active element configurations achieved better attenuation. This is believed to be due to the previously discussed nature of Γ for this geometry where the later active elements (elements 16-32 and then 32-44) do not lose effectiveness in tuning the dynamic response. In the simplified antenna the Γ vector had a decreasing nature with the later elements and it was discussed that adding those active elements would simply serve to breach the constraints of the problem before adding beneficial tuning capabilities.

Next, the framework was used to analyze the time response of the deviation angle due to the discrete OMC excitation profile for the same subcases. For the time domain responses, the objective function η was altered to calculate the total deviation angle as the sum of the integrals of the deviation angle time responses, which represents the total area under the three separate time-response curves. As previously mentioned, the subcase of 64 active members was altered to 44 due to the geometry of the boom arm subsystem. Figure 8.13 and Figure 8.14 depicts the deviation

angles Θ , Φ , Ψ and η for the uncontrolled response (black) and the pareto responses. For clarification, the pareto individuals for each subcase were individually determined using the MOGA for each subcase and excitation profile and the corresponding responses were outputted, a single set of pareto individuals was not determined for all operating cases. This is because the physical method of the framework is an adaptive control method for which the response can be controlled based on the expected excitation. This eliminates the need for a universal best individual as the designer can set the excitation profile to the forecasted mean wind speed for the following day and the algorithm can determine the required active element length changes needed to control that response. Future suggestions to improve this process are discussed in Chapter 9.

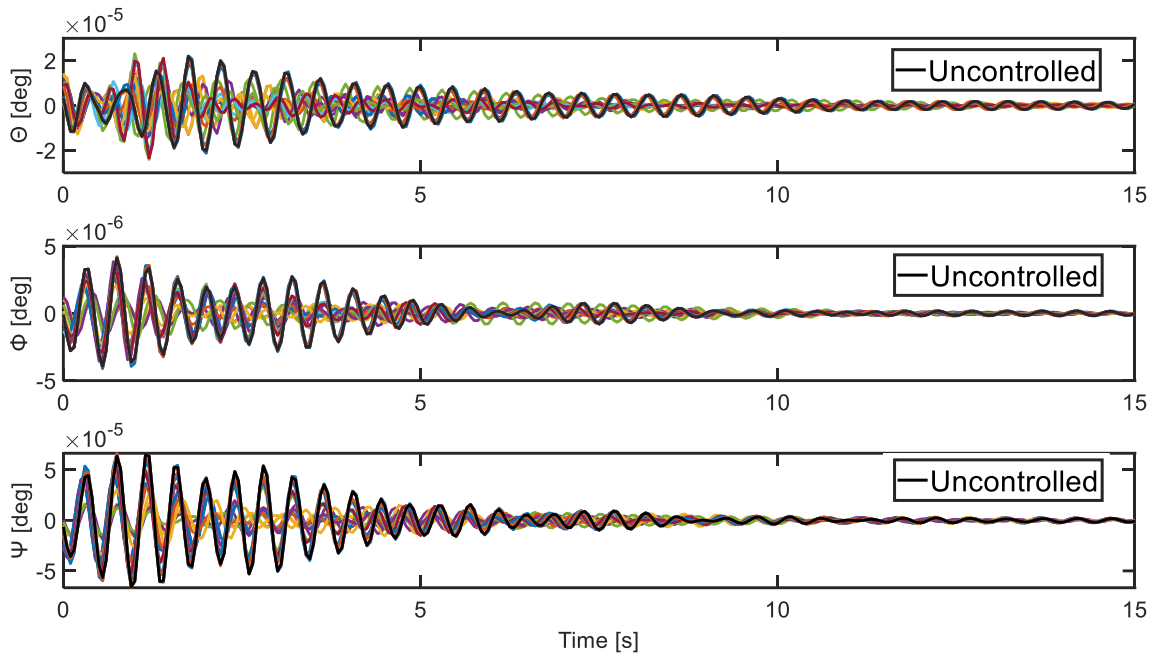


Figure 8.13 – Pointing path deviation angle frequency response of the target node in the Θ , Φ , and Ψ directions for the OMC primary operating case with 44 active elements

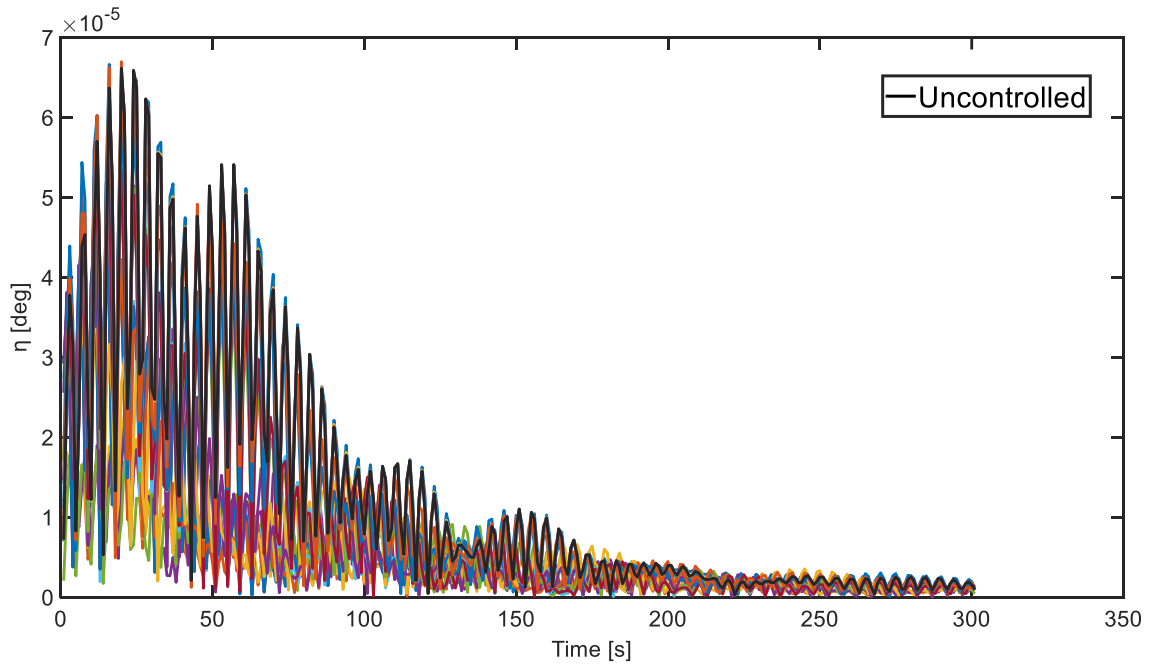


Figure 8.14 – Total pointing path deviation angle frequency response of the target node for the OMC primary operating case with 44 active elements

As opposed to the PSD analysis the deviation angles are reduced for the time response in all directions simultaneously. Due to lack of damping control with this method the initial gust response is the target for the active members, reducing the peaks as much as possible in the first ~10 seconds of the simulation. This is why Figure 8.14 shows the x-axis going to 300 seconds even though the initial response is greatly attenuated by reducing the initial maximum peaks. As with the PSD analysis the utopian point method was employed to select the best individual for each subcase. As an example, Figure 8.15 plots the control ranges and selection of the best individual for the primary operating condition with 44 active elements, selecting individual 9 within the pareto set. This best individual's time response is then plotted against the uncontrolled response in Figure 8.16.

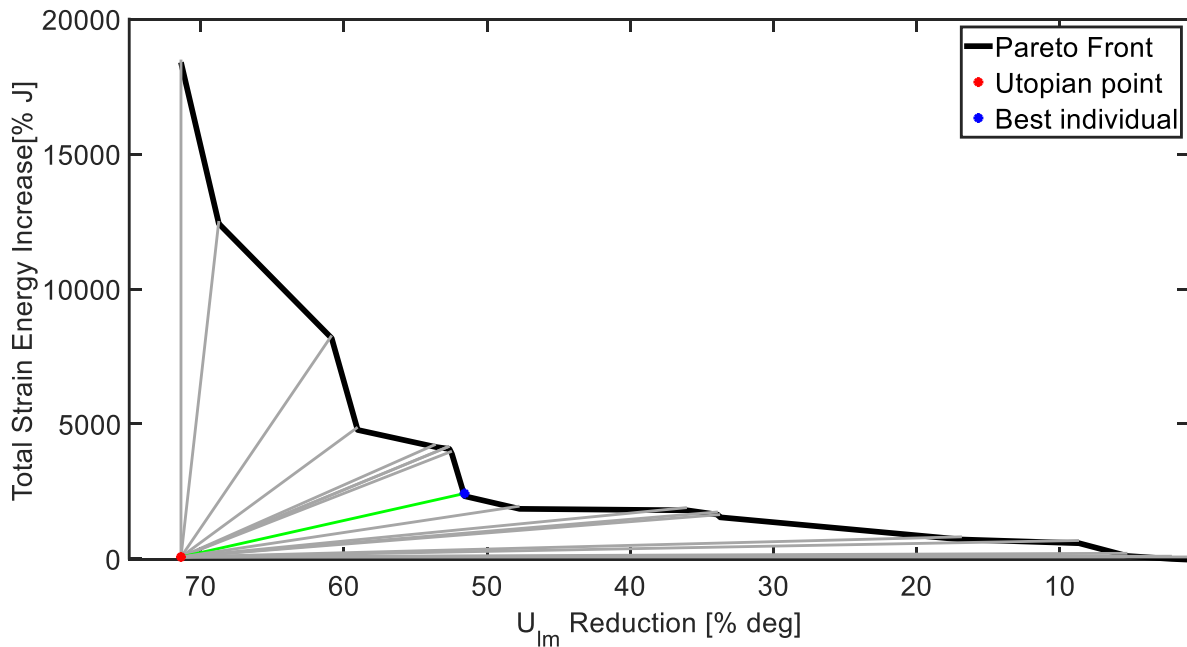


Figure 8.15 – Utopian point plot and determination of best individual for the OMC primary operating case with 44 active elements

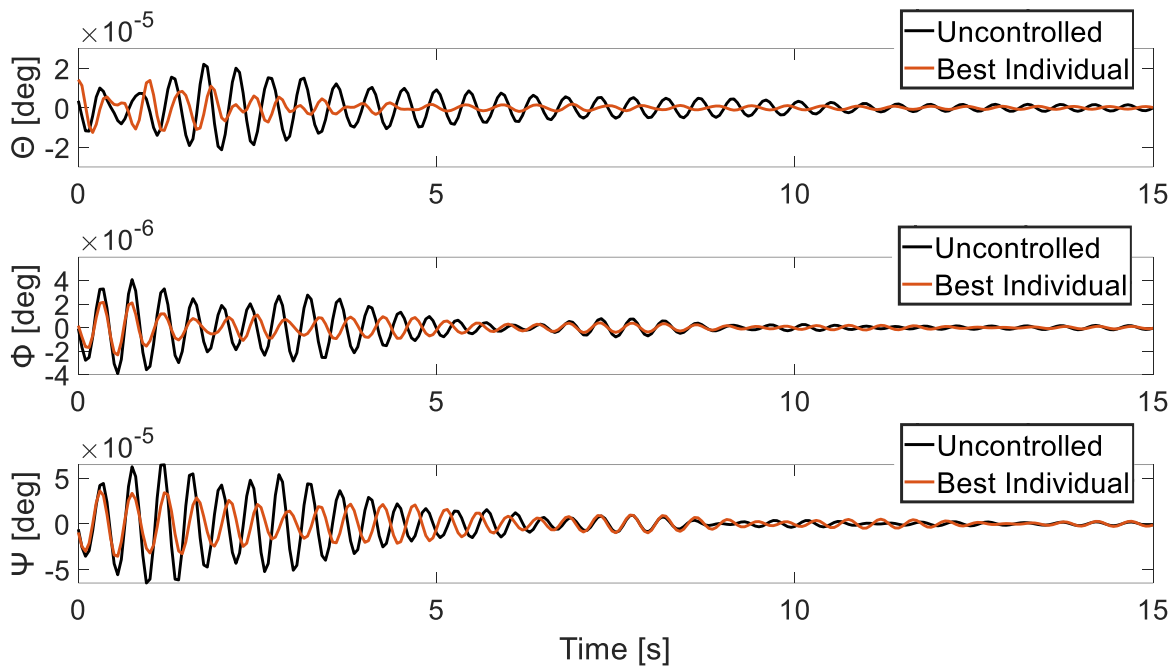


Figure 8.16 – Uncontrolled vs. best individual response for the Davenport spectrum primary operating case with 44 active elements

As previously mentioned, the time response is attenuated for all three directions simultaneously. The active members render the Θ deviation angle negligible within ~ 5 seconds compared to the uncontrolled response requiring ~ 10 seconds to achieve the same level. This is however not reproduced for the Φ and Ψ angles although they are greatly reduced throughout the timespan. This is possibly due again to the fact that the excitation profile direction is in the z-direction for the DLM panels, allowing the greatest difference to be seen in the x-direction for uncontrolled vs controlled as it is simply resisting bending in that direction instead of the brunt of the gust.

Finally, the framework was tested for the three active element subcases using the OMC secondary operating case and the pareto responses are plotted against the uncontrolled response in Figure 8.17 and Figure 8.18 where again the uncontrolled response is displayed in black.

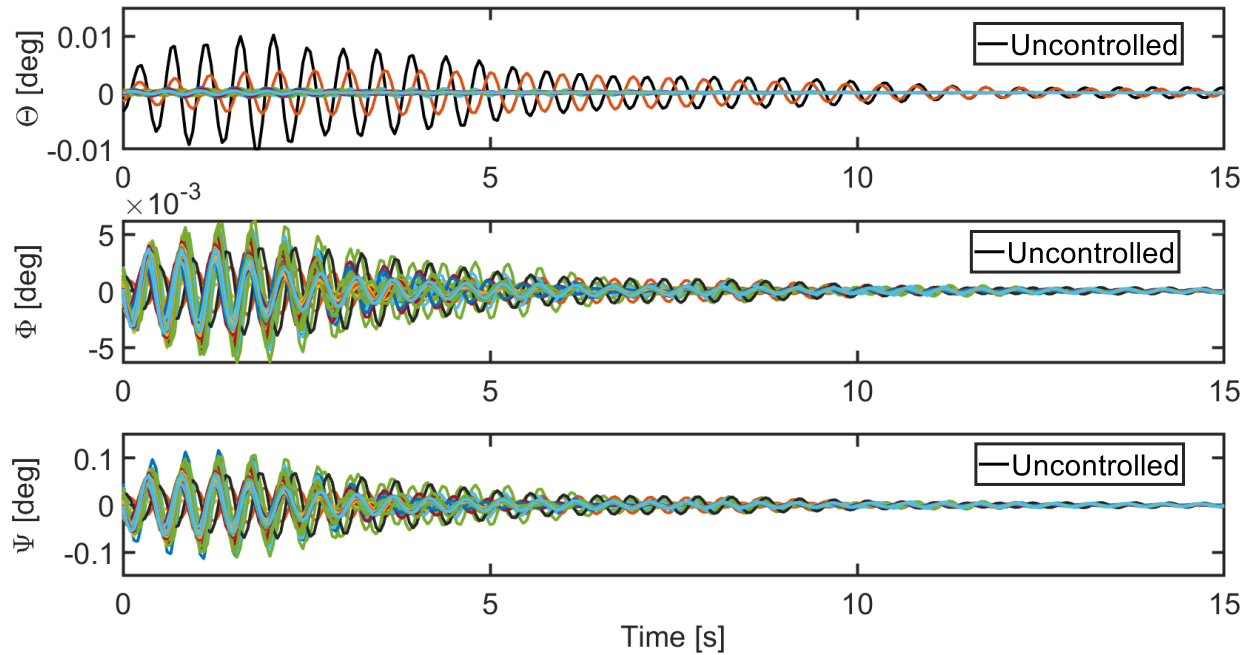


Figure 8.17 - Pointing path deviation angle frequency response of the target node in the Θ , Φ , and Ψ directions for the OMC secondary operating case with 44 active elements

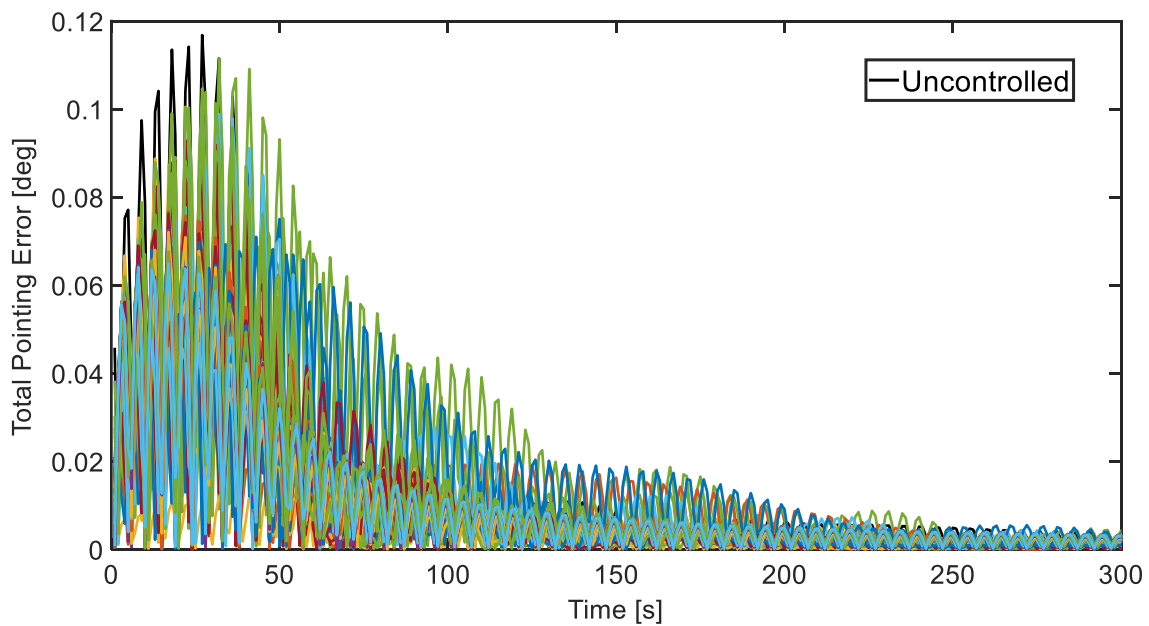


Figure 8.18 - Total pointing path deviation angle frequency response of the target node for the OMC secondary operating case with 44 active elements

A similar result is seen for the secondary operating case as in the primary. Each individual deviation angle being attenuated but with the greatest reduction by far experienced by Θ , this effect only being amplified by the increased mean wind speed of the OMC. The remaining OMC subcases are summarized to avoid redundancy and can be seen in Table 8.2. For all design vectors corresponding to these best individuals for TDG analysis please refer to Appendix A

Table 8.2 – Objective function values for the best individuals within each subcase of the OMC time response analysis

TDG	Primary - 16		Primary - 32		Primary - 44	
	η [deg]	TSE [J]	η [deg]	TSE [J]	η [deg]	TSE [J]
Best Individual (Value)	2.1E-05	1.3	2.0E-05	1.8	2.3E-05	1.4
Best Individual (% change)	54.9	1977.0	58.5	2741.9	51.6	2098.1

TDG	Secondary - 16		Secondary - 32		Secondary - 44	
	η [deg]	TSE [J]	η [deg]	TSE [J]	η [deg]	TSE [J]
Best Individual (Value)	1.9E-02	10565.6	2.8E-02	20522.3	1.1E-02	14868.6
Best Individual (% change)	66.0	5.7	51.9	105.2	80.5	48.7

Interestingly, for the primary operating case the best individual with the 32 active element configuration achieves the best attenuation in the dynamic response. This is counter to the DS result and OMC secondary case where the most active elements results in the best attenuation. As can be seen in Table 8.2 this subcase results in a lower total strain energy than with 32 active elements so this worse attenuation is perhaps due to the slope of the pareto front for the 44 active element primary operating subcase and the subsequent selection of the best individual. For the secondary operating case the total strain energies are extremely high compared to the primary case due to the increased mean wind speed, however percent increases are much lower compared to the primary case due to the larger initial strain energy value. It is up to the designer if these levels of

strain energy are acceptable for implementation and, if not, different weights can be assigned in the selection of the best individual from the pareto front to lower these strain energy levels. Again, it is important to note that the constraints of the problem prevent any element from reaching its yield strength and causing failure. In all cases, both DS and OMC, the framework achieves great levels of dynamic response attenuation with varying increases in total strain energy.

Chapter 9: Conclusion and Further Work

This thesis proposed an optimization framework that leverages the principles of tensegrity structures by using geometric nonlinearities to adaptively tune the dynamic aeroelastic response of aerospace structures. The framework pairs the theories of geometric nonlinearities with dynamic aeroelasticity analysis and implements them in the design space of both a single and multi-objective genetic optimization algorithm. To achieve this, a detailed MATLAB® program was written to perform determinacy analysis, identify optimal locations for active elements based on a new proposed hierarchy metric by the author, and calculate the objective functions of the problem defined by the dynamic aeroelastic response. To obtain the dynamic response the algorithm iteratively calls MSC NASTRAN®'s SOL146 using the DLM method for varying levels of prestress in the active members (through actuator length changes) and uses time consistent output equations in MATLAB® to calculate the objective functions. This is done in the design space of a multi-objective genetic optimization algorithm where the utopian point method is used to determine a pareto set and its corresponding best individual. For each simulation, the effect of the applied load was considered in the active element prestresses which were constrained according to tensile yield strengths and max allowable nodal displacements.

Two case studies were presented to showcase the effectiveness of the proposed framework. First, a simplified Earth-based antenna model was created and analyzed for both a primary and secondary operating case using both PSD analysis in the frequency domain with the DS disturbance model and TDG analysis in the time domain with the OMC disturbance model. FRF's and TRF's were analyzed using 3 different active element configurations of the best 16, 32, and 64 elements as defined by the hierarchy metric Γ . The optimization algorithm successfully attenuated the peak

pointing error by 22.1% and 17.0% as well as the RMS pointing error by 23.0% and 18.7% for the DS primary and secondary operating cases, respectively. For the TDG primary and secondary operating cases the response was attenuated by 36.8% and 37.0%, respectively. It was found that the limiting factors were the prestress in the active elements and when the aluminum actuators were replaced with high strength steel counterparts the total pointing error reduction increased from 22.1% to 32.0%.

The second case study consisted of the application of a high-fidelity VLBI antenna model from Intertronic Solutions. The HF model was greatly reduced using the CBMOR method to drastically decrease the computation time from 39.21 minutes to only 50 seconds while maintaining a 99.9% MAC correlation in the first 20 modes. With the reduced model the framework used a multi-objective genetic optimization algorithm with the dual objectives of decreasing total pointing error while minimizing the total strain energy in the system as a result of both the applied load and applied actuations. Pareto sets containing optimal responses for each subcase of 16, 32, and 44 active members were obtained and the utopian point method was used to calculate their best individual. For the PSD analysis under DS excitation the algorithm decreased the total pointing error by 82.6% with a total strain energy increase of 292.5% for the primary operating case. At the increased mean wind speeds of the secondary operating case the algorithm was still able to reduce the total pointing error by 80.9% but with a total strain energy increase of 825.3%. Similarly, for TDG analysis with the OMC excitation profile the algorithm reduced the total pointing error by 54.9% with a TSE increase of 1977.0% and 80.5% with a TSE increase of 48.7% for the primary and secondary operating conditions, respectively when compared to their uncontrolled state.

9.1 Recommendations for Future Work

This framework is useful for applications where indeterminate structures can be implemented and the effects of environmental loading must be considered. However, a few considerations must be taken for the implementation of the proposed framework and lead to the following recommendations for future work:

1. The effect of the proposed hierarchy metric for determining optimal active element locations in a simplified manner should be further analyzed to determine its effectiveness in other applications. A full factorial analysis is recommended to better understand this trend but was outside of the scope of this work due to the computational cost.
2. One of the main benefits of this framework is that it is an adaptive control method, meaning a single optimal design vector is not required for various load cases as the system can adapt to the expected load and adjust the necessary actuation lengths accordingly. However, due to the complexity of the calculations performed in dynamic aeroelastic analysis the computational cost of implementing this analysis in the design space of an optimization algorithm is extremely high even with extreme reduction in the FEM. Methods to further reduce this computational cost should be explored to increase the effectiveness of the framework in real-world applications. Once this is done, testing the effectiveness of various control schemes will allow the system to be fully active by sensing the loading scenario with sensors and responding via control actuations.
3. Perform a sensitivity analysis to determine the performance when the actual dynamic loading is different than the expected loading used to find the optimal design variables.
4. Finally, experimentally implementing this framework to further validate its effectiveness would be crucial to determining possible applications.

Appendices

Appendix A

The following tables give the design vectors of the best individuals for each subcase. Each vector represents an actuation length change in inches of the respective active element to induce prestress in the member and tune the geometric stiffness matrix for vibration attenuation. As the proposed framework is adaptive in nature a separate design vector is found for each specific subcase to ensure the best individual is tailored specifically to that subcase to achieve the best result.

<i>Element ID</i>	PSD Analysis with Davenport Spectrum					
	Primary			Secondary		
	16	32	44	16	32	44
85	0.034	-0.139	-0.269	-0.059	-0.075	-0.079
55	0.015	0.002	-0.135	-0.010	0.001	-0.130
65	0.270	-0.134	-0.135	-0.604	-0.235	-0.137
75	-0.021	0.003	-0.135	-0.042	0.013	-0.042
2	0.290	0.084	0.049	0.130	-0.020	0.090
5	0.349	0.085	0.049	0.174	0.050	0.048
57	0.827	0.222	0.280	0.832	1.219	0.297
56	1.786	0.575	0.719	1.607	0.623	0.722
94	0.301	-0.096	-0.477	-0.668	-0.141	-0.479
10	0.730	0.041	-0.086	0.263	0.030	0.041
12	0.317	0.034	0.049	0.301	0.035	0.050
63	0.944	0.211	0.280	0.090	0.099	0.279
64	1.556	0.605	0.585	1.365	0.606	0.715
95	0.786	-0.220	-0.477	-0.450	-0.446	-0.480
9	-0.357	0.036	-0.086	0.288	-0.059	0.057
13	0.424	0.036	-0.454	0.296	0.113	0.040
67		0.229	0.280		0.200	0.310
66		0.620	0.585		0.623	0.729
96		-0.444	-0.244		-0.432	-0.259
18		0.119	-0.086		0.117	0.046
21		0.097	-0.086		0.044	0.082
87		0.236	0.280		0.265	0.295

86		0.481	0.953		0.506	0.789
92		-0.117	-0.477		-0.121	-0.770
28		0.018	0.416		-0.036	0.051
30		0.092	0.282		1.042	0.012
77		0.207	0.415		0.230	-0.330
76		0.491	1.087		0.585	0.715
98		-0.100	-0.109		-0.106	-0.478
19		0.109	0.049		0.074	-0.129
22		0.160	-0.086		-0.018	0.119
83		-0.086	0.648		-0.190	0.283
84			1.087			0.747
91			-0.244			-0.485
29			0.282			0.219
31			0.049			0.057
73			0.280			0.280
74			0.719			0.452
97			-0.244			0.142
3			-0.086			0.854
4			0.282			0.058
53			0.514			0.350
54			0.585			0.784
93			-0.244			-0.467

TDG Analysis with One-Minus Cosine						
	Primary			Secondary		
<i>Element ID</i>	16	32	44	16	32	44
85	-0.006	-0.129	-0.140	-0.225	-0.132	-1.228
55	0.003	0.018	-0.135	0.017	0.000	-0.135
65	-0.582	-0.134	-0.135	-0.121	-0.133	-0.135
75	0.013	0.001	-0.135	0.175	0.021	-0.135
2	-0.146	2.008	0.048	0.352	0.084	0.049
5	0.172	0.097	-0.242	0.620	0.084	0.049
57	1.162	0.227	1.242	1.062	0.232	0.280
56	1.333	0.460	0.717	1.805	0.936	0.719
94	-0.822	0.930	-0.477	-0.181	-0.100	-0.477
10	0.039	0.024	0.044	0.304	0.036	0.049
12	0.333	0.131	0.054	0.558	0.036	-1.044
63	0.924	0.218	0.280	1.135	-0.272	0.280
64	1.213	0.661	0.719	1.883	0.606	0.719
95	-0.522	-0.441	-0.478	0.019	-0.442	-1.570
9	0.311	-0.316	0.049	0.293	-0.536	0.049
13	0.299	0.040	0.048	0.541	0.036	0.049
67		0.631	0.281		0.228	-0.812
66		0.609	0.724		0.606	0.719
96		-0.447	-0.522		-0.417	-0.477
18		0.584	0.034		0.117	0.049
21		0.100	0.049		0.220	0.049
87		0.231	0.280		0.238	0.280
86		0.470	0.720		-0.146	-0.374
92		0.421	-0.478		-0.098	-0.477
28		0.083	0.048		0.084	0.049
30		0.741	0.066		0.084	0.049
77		0.238	0.285		0.232	0.280
76		0.496	0.719		0.750	0.719
98		-0.099	-0.477		-0.296	-0.477
19		0.162	0.049		0.252	1.141
22		0.153	0.084		0.153	0.049
83		-0.163	0.277		-0.174	0.280
84			0.719			0.719
91			-0.478			-0.477

29			0.047			0.049
31			0.048			0.049
73			0.279			0.280
74			0.719			0.719
97			-0.477			-0.477
3			0.048			0.049
4			0.050			0.049
53			0.280			0.280
54			0.719			-0.374
93			-0.477			-0.477

References

- [1] H. v. de Figueiredo, D.F. Castillo-Zúñiga, N.C. Costa, O. Saotome, R.G.A. da Silva, Aeroelastic Vibration Measurement Based on Laser and Computer Vision Technique, *Experimental Techniques*. 45 (2021) 95–107. <https://doi.org/10.1007/s40799-020-00399-0>.
- [2] M. Arena, A. Chiariello, M. Castaldo, L. di Palma, Vibration response aspects of a main landing gear composite door designed for high-speed rotorcraft, *Aerospace*. 8 (2021) 1–19. <https://doi.org/10.3390/aerospace8020052>.
- [3] S.I. Moon, I.J. Cho, D. Yoon, Fatigue life evaluation of mechanical components using vibration fatigue analysis technique, *Journal of Mechanical Science and Technology*. 25 (2011) 631–637. <https://doi.org/10.1007/s12206-011-0124-6>.
- [4] F. Kihm, A. Langelier, K. Munson, Influence of the modal damping on the estimated fatigue life, *Procedia Engineering*. 213 (2018) 270–281. <https://doi.org/10.1016/j.proeng.2018.02.028>.
- [5] J.D. Newton, Excitation of Structural Resonance Due to a Bearing Failure, (2007).
- [6] M.G. Nieto, P. v. Thomas, M.S.A. ElSayed, M. Saad, G.L. Brown, L.M. Hilliard, Development of Efficient Dynamic Aeroelasticity Model for High Fidelity Pointing Accuracy Assessment of VLBI Earth-Based Radio Antennas, *International Journal of Aeronautical and Space Sciences*. 21 (2020) 693–706. <https://doi.org/10.1007/s42405-019-00238-6>.

- [7] J. Zhang, J. Huang, W. Liang, Y. Zhang, Q. Xu, L. Yi, C. Wang, A Correction Method of Estimating the Pointing Error for Reflector Antenna, *Shock and Vibration*. 2018 (2018). <https://doi.org/10.1155/2018/3262869>.
- [8] A.J. Keane, A.P. Bright, Passive vibration control via unusual geometries: Experiments on model aerospace structures, *Journal of Sound and Vibration*. 190 (1996) 713–719. <https://doi.org/10.1006/jsvi.1996.0086>.
- [9] A. Rittweger, J. Albus, E. Hornung, H. Öry, P. Mourey, Passive damping devices for aerospace structures, *Acta Astronautica*. 50 (2002) 597–608. [https://doi.org/10.1016/S0094-5765\(01\)00220-X](https://doi.org/10.1016/S0094-5765(01)00220-X).
- [10] S.A. Motahari, M. Ghassemieh, S.A. Abolmaali, Implementation of shape memory alloy dampers for passive control of structures subjected to seismic excitations, *Journal of Constructional Steel Research*. 63 (2007) 1570–1579. <https://doi.org/10.1016/j.jcsr.2007.02.001>.
- [11] W.A. Shen, S. Zhu, Y.L. Xu, An experimental study on self-powered vibration control and monitoring system using electromagnetic TMD and wireless sensors, *Sensors and Actuators, A: Physical*. 180 (2012) 166–176. <https://doi.org/10.1016/j.sna.2012.04.011>.
- [12] S. Nima Mahmoodi, M. Ahmadian, Modified acceleration feedback for active vibration control of aerospace structures, *Smart Materials and Structures*. 19 (2010) 065015. <https://doi.org/10.1088/0964-1726/19/6/065015>.
- [13] N.R. Fisco, H. Adeli, Smart structures: Part I - Active and semi-active control, *Scientia Iranica*. 18 (2011) 275–284. <https://doi.org/10.1016/j.scient.2011.05.034>.

- [14] Mark.J. Balas, Active control of persistent disturbances in large precision aerospace structures, in: *Advances in Optimal Structure Systems*, 1990. <https://doi.org/10.1117/12.21519>.
- [15] D.C. Hyland, J.L. Junkins, R.W. Longman, Active control technology for large space structures, *Journal of Guidance, Control, and Dynamics*. 16 (1993). <https://doi.org/10.2514/3.21087>.
- [16] H. Baier, L. Dastashvili, Active and Morphing Aerospace Structures-A Synthesis between Advanced Materials, Structures and Mechanisms, *International Journal of Aeronautical and Space Sciences*. 12 (2011) 225–240. <https://doi.org/10.5139/IJASS.2011.12.3.225>.
- [17] S. Nima Mahmoodi, M.R. Aagaah, M. Admadian, Active vibration control of aerospace structures using a modified Positive Position Feedback method, in: *2009 American Control Conference, IEEE*, 2009. <https://doi.org/10.1109/ACC.2009.5159955>.
- [18] C. Graciano, *Tensegrity Structures a State-of-the- Art Review*, (2016).
- [19] K. Yildiz, CABLE ACTUATED TENSEGRITY STRUCTURES FOR DEPLOYABLE SPACE BOOMS WITH ENHANCED STIFFNESS, *The Pennsylvania State University The Graduate School College of Engineering*. 5 (2018) 86–96. <https://doi.org/10.1016/j.ijmachtools.2009.09.004>.
- [20] W. Gilewski, J. Kłosowska, P. Obara, Applications of tensegrity structures in civil engineering, *Procedia Engineering*. 111 (2015) 242–248. <https://doi.org/10.1016/j.proeng.2015.07.084>.

- [21] P. Obara, J. Kłosowska, W. Gilewski, Truth and myths about 2d tensegrity trusses, *Applied Sciences (Switzerland)*. 9 (2019). <https://doi.org/10.3390/app9010179>.
- [22] J. Kłosowska, P. Obara, W. Gilewski, Self-stress control of real civil engineering tensegrity structures, *AIP Conference Proceedings*. 1922 (2018). <https://doi.org/10.1063/1.5019157>.
- [23] S. Pellegrino, C.R. Calladine, MATRIX ANALYSIS OF STATICALLY AND KINEMATICALLY INDETERMINATE FRAMEWORKS, *Physical Review Letters*. 99 (1986). <https://doi.org/10.1103/PhysRevLett.99.225701>.
- [24] S. Pellegrino, Structural computations with the singular value decomposition of the equilibrium matrix, *International Journal of Solids and Structures*. 30 (1993) 3025–3035. [https://doi.org/10.1016/0020-7683\(93\)90210-X](https://doi.org/10.1016/0020-7683(93)90210-X).
- [25] R. Buckminster Fuller, E.J. Applewhite, *Synergetics: Explorations in the Geometry of Thinking*, 1975.
- [26] A. Pugh, *An Introduction to Tensegrity*, 1976.
- [27] B.S. Gan, All About Tensegrity, in: *Computational Modeling of Tensegrity Structures*, 2019: pp. 1–21.
- [28] G. Tibert, *Deployable Tensegrity Structures for Space Applications*, 2002.
- [29] H. Furuya, Concept of Deployable Tensegrity Structures in Space Application, *International Journal of Space Structures*. (1992). <https://doi.org/10.1177/026635119200700207>.
- [30] R.E. Skelton, *An Introduction to the Mechanics of Tensegrity Structures*, (2001).

- [31] S.H. Juan, J.M. Mirats Tur, Tensegrity frameworks: Static analysis review, *Mechanism and Machine Theory*. 43 (2008) 859–881. <https://doi.org/10.1016/j.mechmachtheory.2007.06.010>.
- [32] M.P. Bendsøe, N. Kikuchi, Generating optimal topologies in structural design using a homogenization method, *Computer Methods in Applied Mechanics and Engineering*. 71 (1988) 197–224. [https://doi.org/10.1016/0045-7825\(88\)90086-2](https://doi.org/10.1016/0045-7825(88)90086-2).
- [33] S.S. Simmel, P.C. Nickels, T. Liedl, Wireframe and Tensegrity DNA Nanostructures, (2014). <https://doi.org/10.1021/ar400319n>.
- [34] D. Emmerich, *Constructions de reseaux autotendantes*, 1.377.290, 1963.
- [35] B. Roth, W. Whiteley, *Tensegrity Frameworks*, American Mathematical Society. 265 (198AD) 419–446. <https://doi.org/10.1090/S0002-9947-1981-0610958-6>.
- [36] C.R. Calladine, Modal stiffnesses of a pre-tensioned cable net, *International Journal of Solids and Structures*. 18 (1982) 829–846.
- [37] C.R. Calladine, S. Pellegrino, Two-step matrix analysis of prestressed cable nets, in: *Third International Conference on Space Structures*, 1984.
- [38] S. Pellegrino, Analysis of prestressed mechanisms, *International Journal of Solids and Structures*. 26 (1990) 1329–1350. [https://doi.org/10.1016/0020-7683\(90\)90082-7](https://doi.org/10.1016/0020-7683(90)90082-7).
- [39] C.R. Calladine, S. Pellegrino, First-order infinitesimal mechanisms, *International Journal of Solids and Structures*. 27 (1991) 505–515. [https://doi.org/10.1016/0020-7683\(91\)90137-5](https://doi.org/10.1016/0020-7683(91)90137-5).

- [40] C.R. Calladine, S. Pellegrino, Further remarks on first-order infinitesimal mechanisms, *International Journal of Solids and Structures*. (1992). [https://doi.org/10.1016/0020-7683\(92\)90060-7](https://doi.org/10.1016/0020-7683(92)90060-7).
- [41] B.B. Wang, Cable-strut systems: Part II — Cable-strut, *Journal of Constructional Steel Research*. 45 (1998) 291–299. [https://doi.org/10.1016/S0143-974X\(97\)00076-X](https://doi.org/10.1016/S0143-974X(97)00076-X).
- [42] B.K. Wada, S. Das, Cable-strut systems: Part II - Cable-strut, in: Y.K. Wen (Ed.), *Intelligent Structures -2*, Taylor & Francis, 1992.
- [43] W.J. Lewis, M.S. Jones, K.R. Rushton, Dynamic relaxation analysis of the non-linear static response of pretensioned cable roofs, *Computers and Structures*. 18 (1984) 989–997. [https://doi.org/10.1016/0045-7949\(84\)90142-1](https://doi.org/10.1016/0045-7949(84)90142-1).
- [44] P. Gidak, K. Fresl, *Programming the Force Density Method*, (2012) 0–7.
- [45] A. Molter, O.A.A. da Silveira, V. Bottega, J.S.O. Fonseca, Integrated topology optimization and optimal control for vibration suppression in structural design, *Structural and Multidisciplinary Optimization*. 47 (2013) 389–397. <https://doi.org/10.1007/s00158-012-0829-x>.
- [46] J. Cai, J. Feng, Form-finding of tensegrity structures using an optimization method, *Engineering Structures*. 104 (2015) 126–132. <https://doi.org/10.1016/J.ENGSTRUCT.2015.09.028>.

- [47] N. Bel Hadj Ali, L. Rhode-Barbarigos, A.A. Pascual Albi, I.F.C. Smith, Design optimization and dynamic analysis of a tensegrity-based footbridge, *Engineering Structures*. 32 (2010) 3650–3659. <https://doi.org/10.1016/J.ENGSTRUCT.2010.08.009>.
- [48] P. Zhang, J. Feng, Initial prestress design and optimization of tensegrity systems based on symmetry and stiffness, *International Journal of Solids and Structures*. (2017). <https://doi.org/10.1016/j.ijsolstr.2016.11.030>.
- [49] Y. Chen, J. Yan, P. Sareh, J. Feng, Feasible Prestress Modes for Cable-Strut Structures with Multiple Self-Stress States Using Particle Swarm Optimization, *Computing in Civil Engineering*. 34 (2020).
- [50] H. Ahmed, A. Abdalla, Static and dynamic responses of prestressed concrete beams with openings ., (1993).
- [51] A.F. Naser, Static responses analysis of prestressing tension force effects on vertical deflection and shear force of simply-supported and continuous prestressed concrete bridges, *International Journal of Engineering & Technology*. 7 (2018) 5340–5344. <https://doi.org/10.14419/ijet.v7i4.18021>.
- [52] B. Mercan, H.K. Stolarski, A.E. Schultz, Arc-length and explicit methods for static analysis of prestressed concrete members, *Computers and Concrete*. 18 (2016) 17–37. <https://doi.org/10.12989/cac.2016.18.1.017>.
- [53] K.W. Moored, H. Bart-Smith, The analysis of tensegrity structures for the design of a morphing wing, *Journal of Applied Mechanics, Transactions ASME*. 74 (2007) 668–676. <https://doi.org/10.1115/1.2424718>.

- [54] W. Sobek, P. Teuffel, Adaptive systems in architecture and structural engineering, in: *Smart Structures and Materials*, 2001.
- [55] J.M. Mirats Tur, S.H. Juan, Tensegrity frameworks: Dynamic analysis review and open problems, *Mechanism and Machine Theory*. 44 (2009) 1–18.
<https://doi.org/10.1016/j.mechmachtheory.2008.06.008>.
- [56] R. Motro, S. Najari, P. Jouanna, Static and Dynamic Analysis of Tensegrity Structures, in: *Shell and Spatial Structures Computational Aspects*, 1987: pp. 270–279.
- [57] B. Moussa, N. ben Kahla, J.C. Pons, Evolution of natural frequencies in tensegrity systems: A case study, *International Journal of Space Structures*. 16 (2001) 57–73.
<https://doi.org/10.1260/0266351011495322>.
- [58] N.B. Kalha, B. Moussa, J.C. Pons, Nonlinear dynamic analysis of tensegrity systems, *Journal of the International Association for Shell and Spatial Structures*. 41 (2000) 49–58.
- [59] H. Murakami, Static and dynamic analyses of tensegrity structures. Part II. Quasi-static analysis, *International Journal of Solids and Structures*. 38 (2001) 3615–3629.
[https://doi.org/10.1016/S0020-7683\(00\)00233-X](https://doi.org/10.1016/S0020-7683(00)00233-X).
- [60] N. Ashwear, A. Eriksson, Natural frequencies describe the pre-stress in tensegrity structures, *Computers and Structures*. (2014).
<https://doi.org/10.1016/J.COMPSTRUC.2014.01.020>.

- [61] X. Yuan, X. Liang, A. Li, Shape and force control of prestressed cable-strut structures based on nonlinear force method, *Advances in Structural Engineering*. 19 (2016) 1917–1926. <https://doi.org/10.1177/1369433216652411>.
- [62] Y. Wang, G. Senatore, Extended integrated force method for the analysis of prestress-stable statically and kinematically indeterminate structures, *International Journal of Solids and Structures*. 202 (2020) 798–815. <https://doi.org/10.1016/j.ijsolstr.2020.05.029>.
- [63] G. Senatore, A.P. Reksowardojo, Force and Shape Control Strategies for Minimum Energy Adaptive Structures, *Frontiers in Built Environment*. 6 (2020). <https://doi.org/10.3389/fbuil.2020.00105>.
- [64] A.P. Reksowardojo, G. Senatore, A proof of equivalence of two force methods for active structural control, *Mechanics Research Communications*. 103 (2020). <https://doi.org/10.1016/j.mechrescom.2019.103465>.
- [65] G. Senatore, P. Duffour, P. Winslow, Synthesis of minimum energy adaptive structures, *Structural and Multidisciplinary Optimization*. 60 (2019) 849–877. <https://doi.org/10.1007/s00158-019-02224-8>.
- [66] A.P. Reksowardojo, G. Senatore, I.F.C. Smith, Design of Structures That Adapt to Loads through Large Shape Changes, *Journal of Structural Engineering*. 146 (2020) 04020068. [https://doi.org/10.1061/\(asce\)st.1943-541x.0002604](https://doi.org/10.1061/(asce)st.1943-541x.0002604).
- [67] F. Xiaodong, Dynamic Response and Vibration Control of a Planar Tensegrity Beam under El Centro Seismic Excitation, *Journal of Aerospace Engineering and Mechanics*. 1 (2017) 73–82. <https://doi.org/10.36959/422/428>.

- [68] M. Rasool, M.K. Singha, Aeroelastic analysis of pre-stressed variable stiffness composite panels, *JVC/Journal of Vibration and Control*. 26 (2020) 724–734. <https://doi.org/10.1177/1077546319889865>.
- [69] J.R. Taylor, Genetic Optimization of a Tensegrity Structure, (2002).
- [70] N. Ashwear, A. Eriksson, Vibration health monitoring for tensegrity structures, *Mechanical Systems and Signal Processing*. 85 (2017) 625–637. <https://doi.org/10.1016/j.ymssp.2016.08.039>.
- [71] V. Giurgiutiu, Structural Health Monitoring with Piezoelectric Wafer Active Sensors, Academic Press, 2014. <https://doi.org/10.1016/B978-0-12-418691-0.00003-4>.
- [72] W.-H. Hu, D.-H. Tang, J. Teng, S. Said, Rolf.G. Rohrmann, Structural Health Monitoring of a Prestressed Concrete Bridge Based on Statistical Pattern Recognition of Continuous Dynamic Measurements over 14 years, *Sensors*. 18 (2018) 4117. <https://doi.org/10.3390/s18124117>.
- [73] G. Suwała, L. Knap, J. Holnicki-Szulc, Prestressing for reduction of local vibrations in a rotorcraft, *Engineering Transactions*. 64 (2016) 367–380.
- [74] A. Amendola, A. Krushynska, C. Daraio, N.M. Pugno, F. Fraternali, Tuning frequency band gaps of tensegrity mass-spring chains with local and global prestress, *International Journal of Solids and Structures*. 155 (2018) 47–56. <https://doi.org/10.1016/J.IJSOLSTR.2018.07.002>.

- [75] R.K. Pal, M. Ruzzene, J.J. Rimoli, Tunable wave propagation by varying prestrain in tensegrity-based periodic media, *Extreme Mechanics Letters*. 22 (2018) 149–156. <https://doi.org/10.1016/J.EML.2018.06.005>.
- [76] I. Němec, M. Trcala, I. Ševčík, H. Štekbauer, New Formula for Geometric Stiffness Matrix Calculation, *Journal of Applied Mathematics and Physics*. 04 (2016) 733–748. <https://doi.org/10.4236/jamp.2016.44084>.
- [77] K.J. Bathe, *Finite Element Procedures in Engineering Analysis*, 1996. <https://doi.org/10.1016/B978-0-12-384984-7.00010-5>.
- [78] E.A. de Souza Neto, D. Peric, D.R.J. Owen, *Computational Methods for Plasticity: Theory and Applications*, John Wiley & Sons, 2008. <https://doi.org/10.1002/9780470694626>.
- [79] T. Belytschko, W.K. Liu, B. Moran, K. Elkhodary, *Nonlinear Finite Elements for Continua and Structures*, 2nd Edition, John Wiley & Sons, 2014.
- [80] H.C. Tran, J. Lee, Self-stress design of tensegrity grid structures with exostresses, *International Journal of Solids and Structures*. 47 (2010) 2660–2671. <https://doi.org/10.1016/j.ijsolstr.2010.05.020>.
- [81] N.S. Khot, Multicriteria Optimization for Design of Structures with Active Control, *Journal of Aerospace Engineering*. 11 (1998) 45–51. [https://doi.org/10.1061/\(asce\)0893-1321\(1998\)11:2\(45\)](https://doi.org/10.1061/(asce)0893-1321(1998)11:2(45)).
- [82] T.T. Soong, G.P. Cimellaro, Future directions in structural control, *Structural Control and Health Monitoring*. 16 (2009) 7–16. <https://doi.org/10.1002/stc.291>.

- [83] H.P. Fuentes, M. Zehn, Application of the Craig-Bampton Model Order Reduction Method To a Composite Structure :, 12 (2014) 37–50.
- [84] M. Pastor, M. Binda, T. Harčarik, Modal Assurance Criterion, Procedia Engineering. 48 (2012) 543–548. <https://doi.org/10.1016/J.PROENG.2012.09.551>.
- [85] A.G. Davenport, The spectrum of horizontal gustiness near the ground in high winds, Quarterly Journal of the Royal Meteorological Society. 87 (1961) 194–211. <https://doi.org/10.1002/qj.49708837618>.
- [86] J.R. Fuller, Evolution of airplane gust loads design requirements, John Wiley & Sons, 1995. <https://doi.org/10.2514/3.46709>.
- [87] NX, Nastran, Aeroelastic Analysis User’s Guide, (2012).
- [88] R.H. MacNeal, National Aeronautics and Space Administration. Scientific, T.I. Office, The NASTRAN Theoretical Manual, Scientific and Technical Information Office, National Aeronautics and Space Administration, 1970.
- [89] A. Voß, An Implementation of the Vortex Lattice and the Doublet Lattice Method, (2020).
- [90] M.G. Nieto, P. v. Thomas, M.S.A. ElSayed, M. Saad, G.L. Brown, L.M. Hilliard, Development of Efficient Dynamic Aeroelasticity Model for High Fidelity Pointing Accuracy Assessment of VLBI Earth-Based Radio Antennas, International Journal of Aeronautical and Space Sciences. 21 (2020) 693–706. <https://doi.org/10.1007/s42405-019-00238-6>.

- [91] D.E. Goldberg, Genetic Algorithms in Search, Optimization, and Machine Learning, (n.d.)
[1] “Goldberg_Genetic_Algorithms_in_Search.pdf.” .
- [92] S.N. Sivanandam, S.N. Deepa, Principles of Soft Computing, Wiley New Delhi, 2013.
<https://www.worldcat.org/title/principles-of-soft-computing/oclc/891566849>.
- [93] E.M. Kasprzak, K.E. Lewis, Pareto analysis in multiobjective optimization using the collinearity theorem and scaling method, Structural and Multidisciplinary Optimization. 22 (2001) 208–218. <https://doi.org/10.1007/s001580100138>.
- [94] H. Eschenauer, J. Koski, A. Osyczka, Multicriteria Design Optimization, Springer-Verlag Berlin Heidelberg, 1990. <https://doi.org/10.1007/978-3-642-48697-5>.
- [95] N. Ashwear, A. Eriksson, Natural frequencies describe the pre-stress in tensegrity structures, Computers and Structures. 138 (2014) 162–171.
<https://doi.org/10.1016/j.compstruc.2014.01.020>.
- [96] M. Yordanova, Y. Evstatieva, G. Chernev, S. Ilieva, R. Denkova, D. Nikolova, Enhancement of xylanase production by sol-gel immobilization of *Aspergillus awamori* K-1, Bulgarian Journal of Agricultural Science. 19 (2013) 117–119.
- [97] Z. Chen, W. Zheng, Chinese VLBI Network and e-VLBI Technology Applications in Chinese Lunar Exploration Program, in: Chinese Academy of Sciences et al. (Eds) China’s e-Science Blue Book 2020, Springer, Singapore, 2020: pp. 169–190.
https://doi.org/10.1007/978-981-15-8342-1_9.

- [98] G. Giovannini, W.D. Cotton, L. Feretti, L. Lara, T. Venturi, VLBI Observations of a Complete Sample of Radio Galaxies: 10 Years Later, *The Astrophysical Journal*. 552 (2001) 508–526. <https://doi.org/10.1086/320581>.
- [99] A. Brunthaler, M.J. Reid, K.M. Menten, X.W. Zheng, A. Bartkiewicz, Y.K. Choi, T. Dame, K. Hachisuka, K. Immer, G. Moellenbrock, L. Moscadelli, K.L.J. Rygl, A. Sanna, M. Sato, Y. Wu, Y. Xu, B. Zhang, The Bar and Spiral Structure Legacy (BeSSeL) survey: Mapping the Milky Way with VLBI astrometry, *Astronomische Nachrichten*. 332 (2011) 461–466. <https://doi.org/10.1002/asna.201111560>.
- [100] T. Hobiger, T. Kondo, H. Schuh, Very long baseline interferometry as a tool to probe the ionosphere, *Radio Science*. 41 (2006) 1–10. <https://doi.org/10.1029/2005RS003297>.
- [101] A. Boivin, F. Boilard, P. Messier, P. Tremblay, 12 m VLBI antenna structural simulation, 2014.
- [102] Intertronic Solutions, (2021). <https://www.intertronicsolutions.com/landing.php>.
- [103] E. Toolbox, Aluminum Alloys - Mechanical Properties, (2008). https://www.engineeringtoolbox.com/properties-aluminum-pipe-d_1340.html.
- [104] A. Hitchcox, High-strength steel made for hydraulic cylinders, *Hydraulics & Pneumatics*. (2013). <https://www.hydraulicspneumatics.com/technologies/cylinders-actuators/article/21883501/highstrength-steel-is-made-for-hydraulic-cylinders>.
- [105] K. Deb, *Multi-Objective Optimization Using Evolutionary Algorithms: An Introduction*, John Wiley & Sons, 2001.